N85-22391

GAS TURBINE LABORATORY
DEPARTMENT OF AERONAUTICS AND ASTRONAUTICS
MASSACHUSETTS INSTITUTE OF TECHNOLOGY
CAMBRIDGE, MASSACHUSETTS 02139

Final Report

on

NASA Grant NAG 3-200

STRUCTURAL RESPONSE OF A ROTATING BLADED DISK TO ROTOR WHIRL

submitted to

NASA LEWIS RESEARCH CENTER
Structural Dynamics Section
21000 Brookpark Road
Cleveland, Ohio 44135

Attention: Gerald Brown
MS 500-302

Principal
Investigator: Edward F. Crawley
Associate Professor
Department of Aeronautics & Astronautics

April 1985

ABSTRACT

A set of high speed rotating whirl experiments were performed in the vacuum of the MIT Blowdown Compressor Facility on the MIT Aeroelastic Rotor, which is structurally typical of a modern high bypass ratio turbofan stage. These tests identified the natural frequencies of whirl of the rotor system by forcing its response using an electromagnetic shaker whirl excitation system. The excitation was slowly swept in frequency at constant amplitude for several constant rotor speeds in both a forward and backward whirl direction.

The natural frequencies of whirl determined by these experiments were compared to those predicted by an analytical 6 DOF model of a flexible blade-rigid disk-flexible shaft rotor. The model is also presented in terms of nondimensional parameters in order to assess the importance of the interaction between the bladed disk dynamics and the shaft-disk dynamics. The correlation between the experimental and predicted natural frequencies is reasonable, given the uncertainty involved in determining the stiffness parameters of the system.

"Page missing from available version"

142

Acknowledgements

The author would like to express his gratitude to all those at MIT who contributed to this effort, especially to his thesis advisor, Prof. Edward Crawley for his guidance and insightful comments. I would also like to thank Professors J. Dugundji and N. Ham for their instructive comments on rotor dynamics and turbomachine aeroelasticity. The encouragement from, and rewarding discussions with colleagues Dinkar Mokadam and Kenneth Hall are also greatly appreciated. Thanks are also due to John Kehrbaum and Michael Bernard for their contributions to the experimental program, and to Steve Chamberlin for his help with the CAD figures.

Finally, a special thanks to my wife Kerry for her help with the preparation of this document and her unbounded support for my graduate studies.

This research was sponsored under NASA Lewis Research Center grant NAG3-200, with Dr. R. Kielb serving as monitor.

Contents

List of Tables

List of Figures

1. Introduction

Current trends in the design of aircraft gas turbines have resulted in lighter, more structurally efficient engines with higher spool speeds and higher bypass ratio fans. In particular, fans are often unshrouded and are of high aspect ratio, thereby increasing the flexibility of the fan blading. This increase in blade flexibility tends to depress the blade natural frequencies towards those of the shaft-disk system. As the natural frequency of the blade, in its first bending mode for example, approaches the natural frequency of the shaft disk system, the interaction between the blade modes and the shaft-disk modes increases. Neglecting these interaction effects could in some cases lead to inaccurate estimates of rotor critical speeds and system natural frequencies at speed. Unexpected resonances within the engine's operating envelope may result, with all the reliability and performance penalties inherent in operating at such points. This report describes a set of experiments carried out in order to evaluate the influence of shaft flexibility on the dynamics of of bladed-disk systems.

The whirling motion of a rotating bladed disk-shaft system has been investigated by several authors. Early efforts by Coleman and Feingold [1] to investigate the phenomenon known as helicopter ground resonance identified the cause of the instability to be whirling of the rotor. Later analytical efforts by Crandall and Dugundji [2] studied the whirling of propellors powered by piston engines. The finite element approach taken by Palladino and Rossettos [3] as well as Loewy and Khader [4] provides numerical estimates of the natural frequencies of a bladed disk-shaft system. In this investigation, the analytical model derived by Mokadam [5] will be modified to predict the natural frequencies of whirl for a rotor typical of a cantilevered turbofan stage. The results of a set of experimental

whirl testing will be compared with predictions of the model.

A simplified rotor model involving a flexible shaft, rigid disk, and flexible blading [5] was employed to predict the dynamic behaviour of the MIT Aeroelastic (AE) rotor as installed in the MIT Blowdown Compressor Facility [6]. The system vibration modes predicted by the model included motion of the disk centroid in the direction of rotation (forward whirl) and opposite to the direction of rotation (backward whirl) as viewed from the rotor frame of reference. The degree of interaction between the bladed disk and shaft-disk dynamics can be quantified by a set of nondimensional interaction criteria. The magnitude of these interaction criteria determines if sufficiently accurate results can be obtained with uncoupled analyses of the blade-disk and shaft-disk dynamics. Otherwise a coupled analysis or a finite element approach may be indicated.

An experimental program to determine the natural frequencies of the MIT AE rotor was undertaken in order to validate the predictions obtained from the model. A series of forced response tests were conducted by setting up a particular whirl excitation pattern, either forward or backward, and sweeping through a range of forcing frequencies at constant rotor speed. The response of the system was monitored with an array of on-rotor and nonrotating instrumentation. By sweeping the forcing frequency and monitoring the system response for amplitude peaks, the system natural frequencies were found. Therefore the system natural frequencies predicted by the model could be compared to those experimentally determined.

The series of experiments described in this report were the high speed tests in an ongoing rotor whirl testing program. Previous work [5] involved the development of the flexible shaft-rigid disk-flexible blade model and the construction of a low speed vacuum whirl spin rig. Tests were conducted in the low speed spin rig in 5 Hz (300 rpm) increments of rotor speed up to

30 Hz (1800 rpm). The high speed experiments were conducted in the vacuum of the MIT Blowdown Compressor facility test section in 30 Hz (1800 rpm) increments of rotor speed up to 150 Hz (9000 rpm). At higher rotor speeds the effects of rotation had a more pronounced effect on the system natural frequencies and on the interaction of the modes.

Chapter 2 provides an overview of the 6 degree of freedom (DOF) coupled rotor model developed in [5] and presents the necessary first order corrections to the shaft disk dynamics to account for a system center of mass offset from the disk geometric center. The nondimensional interaction criteria are also explored and comparison are made with the classical cantilevered bladeless rotor analysis of Den Hartog [7] and with recent work on bladed disk dynamics by Crawley and Mokadam [8]. The experimental facilities, instrumentation, whirl excitation system are described in Chapter 3. Chapter 4 describes the series of nonrotating modal surveys performed on the MIT AE rotor as installed in the MIT Compressor Blowdown Facility in order to characterize the stiffness parameters of the system. From the experimental determination of the system stiffness parameters, the natural frequencies of the rotating blade-disk-shaft system are predicted. The rotating forced whirl response tests are discussed in Chapter 5 and reasonable agreement between the predicted and experimentally determined natural frequencies is found.

2. Analysis of a Rotating Shaft - Bladed Disk System

In order to predict the dynamic behaviour of a shroudless fan with flexible blades affixed to a rigid disk and supported by a flexible shaft, an appropriate analytic model has been developed. Since they are attached to a rigid disk and not connected through midspan or tip shrouds, the N fan blades are assumed to be elastically uncoupled. The blades are also assumed to be structurally identical, or well tuned. The shaft upon which the disk is suppported has sufficient flexibility to allow for translation of the disk centroid in the plane of rotation and pitching of the disk out of the plane of rotation. The main objective of the development of the coupled blade-disk-shaft dynamic model is to determine the criteria for interaction between the blade motion and the rigid body motion of the disk supported on the flexible shaft. If the coupling interactions are strong, then the solution of the fully coupled system is warranted in order to obtain accurate estimates of the system natural frequencies. Otherwise, if the interactions are weak, then the bladed disk dynamic problem may be solved independent of the shaft-disk dynamic problem.

The generalized degrees of freedom of the model express blade and shaft deflection with reference to a rotor-fixed coordinate system. The equations will first be derived in a coordinate system centered at the geometric centroid the disk. In the absence of a massive shaft, this point would also be the system center of mass. The approximate effect of the presence of a massive shaft, which shifts the system center of mass of the system away from the centroid of the disk, will be explored.

Subsequently the equations will be expressed in a nondimensional form. In this way the the relevant nondimensional parameters governing the coupled blade-disk-shaft vibration of a shroudless fan can be identified. These parameters will be

compared to those obtained by Den Hartog [7] in his classical analysis of the asynchronous whirl of a cantilevered bladeless disk. The similarities between the two analyses will be identified and the necessary extensions to include blade flexibility will be pointed out. The nondimensionalization procedure will facilitate the assessment of the importance of the interactions between the bladed disk vibration and the whirling shaft motion in rotating turbomachinery.

2.1) Equations of Motion

The homogeneous equations of motion of a system of N flexible blades cantilevered from the hub of a rigid disk supported by a rotating flexible shaft will be presented. The blades are modelled with a single Ritz bending mode and are attached to the disk with an effective structural stagger angle α between the normal to the disk plane and the blade chord line, as shown in fig. 2.1. In general the disk may be located at any axial position along a shaft of arbitrary boundary conditions. The shaft stiffness, which is represented by equivalent springs, may include both translational and pitch displacement stiffnesses, as well as a stiffness coupling between disk pitching and translation.

The equations of motion for the blade-disk-shaft system were derived by Mokadam [5] using a Lagrangian formulation. This model of the whirling shaft-bladed disk system included the following degrees of freedom, expressed in the rotating coordinate system, as shown fig. 2.1:

- two orthogonal disk translation modes in the plane of rotation (q_{xR} and q_{yR}),
- two out of plane disk pitch modes about mutually orthogonal diametral lines ($q_{\zeta R}$ and $q_{\eta R}$),
- one Ritz beam first bending mode for each of

the N blades (q_i, i=0,...,N-1).

The use of coordinates expressed in the rotating frame of reference is helpful from the point of view of the experimental investigator, since displacement and acceleration signals measured on the rotating bladed disk are referred to this coordinate frame. Comparisons between the experimental results and the behaviour predicted by the analytical model are therefore more readily made if the behaviour is described in the rotating reference frame.

The relevant coupling of the blade modes to the shaft translation and pitching becomes apparent when the displacement for each individual blade is expressed as the sum of sine and cosine nodal diameter patterns:

$$q_i = \sum_{n=0}^{N-1} [\, -a_n \sin n\theta_i + b_n \cos n\theta_i \,] , \qquad (2.1.1)$$

where θ_i is the angular position of the i^{th} blade on the disk:

$$\theta_i = \frac{2\pi i}{N} .$$

Only the one nodal diameter sine and cosine blade modes couple with the translation and pitching of the disk on its shaft. The umbrella or zero nodal diameter cosine blade mode completely decouples from the other blade modes and would couple with the disk axial translation and in-plane rotational degrees of freedom of the disk. However the present model does not include disk axial motion or rotational vibration motions. Therefore the zero nodal diameter blade mode for this simpliflied model is governed by eq. (2.1.2).

$$m_0 \ddot{b}_0 + [\, K_B + (m_\Omega - m_0 \cos^2\alpha)\Omega^2 \,] b_0 = 0 . \qquad (2.1.2)$$

For a discussion of the dynamics of this mode, see [8].

The higher blade modes, which have more than one nodal diameter, also completely decouple from the disk motion. These are the so called reactionless modes which exert no net inertial reaction on the disk due to their motion. The equations of motion for these so called reactionless modes are given by:

$$m_0 \ddot{a}_n + [\, K_B + (m_\Omega - m_0 \cos^2\alpha)\Omega^2 \,] a_n = 0 \qquad (n>1) \qquad (2.1.3)$$

$$m_0 \ddot{b}_n + [\, K_B + (m_\Omega - m_0 \cos^2\alpha)\Omega^2 \,] b_n = 0 \qquad (2.1.4)$$

The homogeneous coupled whirl equations of motion, which include the blade one nodal diameter motion, are shown in matrix form in eq. (2.1.5). The blade one nodal diameter modes couple to the disk translation motion inertially, gyroscopically and centrifugally. The $n=1$ blade modes couple to the disk pitch motion inertially and centrifugally. These coupled whirl equations were derived assuming that the center of the axis system located at the centroid of the disk coincided with the system center of mass, as shown in fig. 2.2a.

In equations (2.1.2) to (2.1.5), the following definitions hold:

$$M = \int_V dm$$

$$I_P = \int_V [\, x^2 + z^2 \,] dm \qquad = \int_V [\, y^2 + z^2 \,] dm$$

$$m_0 = r_T^2 \int_{r_H}^{r_T} [\gamma(r)]^2 dm \quad , \quad m_1 = r_T \int_{r_H}^{r_T} \gamma(r) r dm$$

$$m_2 = r_T \int_{r_H}^{r_T} \gamma(r) dm \quad , \quad m_\Omega = r_T^2 \int_{r_H}^{r_T} r \int_{r_H}^{r} \frac{\partial \gamma}{\partial r}^2 dr\, dm$$

The quantity m_0 is the blade modal mass, m_1 is the blade consistent mass coupling to disk pitch, m_2 is the blade

$$
\begin{bmatrix}
M & 0 & 0 & S & \frac{N}{2} m_2 \cos\alpha & 0 \\
 & M & -S & 0 & 0 & \frac{N}{2} m_2 \cos\alpha \\
 & & I_P & 0 & -\frac{N}{2} m_1 \sin\alpha & 0 \\
 & & & I_P & 0 & -\frac{N}{2} m_1 \sin\alpha \\
 & & & & \frac{N}{2} m_0 & 0 \\
 & \text{SYMMETRIC} & & & & \frac{N}{2} m_0
\end{bmatrix}
\begin{Bmatrix}
\ddot{q}_{xR} \\ \ddot{q}_{yR} \\ \ddot{q}_{\xi R} \\ \ddot{q}_{\eta R} \\ \ddot{a}_1 \\ \ddot{b}_1
\end{Bmatrix} +
$$

$$
2\Omega
\begin{bmatrix}
0 & -M & S & 0 & 0 & -\frac{N}{2} m_2 \cos\alpha \\
 & 0 & 0 & S & \frac{N}{2} m_2 \cos\alpha & 0 \\
 & & 0 & 0 & 0 & 0 \\
 & & & 0 & 0 & 0 \\
 & & & & 0 & 0 \\
 & \text{SKEW-SYMMETRIC} & & & & 0
\end{bmatrix}
\begin{Bmatrix}
\dot{q}_{xR} \\ \dot{q}_{yR} \\ \dot{q}_{\xi R} \\ \dot{q}_{\eta R} \\ \dot{a}_1 \\ \dot{b}_1
\end{Bmatrix} +
$$

$$
\begin{bmatrix}
K_{xR}-\Omega^2 M & 0 & 0 & K_{x\eta R}-\Omega^2 S & -\Omega^2\frac{N}{2} m_2 \cos\alpha & 0 \\
 & K_{yR}-\Omega^2 M & K_{y\xi R}+\Omega^2 S & 0 & 0 & -\Omega^2\frac{N}{2} m_2 \cos\alpha \\
 & & K_{\xi R}+\Omega^2 I_P & 0 & -\Omega^2\frac{N}{2} m_1 \sin\alpha & 0 \\
 & & & K_{\eta R}+\Omega^2 I_P & 0 & -\Omega^2\frac{N}{2} m_1 \sin\alpha \\
 & & & & \frac{N}{2}(K_B+\Omega^2[m_\Omega - m_0 \cos^2\alpha]) & 0 \\
 & \text{SYMMETRIC} & & & & \frac{N}{2}(K_B+\Omega^2[m_\Omega - m_0 \cos^2\alpha])
\end{bmatrix}
\begin{Bmatrix}
q_{xR} \\ q_{yR} \\ q_{\xi R} \\ q_{\eta R} \\ a_1 \\ b_1
\end{Bmatrix} = 0
$$

(2.1.5)

consistent mass coupling to disk translation, and m_{Ω} is the blade mass foreshortening term.

Often the system center of mass is not located at the centroid of the disk, which was chosen in the above analysis as the coordinate system origin. This is in fact the case for the MIT AE rotor. Instrumentation considerations made it desirable to refer the motion to a coordinate system center at the geometric centroid of the disk. Because the mass of the shaft was not negligible, the center of mass of the rotor system was offset from the centroid of the disk. Under these circumstances the translational and pitch motion the disk are inertially coupled, even in the absence of blade dynamics or shaft elastic coupling. This effect must be included in the equations of motion. An appropriate axial mass imbalance S is defined as:

$$S = \int_V z dm \qquad (2.1.6)$$

The mass imbalance was introduced in the coupled whirl equations of motion by correcting the upper left corner 4x4 disk motion submatrices of eq. (2.1.5) [4]. The corrected submatrix equation exactly represents the whirling motion of a disk with rigid blades. For small offsets of the center of mass from the disk centriod, the effect of the resulting imbalance on the blade dynamics and its coupling to the disk motion is of higher order, and will not be included in the current model. For an exact representation of these imbalance effects on the blade motion see [8]. The matrix equations of motion for the mass imbalance corrected system are shown in eq. (2.1.7). The dynamics of the blade modes which are uncoupled from the disk motion, eq. (2.1.2) to (2.1.4), remain unchanged.

The set of equations (2.1.7) show the characteristic behavior of the coupled shaft-bladed disk system expressed in the rotor frame of reference. Disk rigid body translation displacements q_{xR} and q_{yR} couple inertially to both the disk

$$
\begin{bmatrix}
M & 0 & 0 & S & \frac{N}{2} m_2 \cos\alpha & 0 \\
 & M & -S & 0 & 0 & \frac{N}{2} m_2 \cos\alpha \\
 & & I_P & 0 & -\frac{N}{2} m_1 \sin\alpha & 0 \\
 & & & I_P & 0 & -\frac{N}{2} m_1 \sin\alpha \\
 & & & & \frac{N}{2} m_0 & 0 \\
 & \text{SYMMETRIC} & & & & \frac{N}{2} m_0
\end{bmatrix}
\begin{Bmatrix}
\ddot{q}_{xR} \\ \ddot{q}_{yR} \\ \ddot{q}_{\xi R} \\ \ddot{q}_{\eta R} \\ \ddot{a}_1 \\ \ddot{b}_1
\end{Bmatrix} +
$$

$$
2\Omega
\begin{bmatrix}
0 & -M & S & 0 & 0 & -\frac{N}{2} m_2 \cos\alpha \\
 & 0 & 0 & S & \frac{N}{2} m_2 \cos\alpha & 0 \\
 & & 0 & 0 & 0 & 0 \\
 & & & 0 & 0 & 0 \\
 & & & & 0 & 0 \\
 & \text{SKEW-SYMMETRIC} & & & & 0
\end{bmatrix}
\begin{Bmatrix}
\dot{q}_{xR} \\ \dot{q}_{yR} \\ \dot{q}_{\xi R} \\ \dot{q}_{\eta R} \\ \dot{a}_1 \\ \dot{b}_1
\end{Bmatrix} +
$$

$$
\begin{bmatrix}
K_{xR}-\Omega^2 M & 0 & 0 & K_{x\eta R}-\Omega^2 S & -\Omega^2 \frac{N}{2} m_2 \cos\alpha & 0 \\
 & K_{yR}-\Omega^2 M & K_{y\xi R}+\Omega^2 S & 0 & 0 & -\Omega^2 \frac{N}{2} m_2 \cos\alpha \\
 & & K_{\xi R}+\Omega^2 I_P & 0 & -\Omega^2 \frac{N}{2} m_1 \sin\alpha & 0 \\
 & & & K_{\eta R}+\Omega^2 I_P & 0 & -\Omega^2 \frac{N}{2} m_1 \sin\alpha \\
 & & & & \frac{N}{2}(K_B+\Omega^2[m_\Omega - m_0 \cos^2\alpha]) & 0 \\
 & \text{SYMMETRIC} & & & & \frac{N}{2}(K_B+\Omega^2[m_\Omega - m_0 \cos^2\alpha])
\end{bmatrix}
\begin{Bmatrix}
q_{xR} \\ q_{yR} \\ q_{\xi R} \\ q_{\eta R} \\ a_1 \\ b_1
\end{Bmatrix} = 0
$$

(2.1.7)

rigid body pitch motion, through the center of mass offset term S, and the blade one nodal diameter blade deflections, through the N/2 m $\cos\alpha$ terms. The inertial coupling effects are always symmetric in the equations of motion. The two translational degrees of freedom also couple gyroscopically: to each other (through the rotor mass $2\Omega M$), to the disk pitching motion (through $2\Omega S$), and to the blade one nodal diameter displacement (through $\Omega N m_2 \cos\alpha$). The gyroscopic coupling terms are antisymmetric, or skew-symmetric, in the equations of motion. The disk rigid body translation terms in the stiffness matrix show the centrifugal destiffening of the translational stiffness terms K_{xR} and K_{yR}. Depending on the sign of the center of mass offset S, the translation-pitch coupling stiffnesses $K_{x\eta R}$ and $K_{y\xi R}$ are either alternately destiffened or stiffened by the centrifugal effects. The disk translation motion is also destiffened by centrifugal coupling to the blade one nodal diameter motion.

The disk out-of-plane pitching displacements $q_{\xi R}$ and $q_{\eta R}$ can be seen from eq. (2.1.7) to inertially couple with the disk translation motion (through S) and to the blade one nodal diameter displacement through $N/2 \cdot m_1 \sin\alpha$. The disk pitching degrees of freedom are not mutually coupled in the gyroscopic sense, as were the two disk translational degrees of freedom. This is due to the fact that the equations of motion are expressed in the rotor frame and not in a nonrotating coordinate system. If the equations were expressed in the nonrotating frame, the converse would be true, that is the two disk pitch degrees of freedom would gyroscopically couple with each other and the disk translation motion would be mutually uncoupled. The disk pitching stiffness terms $K_{\xi R}$ and $K_{\eta R}$ are centrifugally stiffened by $\Omega^2 I_p$. Depending on the sign of S, the disk translation-pitch coupling stiffnesses $K_{x\eta R}$ and $K_{y\xi R}$ are alternately centrifugally destiffened or stiffened. The blade one nodal

diameter displacement modes couple to centrifugally destiffen the disk pitch motion through the terms $\Omega^2 N/2 \cdot m_1 \sin\alpha$.

Centrifugal blade stiffening terms are also seen on the diagonal of the stiffness matrix in rows 5 and 6. The Southwell coefficient ℓ, which represents the degree of stiffening, relates the blade natural frequencies in the absense or presence of mean rotation Ω :

$$\omega_R = \sqrt{\omega_B^2 + \ell\Omega^2} \qquad (2.1.8)$$

Comparing equations (2.1.7) and (2.1.8), the Southwell coefficient is:

$$\ell = \frac{m_\Omega}{m_0} - \cos^2\alpha \qquad (2.1.9)$$

The first term in eq. (2.1.9) represents the stiffening due to blade foreshortening and the second term the destiffening due to in-plane motion.

2.2) Nondimensional Equations of Motion and Interaction Criteria

The coupled set of equations (2.1.7) describe the homogeneous behavior of the bladed disk - shaft rotating system. It is instructive to express the equations nondimensionally, and to identify the relevant nondimensional parameters. The relative importance of each structural dynamic quantity, such as shaft stiffness or blade inertial coupling to disk translation, can be determined by evaluating the magnitude of the corresponding nondimensional terms. Therefore a nondimensional equation set would be more useful for evaluating the criteria for interaction between the dynamics of blade vibration and shaft whirl. Observations comparing this normalization scheme and Den Hartog's [7] classical approach for a whirling cantilevered rotor with no blades will also be made.

In formulating the nondimensionalization scheme four length scales appear. Two length scales naturally arise from the mass parameters: the axial offset of the system center of mass from the centroid of the disk (c) and the radius of gyration for pitching of the disk (d). The translational degrees of freedom q_{xR} and q_{yR} will be normalized by d. The length scales that arise from consideration of the blade geometry are the blade tip radius r_T and hub radius r_H. Of the four length scales, one is chosen as the fundamental length and the others are expressed as ratios which are normalized by this length. Because the translational degrees of freedom were normalized by the disk pitching radius of gyration, d is chosen as the fundamental length and the other length scales are expressed as:

$$\frac{c}{d} \quad , \qquad \frac{r_T}{d} \quad , \qquad \frac{r_H}{d} \quad .$$

The natural frequency of the nonrotating tuned blades ω_B was chosen as the reference time quantity. This is the blade frequency that would be measured if the blade was cantilevered from a perfectly rigid foundation. This choice of a reference time scale was arbitrary but convenient for the current problem of assessing the impact of the flexibility and whirling of the shaft on the blade dynamics. The time variable t normalized by ω_B is τ:

$$\tau = \omega_B t \tag{2.2.1}$$

where:

$$\omega_B^2 = \frac{K_B}{m_0} \tag{2.2.2}$$

Therefore differentiation with respect to time ($\dot{}$) becomes differentiation with respect to ω_B ( )':

$$\frac{d}{dt} = (\dot{}) = \omega_B \frac{d}{d\tau} = \omega_B (\,)' \qquad (2.2.3)$$

Several nondimensional mass parameters arise in the normalization scheme. The comparison of diagonal and off-diagonal inertia terms in the equations of motion yields mass coupling ratios μ expressing the relative magnitude of the inertial coupling terms. A ratio of mass matrix diagonal entries ρ, which expresses the relative mass of the blades and the disk, also appears. As defined below, the mass coupling parameter for interaction between disk translational motion and blade one nodal diameter vibration is μ_{TB} (i.e. μ Translation Blade) [9]. Note the dependence of μ_{TB} on the square of the cosine of the effective stagger angle angle α. The inertial coupling between disk pitching and blade one nodal diameter vibration is μ_{PB} (i.e. μ Pitch Blade). This term depends on the square of the sine of the stagger angle. The ratio of mass matrix diagonal elements that arises naturally from this normalization scheme is the ratio of the blade modal mass to the disk pitch moment of inertia, ρ. These nondimensional inertia terms are defined below:

$$\mu_{TB} = \frac{\frac{N}{2} m_2^2 \cos^2\alpha}{m_0 M} \quad , \quad \mu_{PB} = \frac{\frac{N}{2} m_1^2 \sin^2\alpha}{m_1 I_P} \quad .$$

$$\rho = \frac{m_0}{I_P}$$

The disk translation-pitch inertial coupling term μ_{TP}, defined below, is nonzero due to the choice of a coordinate system centered at the centroid of the disk, and not at the center of mass of the system. Note that the expression for μ_{TP} reduces to the square of the offset of the center of mass from the disk centroid normalized by the fundamental length scale d.

$$\mu_{TP} = \frac{S^2}{MI_P} = \left(\frac{c}{d}\right)^2$$

The effects of rotation yield two nondimensional parameters, the Southwell coefficient ℓ as defined in eqn.(2.1.9) and the nondimensional rotor speed Ω/ω_B:

$$\ell = \frac{m_\Omega}{m_0} - \cos^2\alpha \quad , \quad \frac{\Omega}{\omega_B} \; .$$

Applying the normalization scheme to the stiffness matrix in the equations of motion (2.1.7) yields nondimensional frequency ratios and a stiffness coupling parameter. The frequency ratios ω_x/ω_B and ω_y/ω_B, defined below, quantify the relative proximity of the uncoupled shaft translational vibrational frequency to the natural frequency of a cantilevered blade. The frequency ratios ω_η/ω_B and ω_ξ/ω_B express the proximity of the uncoupled shaft pitching frequency to the blade frequency. For a symmetric shaft these ratios are:

$$\left(\frac{\omega_x}{\omega_B}\right)^2 = \frac{\frac{K_{xR}}{M}}{\omega_B^2} = \left(\frac{\omega_y}{\omega_B}\right)^2 = \frac{\frac{K_{yR}}{M}}{\omega_B^2} \quad ,$$

$$\left(\frac{\omega_\eta}{\omega_B}\right)^2 = \frac{\frac{K_{\eta R}}{I_P}}{\omega_B^2} = \left(\frac{\omega_\xi}{\omega_B}\right)^2 = \frac{\frac{K_{\xi R}}{I_P}}{\omega_B^2} \; .$$

A shaft translation-pitching stiffness coupling parameter $\hat{k}$ also appears in the nondimensionalization. The parameter $\hat{k}$ appears in a manner that is analogous to the parameter μ_{TP}, which arises due to the fact that the origin of the coordinate system is centered at the disk centroid and not the center of mass of the system. This stiffness coupling $\hat{k}$ arises because the origin of the coordinate system does not

coincide with the axial location of the shear center. The shear center is defined as the point along the rotor centerline where the application of a transverse force does not result in any pitching deflection of the rotor, and the application of a pitching torque does not result in any transverse deflection. For a system in which the shaft stiffness is symmetric with respect to the x and y directions as seen in fig. 2.1, the nondimensional stiffness coupling parameter is defined:

$$\hat{k} = \frac{K^2_{x\eta R}}{K_{xR}\, K_{\eta R}} = \frac{K^2_{y\xi R}}{K_{yR}\, K_{\xi R}}$$

Applying this nondimensionaliztion scheme to the equations of motion (2.1.7) yield the nondimensional equation set (2.2.4). Also, the uncoupled zero nodal diameter cosine and n>1 nodal diameter sine and cosine blade modes nondimensionalize to:

$$\ddot{b}_0 + \left[\, 1 + \ell \left(\frac{\Omega}{\omega_B}\right)^2 \,\right] b_0 = 0 \qquad (2.2.5)$$

$$\ddot{a}_n + \left[\, 1 + \ell \left(\frac{\Omega}{\omega_B}\right)^2 \,\right] a_n = 0 \qquad (n>1) \qquad (2.2.6)$$

$$\ddot{b}_n + \left[\, 1 + \ell \left(\frac{\Omega}{\omega_B}\right)^2 \,\right] b_n = 0 \qquad (2.2.7)$$

$$
\begin{bmatrix}
1 & 0 & 0 & \sqrt{\mu_{TP}} & \sqrt{\frac{N}{2}\rho\mu_{TB}} & 0 \\
 & 1 & -\sqrt{\mu_{TP}} & 0 & 0 & \sqrt{\frac{N}{2}\rho\mu_{TB}} \\
 & & 1 & 0 & -\sqrt{\frac{N}{2}\rho\mu_{PB}} & 0 \\
 & & & 1 & 0 & \sqrt{\frac{N}{2}\rho\mu_{PB}} \\
 & & & & \frac{N}{2}\rho & 0 \\
 & \text{SYMMETRIC} & & & & \frac{N}{2}\rho
\end{bmatrix}
\begin{Bmatrix}
\frac{q_{xR}}{d} \\ \frac{q_{yR}}{d} \\ q_{\xi R} \\ q_{\eta R} \\ a_1 \\ b_1
\end{Bmatrix}''
+
$$

$$
2\frac{\Omega}{\omega_B}
\begin{bmatrix}
0 & -1 & \sqrt{\mu_{TP}} & 0 & 0 & -\sqrt{\frac{N}{2}\rho\mu_{TB}} \\
 & 0 & 0 & \sqrt{\mu_{TP}} & \sqrt{\frac{N}{2}\rho\mu_{TB}} & 0 \\
 & & 0 & 0 & 0 & 0 \\
 & & & 0 & 0 & 0 \\
 & & & & 0 & 0 \\
 & \text{SKEW-SYMMETRIC} & & & & 0
\end{bmatrix}
\begin{Bmatrix}
\frac{q_{xR}}{d} \\ \frac{q_{yR}}{d} \\ q_{\xi R} \\ q_{\eta R} \\ a_1 \\ b_1
\end{Bmatrix}'
+
$$

$$
\begin{bmatrix}
(\frac{\omega_x}{\omega_B})^2 - (\frac{\Omega}{\omega_B})^2 & 0 & 0 & \hat{k}\frac{\omega_x}{\omega_B}\frac{\omega_\eta}{\omega_B} & -\sqrt{\mu_{TP}}(\frac{\Omega}{\omega_B})^2 & -\sqrt{\frac{N}{2}\rho\mu_{TB}}(\frac{\Omega}{\omega_B})^2 & 0 \\
 & (\frac{\omega_y}{\omega_B})^2 - (\frac{\Omega}{\omega_B})^2 & \hat{k}\frac{\omega_y}{\omega_B}\frac{\omega_\xi}{\omega_B} & +\sqrt{\mu_{TP}}(\frac{\Omega}{\omega_B})^2 & 0 & 0 & -\sqrt{\frac{N}{2}\rho\mu_{TB}}(\frac{\Omega}{\omega_B})^2 \\
 & & (\frac{\omega_\xi}{\omega_B})^2 + (\frac{\Omega}{\omega_B})^2 & 0 & -\sqrt{\frac{N}{2}\rho\mu_{PB}}(\frac{\Omega}{\omega_B})^2 & 0 & \\
 & & & (\frac{\omega_\eta}{\omega_B})^2 + (\frac{\Omega}{\omega_B})^2 & 0 & -\sqrt{\frac{N}{2}\rho\mu_{PB}}(\frac{\Omega}{\omega_B})^2 & \\
 & & & & \frac{N}{2}\rho(1+\ell(\frac{\Omega}{\omega_B})^2) & 0 & \\
 & \text{SYMMETRIC} & & & & \frac{N}{2}\rho(1+\ell(\frac{\Omega}{\omega_B})^2) &
\end{bmatrix}
\begin{Bmatrix}
\frac{q_{xR}}{d} \\ \frac{q_{yR}}{d} \\ q_{\xi R} \\ q_{\eta R} \\ a_1 \\ b_1
\end{Bmatrix}
= 0
$$

(2.2.4)

Thus, for a symmetric rotor, there are nine nondimensional parameters in the full problem:

μ_{TP}	inertial term coupling disk translation and disk pitching motion
μ_{TB}	inertial term coupling disk translation and blade displacement
μ_{PB}	inertial term coupling disk pitching and blade displacement
ρ	ratio of blade modal mass to disk pitching moment of inertia
$\hat{k}$	stiffness term coupling disk translation and disk pitching
ω_x/ω_B	ratio of rotor uncoupled disk translational frequency at Ω=0 to isolated blade frequency at Ω=0
ω_η/ω_B	ratio of rotor uncoupled disk pitching frequency at Ω=0 to isolated blade frequency at Ω=0
Ω/ω_B	nondimensional rotor speed
ℓ	Southwell coefficient

The numerical values of these parameters for the MIT AE rotor are given in Appendix A. Typical values of some of these parameters for various generic types of turbomachinery are given in [9].

Den Hartog's analysis of a bladeless cantilevered rotor [7] can be thought of as a special case of the present model. His model describes the motion of a massive disk on a massless shaft using a rotating coordinate system with its origin located at the centroid of the disk. Shaft mass imbalance is therefore not included. Of course, blade flexibility effects are also not included. A further simplification is introduced by the use of a coordinate system rotating not at the rotor speed Ω, but at the asynchronous whirl rate ω. This transformation reduces the problem to one of only two degrees of freedom: a radial disk

deflection and a disk coning angle.

The Den Hartog approach to the simplified rotor yields only three nondimensional parameters: the "disk" effect $\tilde{D}$, the elastic coupling $\tilde{E}$, and the nondimensional speed $\tilde{S}$. In terms of the present nomenclature (for a symmetric rotor) they correspond to:

$$\tilde{D} = \frac{\frac{\omega_x}{\omega_B}}{\frac{\omega_\eta}{\omega_B}} = \frac{\frac{\omega_y}{\omega_B}}{\frac{\omega_\xi}{\omega_B}} \qquad (2.2.8)$$

$$\tilde{E} = \hat{k} = \frac{K^2_{x\eta R}}{K_{xR}\, K_{\eta R}} = \frac{K^2_{y\xi R}}{K_{yR}\, K_{\xi R}} \qquad (2.2.9)$$

$$\tilde{S} = \frac{\frac{\Omega}{\omega_B}}{\frac{\omega_x}{\omega_B}} \qquad (2.2.10)$$

The whirl frequencies of the Den Hartog model are the four roots of the characteristic polynomial:

$$\tilde{F}^4 - 2\cdot\tilde{S}\cdot\tilde{F}^3 + \frac{\tilde{D}+1}{\tilde{D}\cdot(\tilde{E}+1)}\tilde{F}^2 - \frac{2\cdot\tilde{S}}{\tilde{E}-1}\tilde{F} - \frac{1}{\tilde{D}\cdot(\tilde{E}-1)} = 0 \qquad (2.2.11)$$

where $\tilde{F}$ is the nondimensional frequency:

$$\tilde{F} = \frac{\frac{\omega}{\omega_B}}{\frac{\omega_x}{\omega_B}} \qquad (2.2.12)$$

Equation (2.2.11) is well known and has been used extensively in the design of cantilevered rotors. For a complete treatment of the dynamics of a bladed disk - shaft system, the fully coupled set of equations (2.2.4) should be considered. This higher order

model is required when the interaction criteria, discussed below, indicate appreciable interactions between the bladed disk vibration and the shaft whirling motion.

The normalized equations of motion (2.2.4) yield a convenient form for the evaluation of the criteria for interaction between the bladed disk dynamics and the shaft whirling motion. The basic question to be addressed is: under what circumstances is the interaction between the blade motion and the disk rigid body motion sufficient to warrant solving the fully coupled equations of motion. If the interactions are weak, then the bladed disk vibration and shaft-disk whirl problems may be solved as two simpler analyses. The propensity for interaction between the two motions is determined by the proximity of the shaft translation and pitch mode frequencies to the uncoupled blade frequency [9].

The procedure for assesing the strength of the interaction requires a knowledge of the uncoupled blade natural frequency and the uncoupled shaft natural frequencies (i.e. the frequencies of the shaft assuming the blades are rigid). An estimate of the shaft natural frequencies can be obtained by solving the 4x4 shaft motion submatrix in the upper left hand corner of eqn. (2.2.4). The resulting coupled shaft translation / pitch frequencies are ω_1 and ω_2, respectively. Therefore the criteria for propensity of interaction will be determined by the value of the two ratios: ω_1/ω_B and ω_2/ω_B being close to unity.

In the simple case of a rotor with relatively weak translation-pitch coupling, the frequencies ω_1 and ω_2 can be approximated by considering only the diagonal elements of the equations of motion. For a symmetric rotor with only disk translational degrees of freedom, the ratio of the disk to blade natural frequencies as a function of rotation rate is [9]:

$$\frac{\omega_1}{\omega_B} = \frac{\frac{\omega_x}{\omega_B} \pm \frac{\Omega}{\omega_B}}{\sqrt{1 + \ell \left(\frac{\Omega}{\omega_B}\right)^2}} = \frac{\frac{\omega_y}{\omega_B} \pm \frac{\Omega}{\omega_B}}{\sqrt{1 + \ell \left(\frac{\Omega}{\omega_B}\right)^2}} \qquad (2.2.13)$$

and for a rotor with only pitch degrees of freedom, the ratio of the disk to blade natural frequencies is:

$$\frac{\omega_2}{\omega_B} = \left\{ \frac{\left(\frac{\omega_\xi}{\omega_B}\right)^2 + \left(\frac{\Omega}{\omega_B}\right)^2}{1 + \ell \left(\frac{\Omega}{\omega_B}\right)^2} \right\}^{\frac{1}{2}} = \left\{ \frac{\left(\frac{\omega_\eta}{\omega_B}\right)^2 + \left(\frac{\Omega}{\omega_B}\right)^2}{1 + \ell \left(\frac{\Omega}{\omega_B}\right)^2} \right\}^{\frac{1}{2}} \qquad (2.2.14)$$

In gas turbines, the blade frequency ω_B is usually higher than the shaft-disk coupled translation/pitch frequencies ω_1 and ω_2 [9]. This implies that the uncoupled blade natural frequency is usually above the first two shaft critical speeds. In the case of the MIT AE rotor, the shaft stiffness and disk inertia are such that the pitch dominated mode is higher than the translation dominated mode. Hence, in this case, ω_2/ω_B is the relevant parameter for the propensity of interaction criteria. Note that the denominator of the ω_2/ω_B expression, eqn. (2.2.14), contains the term: $\ell(\Omega/\omega_B)^2$. Since in gas turbine blading the Southwell coefficient ℓ is usually greater than one, the interaction criteria ω_2/ω_B decreases with increasing rotor speed. Therefore, if the shaft-disk pitch and blade frequencies are well separated at zero rotation speed, then the modes will tend not to interact at higher rotor speeds. This effect can be seen schematically in fig. 2.3.

The magnitude of the interaction between the blade motion and the shaft whirl can be quantified by the degree of coupling between them. The influence of the coupling magnitude criteria μ_{TB} and μ_{PB} are discussed by Crawley and Mokadam [9]. The degree of coupling is also dependent on the ratio of the blade modal mass to the rotor pitching moment of inertia ρ. The

inertial coupling terms appear in eq. (2.2.4) as $N/2 \cdot \rho\mu_{TB}$ and $N/2 \cdot \rho\mu_{PB}$. The strong dependence of these terms on the cosine and sine of the effective stagger angle α is seen from the definitions of μ_{TB} and μ_{PB}, respectively. If the stagger angle α is zero, then the blade motion-disk translation inertial coupling parameter μ_{TB} is maximized and the blade motion-disk pitch inertial coupling parameter μ_{PB} is zero. If α is equal to 90^0, then μ_{PB} is a maximum and μ_{TB} is zero.

The term in the equations of motion (2.2.4) that indicates the magnitude of the gyroscopic coupling is:

$$2 \frac{\Omega}{\omega_B} \sqrt{\frac{N}{2} \rho\mu_{TB}}$$

The stiffness matrix in eq. (2.2.4) shows centrifugal coupling between the disk rigid body motion and blade displacement in the destiffening form:

$$- \frac{\Omega}{\omega_B}^2 \sqrt{\frac{N}{2} \rho\mu_{TB}} \quad \text{and} \quad - \frac{\Omega}{\omega_B}^2 \sqrt{\frac{N}{2} \rho\mu_{PB}}$$

These terms describe the magnitude of stiffness coupling and, like the inertial and gyroscopic coupling magnitude criteria, they have an implicit dependence on blade stagger angle.

The equations of motion of rotating flexible shaft-rigid disk-flexible blade rotor have been presented. They are expressed in both dimensional and nondimensional form. The relevant nondimensional parameters have been identified and their importance in determining the degree to which the bladed disk dynamics and the shaft whirling motion are coupled was explored. The subsequent chapters of this report will be concerned with identifying the system constants in the equations of motion for the MIT Aeroelastic Rotor and with the results of a series of experiments performed on the rotor to verify the analytical formulation.

3. Experimental Facilities

In order to experimentally document the bladed disk-shaft dynamic interaction of a typical fan, an extensive set of experiments were conducted, and the results compared with the model presented in Chapter 2. The experiments were carried out on the MIT Aeroelastic (AE) Rotor installed in the MIT Blowdown Compressor Facility of the MIT Gas Turbine Laboratory, which is depicted in fig. 3.1. The dynamics of the MIT AE bladed disk assembly have been documented by Crawley [8]. The use of this facility for transient testing of compressor stages for performance and aeroelastic response has been well documented [6,10]. Mokadam [5] also discussed the use of this facility for high speed rotor whirl testing in vacuum as a complementary facility to the low speed Whirl Spin Rig.

3.1) Rotating Assembly

An extensively instrumented rotor, the MIT AE rotor, was mounted in the test section of the Facility as seen in fig. 3.2a. The rotor is aerodynamically typical of modern high bypass ratio fans with: a blade hub to tip ratio of 0.5, a blade aspect ratio of 2, a design pressure ratio of 1.6, and axial and tip Mach numbers of 0.5 and 1.2 respectively. The structure and dynamics of the rotor has been fully described by Crawley [8] and Mokadam [5]. The rotor is cantilevered in the test section at the front of a shaft supported by two forward angular contact thrust bearings and a single rear spring loaded angular contact bearing. Flexible couplings forward and aft of the rotor-shaft system dynamically isolate the system from the forward slip rings and rear drive motor. The rotor was installed in the Blowdown Facility together with the forward slip ring assembly in order to be able to monitor the 23 blade piezoelectric blade root displacement transducer signals. A smaller rear set of slip rings

carried disk accelerometer and blade strain gage signals.

A degree of nonlinearity in the dynamic stiffness behavior of the shaft support had been observed in the low speed tests which used angular contact bearings. In order to reduce the degree of nonlinearity, initial planning called for the use of alternative bearing types such as Conrad roller bearings. However, in order to compensate for the thermal growth of the shaft during testing, the continued use of the spring preloaded angular contact bearings was indicated. It should be noted that even with ABEC-7 super precision bearings, the operating DN of the bearings exceeded their maximum rating for the lubrication available. The bearings therefore had a short life expectancy under the high speed test conditions. This required that the time spent testing at speed be kept as short as possible.

In order to maintain the cyclic bearing loads due to mass imbalance at a minimum, the rotor assembly was balanced prior to installation. The assembly was balanced according to ISO Grade G2.5 Gas Turbine Balancing Specifications, with a residual imbalance of less than 1 gram-inch in each of two balancing planes. Any loads due to this small residual imbalance would appear as steady loads in the rotor frame of reference and as a once per revolution periodic load in the nonrotating frame of reference.

With the balanced rotor installed in the test section, the forward slip ring assembly was then mounted. Considerable effort was expended to assure that the axes of rotation of the rotor and the slip ring assembly were aligned.

3.2) Instrumentation

The instrumentation associated with whirl testing of the MIT AE rotor in the Blowdown Facility included instrumentation on the rotor and on the nonrotating support structure. On the rotor, piezoelectric displacement transducers and semiconductor strain gages were used to monitor blade motion and miniature accelerometers measured accelerations of the disk in the plane of rotation. Instrumentation associated with the nonrotating frame of reference included accelerometers to monitor motion of the bearing support housing, and force transducers to measure the excitation forces applied to the bearing housing.

The blade piezoelectric displacement transducer configuration is shown in fig. 3.3. With the forward slip ring assembly installed, all 23 blade root piezoelectric displacement displacement transducers could be monitored. The rear set of slip rings carried signals from the three Bolt, Beranek and Newman (BBN) Model 501 miniature accelerometers. The three accelerometers were circumferentially mounted at 120° increments and were sensitive to motion of the disk in the plane of rotation. The rear slip rings also carried signals from two semiconductor blade strain gauges.

The disk accelerometers operated intermittently during rotating tests and produced noisy signals. Therefore the blade piezoelectric displacement transducers were used as the primary indicator of rotor response. In addition to their higher signal to noise ratio, the blade displacement transducers were sensitive to both in-plane translation as well as out-of-plane pitching motion of the disk. The disk accelerometers were only sensitive to disk in-plane translation motion, a serious limitation for detecting disk pitch modes. The disadvantage of using the blade transducers was that for the lower system modes, those well below the blade first bending frequency, a small amount of blade motion would occur for a relatively large amount of disk motion. Thus

the detectibility of disk motion by monitoring only the blade response was somewhat impaired.

A proximity sensor mounted in the center body was used as a tachometer. By sensing the passage of each the 115 teeth of a gear wheel mounted on the shaft, the tachometer produced a 115 per revolution signal. The tachometer signal was monitored with a frequency counter located at the rotor motor drive control panel.

During tests, which sometimes lasted up to 200 seconds, data were recorded using three different methods. The primary data logging device was a Hewlett-Packard (HP) 3960 FM Instrumentation tape recorder. This 4 channel instrument recorded 2 channels of forcing input (described in section 3.3) and 2 channels of blade displacement response. With these simultaneous measurements of input and response, system transfer functions could be determined. The second method of recording the data was an Ampex 14 channel FM tape recorder. This recorder was used as a redundant method of logging the forcing input and blade response data, as well as the tachometer signal.

After the test, the tape recorded analog data were played back into an HP 3582 dual channel spectrum analyzer for frequency domain inspection of the data. Graphical records were obtained by transferring the spectral data from the spectrum analyzer over an IEEE-488 bus into an IBM Personal Computer.

The third method of data logging was a direct digitization of up to 32 channels of data during the test. Because of memory limitations in the A/D system, only 200 ms of data could be digitized, using at a rate of 5 kHz per channel. This digitized data provided an instantaneous snapshot of the rotor system state at a particular speed and forcing frequency. This A/D system, manufactured by LeCroy Inc. and based on the CAMAC convention, was controlled by the MIT GTL PDP 11/70 computer. Post test signal processing of the digitized data was also performed on the 11/70 computer.

3.3) Whirl Excitation System

Some modifications to the test section were required in order to mount the rotor and whirl excitation actuators in the Blowdown Compressor Facility. The test section was machined in order to mount the two Ling 100 lb electromagnetic shakers on the casing, circumferentially 90 apart as seen in fig. 3.4a. The whirl excitation forces were transferred to the bearing housing of the test section via push rods connected to the shakers as seen in fig. 3.4b. The whirl excitation system employed in the blowdown facility was a modification of that used in the low speed whirl experiment [5].

Some trial and error was necessary in order to develop an appropriate experimental protocol for the whirl testing. Because of the potentially nonlinear response of the bearings, and the frequency shifting phenomena observed in the low speed rig data, any possibility of using impulsive or broadband excitation was discarded. Sine dwell type testing would be difficult because of the expected limited lifetime of the bearings. Therefore a slow sine sweep was chosen as the best system identification protocol.

Yet there still remained several detailed questions. Should a pure forward whirl, and then a pure backward whirl excitation be used, or some combination like a standing wave? Should the rotor speed be held constant and the excitation frequency swept, or should the excitation frequency be held constant and the rotor speed swept?

Due to the rather cumbersome manual control of the rotor speed, it was decided that it would be held constant, and the excitation would be swept in a controlled way. To simplify the data interpretation, a pure forward or backward whirl excitation would be used. The increased operator workload of the high speed testing required that the forcing sweep be automated. A Wavetek Model 184 sweep function generator supplied a linearly sweeping

signal between two preset frequency limits over a fixed duration. This frequency sweeping signal served two functions. It supplied the command signal to shaker #1 as shown in fig. 3.4a. It also supplied the phase and frequency reference signal to a Wavetek Model 186 phase lock sweep function generator. The phase lock generator would track the frequency of the input reference signal and would output a signal with the required predetermined phase shift. The output of the phase lock generator served as the command signal for shaker #2. The phase difference between the two signals was monitored with a Wavetek Model 750 phase meter. It was the preset phase angle that determined whether the excitation would excite either forward or backward whirl.

The outputs of the two function generators were input to two dedicated Altec Model 9440A 800 Watt amplifiers. The output of the amplifiers were passed through impedance matching transformers to the Ling Model 420 100 lb. shakers as seen in fig. 3.4a.

The shakers pushed on the bearing housing of the rotor through push rods instrumented with PCB Piezotronics Model 208 force transducers. The force transducers provided a direct measurement of the excitation force applied to the bearing housing. Due to air convection cooling and space considerations, the shakers were mounted on the outside of the test section casing. In order to apply the excitation forces to the bearing housing in the vacuum of the test section, dynamic O-ring seals isolated the segment of the pushrod inside the vacuum from that attached to the shaker as seen in fig. 3.4b.

Diametrically opposed to the push rod contact points on the bearing housing were two Endevco Model 7701 high sensitivity piezoelectric accelerometers. These allowed for a direct measurement of the response of the bearing housing centerbody to the applied excitation and other rotor dynamic loads.

Following the labelling convention shown in fig. 3.4b, the

forcing applied to the nonrotating bearing housing is of the form:

$$F_{N1} = F \sin \omega_{FN} t$$
$$F_{N2} = F \sin (\omega_{FN} t + \phi) \qquad (3.3.1)$$

If the phase of the force applied by shaker #2 leads the force applied by shaker #1 by 90 degrees ($\phi = 90^0$), then a clockwise rotating resultant force vector is produced. Since the rotor turns in the counter-clockwise direction, the resultant force vector rotates in the opposite direction or backwards with respect to the rotor. For a shaker forcing frequency ω_{FN}, the rotor senses this excitation at a shifted frequency ω_{FR}. The magnitude of the frequency shift is the relative angular speed between the nonrotating structure and the rotor, Ω. Since the rotor and the rotating force vector generated by the shakers rotate in opposite directions, the frequency shift in excitation sensed by the rotor is additive. The rotor is then excited with a backward whirl force at the frequency:

$$\omega_{FR} = \omega_{FN} + \Omega \qquad (3.3.2)$$

This corresponds to curve 1 in fig 3.5 which illustrates the forcing frequency shift as a function of rotor speed.

If the force applied by shaker #2 lags the force applied by shaker #2 by 90 degrees ($\phi = -90^0$), then a counterclockwise rotating resultant force vector is produced. In the case where the force vector is rotating faster than the rotor ($\omega_{FN} > \Omega$), the force vector is seen in the rotor reference frame to rotate in the direction of rotor rotation. This excites forward whirl and is sensed by the rotor at the frequency:

$$\omega_{FR} = \omega_{FN} - \Omega \quad . \tag{3.3.3}$$

This forcing condition corresponds to curve 2 in fig. 3.5.

The other possible forcing condition with $\phi = -90^0$ occurs when the rotor is turning faster than the rotating force vector ($\Omega > \omega_{FN}$). The force vector then seen in the rotor reference frame to rotate opposite to the direction of the rotor rotation. This excites backward whirl and is sensed by the rotor at the frequency:

$$\omega_{FR} = \Omega - \omega_{FN} \quad . \tag{3.3.4}$$

This forcing condition corresponds to curve 3 in fig. 3.5. Thus, by controlling the shaker excitation frequency ω_{FN} and phase angle ϕ of the signal generators, a forward or backward whirl excitation of known frequency ω_{FR} can be created in the rotor frame of reference.

In this chapter the experimental rig used to perform the structural dynamic whirl testing on the MIT AE Rotor in the Blowdown Compressor Facility and the whirl excitation system has been described. In the following chapters the identification of the system inertial and stiffness parameters and the results of a series of rotating whirl tests will be described.

4. Determination of Rotor Structural Properties

The prediction of the dynamic behavior of a rotating bladed disk on a flexible shaft system depends on an accurate knowledge of the structural properties of the system. This chapter describes the procedures employed in estimating and measuring the inertial and stiffness properties for the MIT AE rotor.

The system inertial parameters other than blade mass terms were determined by direct measurement of physical dimensions of components. Blade modal mass and mass coupling parameters were determined by calculations from holographic mode shape measurements. These mass calculations are described in section 4.1.

The stiffness properties of the system were much more difficult to determine. Direct static stiffness measurements of the shaft-bearing system yielded inconsistent results, as described in section 4.2. The approach finally used in determining these stiffnesses was to perform modal surveys of the nonrotating disk-shaft system and fit the dynamic data to a simple rigid disk-flexible shaft model. This approach is described in section 4.3.

4.1) System Mass Properties

The mass properties of the shaft-disk system were readily determined by a knowledge of component geometries and the material densities. The dimensions of each rotor part was found by direct measurement or, in some instances, by inspection of the dimensions on mechanical drawings.

The mass properties of the blades were determined by the holographic measurement of the blade cantilever bending mode shape at the midpoint of each grid cell on a 10x20 blade grid. This data, together with the measurement of the cell volumes were

applied to the integral definitions of m_0, m_1, m_2, and m_Ω given in section 2.1. The resulting inertial properties of the MIT AE rotor are listed in Appendix A.

4.2) Static Stiffness Tests

Determining the necessary stiffness terms consisted of determining the blade modal stiffness K_B and the effective shaft/support translation, pitch, and coupling stiffnesses K_x, K_η, $K_{x\eta}$. The blade modal bending stiffness K_B was determined from a knowledge of the isolated blade natural frequency of 374 Hz, the blade modal mass m_0, and the relation:

$$K_B = \omega_B^2 \, m_0 \quad . \tag{2.2.2}$$

Mokadam [5] describes attempts to measure effective bearing and shaft flexibilities of the low speed whirl spin rig by the application of static in-plane forces and out-of plane moments. These measurements entailed the use of dial gauges to measure the resulting small deflections. Subsequent tests involved the use of more sensitive inductive proximity sensors. Both series of tests displayed large scatter, low repeatibility and pronounced nonlinearity in the translation and pitch stiffnesses. These effects can be attributed to the difficulty of measuring the small resultant displacements and to the complex kinematics of angular contact ball bearings under the various loading states. When fitted to a straight line in order to approximate a linear stiffness, the data yielded compliance coefficients one or two orders of magnitude different from those required to reproduce the dynamic behavior of the system given the known mass properties. Further uncertainty would result in extrapolating the measurements taken on the low speed spin rig to the Blowdown Compressor Facility.

A different approach to determining the stiffnesses of the shaft-bearing system was therefore required. Dynamic nonrotating

modal surveys were seen as the most accurate possible method of measuring the effective stiffness coefficients of the MIT Aeroelastic (AE) rotor as mounted in the Blowdown Compressor Facility.

4.3) Nonrotating Dynamic Stiffness Determination

The technique employed in determining the dynamic stiffness properties was to calculate the effective stiffnesses for the system in the Blowdown Facility given the known mass properties and the measured shaft-disk natural frequencies and mode shapes. In the analysis necessary to back calculate these stiffnesses, the blades were assumed to be rigid bodies fixed to the disk hub. As a result, the data were fit to a model of a simple rigid disk on the end of a symmetric cantilever shaft as shown in fig. 4.1a. Let the two system degrees of freedom be defined as the in-plane translation of the disk (q_x) and the out-of-plane pitching of the disk about its diameter (q_η), as shown in fig. 4.1(a). With rigid blades, the homogeneous system equations of motion would then be:

$$\begin{bmatrix} M & S \\ S & I_p \end{bmatrix} \begin{Bmatrix} \ddot{q}_x \\ \ddot{q}_\eta \end{Bmatrix} + \begin{bmatrix} K_x & K_{x\eta} \\ K_{x\eta} & K_\eta \end{bmatrix} \begin{Bmatrix} q_x \\ q_\eta \end{Bmatrix} = 0 \qquad (4.3.1)$$

The testing for the two modes of the simplified system described by eq. (4.3.1) was accomplished by placing Endevco model 2222c miniature piezoelectric accelerometers on various points of the rotor while sweeping the excitation frequency of the electromagnetic shakers. The system resonances were noted as the frequencies at which the response peaked and the phase shifted abruptly through 90° during the forcing sweep.

In the modal testing, two shaft-disk modes were found, and are sketched in figures 4.1b and 4.1c. A certain degree of system

asymmetry was present, that is, the frequencies measured when the disk was excited in the x direction were not exactly identical with those measured in the y direction. These asymmetrical structural properties resulted in pairs of modes at similar but not identical frequencies but with approximately the same eigenvector. For the purposes of the fit of the nonrotating dynamic model of eq. (4.3.1) to the system stiffnesses, the system was assumed to be symmetric, and averages of the paired frequencies were used.

The low frequency mode was seen at 222 ± 5 Hz (the range representing the degree of asymmetry) and was characterized by a predominant disk rigid body translation motion in phase with disk pitching. The higher mode was found at 325 ± 5 Hz and consisted of a larger degree of disk rigid body pitching motion out of phase with disk translation. The experimentally measured modal vectors were determined to be:

$$\{\gamma_1\} = \begin{Bmatrix} q_x \\ q_\eta \end{Bmatrix} = \begin{Bmatrix} 0.123 \text{ m} \\ 1.00 \text{ rad} \end{Bmatrix}$$

$$\{\gamma_2\} = \begin{Bmatrix} q_x \\ q_\eta \end{Bmatrix} = \begin{Bmatrix} -0.054 \text{ m} \\ 1.00 \text{ rad} \end{Bmatrix}$$

A good test of the consistency of the experimentally observed mode shapes is to calculate their degree of orthogonality with respect to the "known" mass matrix. The experimental mode shapes were not strictly orthogonal with respect to the mass matrix of 2 DOF model. However, the normalized degree of nonorthogonality defined below, was on the order of 3%

$$\frac{(\{\gamma_1\}^T[M]\{\gamma_2\})^2}{\{\gamma_1\}[M]\{\gamma_1\}^T\{\gamma_2\}[M]\{\gamma_2\}} = 0.03 \qquad (4.3.2)$$

where γ^1 and γ^2 are the measured modal vectors, and M is the

mass matrix given in eq. (4.3.1).

With the two system modal frequencies and one independent modal vector (the other modal vector being redundant due to the need to satisfy the orthogonality condition) the three unknown stiffness terms in eq. (4.3.1) can be determined. The stiffness values that were determined by the fit of the nonrotating data to the simplified 2 DOF model are:

$$[K] = \begin{bmatrix} 8.10 \text{ N/m} & -5.29 \text{ N} \\ \text{SYM.} & 1.05 \text{ Nm} \end{bmatrix} 10^6$$

These stiffness values were subsequently used in the equations of motion to predict the behavior of the MIT Aeroelastic rotor system as a function of rotor speed.

In order to more thoroughly investigate the presence of asymmetries in the rotor and its mounting structure, nonrotating forced response sweeps were performed with the rotor shaft at various angular positions, and with the forcing vector directed at various angles. A useful feature of having two shakers which are mounted 90^0 apart on the circumference of the test section is that the vector sum of the shaker forces could be directed through the rotor center line at an arbitrary angle. This was accomplished by the proper selection of force amplitude and phase angle for each shaker. Note that this procedure was different than the whirl excitation scheme described in section 3.3. In that case the shakers were driving at equal forcing amplitudes and a $\pm 90^0$ relative phase angle.

The asymmetries could have been present in either the rotating assembly or in the nonrotating structure, or some combination of both. In order to determine if asymmetries were present in the nonrotating structure, forcing sweeps were performed with the resultant force vector acting at various angles with respect to top dead center of the test section. However the shaft was always rotated by the same amount as the

change in the forcing direction angle in order to maintain a constant relative angle between the shaft position and the forcing line of action. Since the forcing line of action was always constant relative to the rotor, any asymmtries in the nonrotating support structure would be apparent. Except when the direction of the applied force vector coincided with a nonrotating system principal direction, the response transfer function exhibited behavior typical of mistuned oscillators. The response shows showed two neighbouring peaks in the vicinity of the slightly different system frequencies. This indicates that there existed two principal directions for the stiffness of the nonrotating structure. The natural frequencies associated with each principal stiffness direction was slightly different.

The procedure for testing for asymmetries in the rotating system was more straight forward. The force application direction was maintained constant with respect to the nonrotating structure, while forcing frequency sweeps were performed at various rotor angular positions. Only a slight degree of asymmetry was detected in the rotating structure. This is to be expected since the rotating structure is an axisymmetric precision assembly while the rotor support structure consists of welded struts, casings, and supports that were not necessarily designed for elastic isotropy.

Response amplitude plots for disk motion as a function of forcing frequency are shown in fig. 4.2. These plots show the behaviour of the nonrotating disk pitch mode at constant load direction and rotor position. Figure 4.2a depicts the mistuned oscillator-type response for a forcing direction and rotor position that do not correspond to the principal directions of the system. Figure 4.2b shows the system behavior for a forcing direction aligned with one of the principal directions on the nonrotating structure and a rotor position aligned with a principal direction of the rotating system. The response

transfer function curve of fig. 4.2b indicates a single peak, more typical of the the response of a single degree of freedom system than that of fig. 4.2a

4.4) Numerical Model of a Whirling Rotor

As a method of predicting the natural frequencies of whirl of the MIT AE rotor in the Blowdown Compressor Facility, the equations of motion (2.1.7) were solved using with the experimentally determined mass and stiffness properties. The set of equations (2.1.7) are of the form:

$$[M]\{\ddot{x}\} + [G]\{\dot{x}\} + [K]\{x\} = \Omega \qquad (4.4.1)$$

Describing the system in state vector form:

$$\{y\} = \begin{Bmatrix} \{\dot{x}\} \\ \{x\} \end{Bmatrix} \qquad (4.4.2)$$

the normal modes were assumed to be of the form:

$$\{y\} = \{\phi\}\, e^{\lambda t} \qquad (4.4.3)$$

Upon substitution in eq. (4.4.1), the equations of motion are then in standard eigenproblem form:

$$[D]\{\phi\} = \frac{1}{\lambda}\{\phi\} \qquad (4.4.5)$$

where:

$$[D] = \begin{vmatrix} [0] & [I] \\ -[K]^{-1}[M] & -[K]^{-1}[G] \end{vmatrix} \qquad (4.4.5)$$

The system of equations (4.4.4) were solved using the well known EISPACK [11] library of matrix eigensystem solution subroutines. The entries of the dynamic matrix [D] depend on the rotation speed Ω, therefore the normal modes and frequencies were determined as a function of Ω. The behavior of the predicted system natural frequencies as a function of rotor speed is shown

in fig. 4.3a. The frequencies calculated from the equation are referred to the rotating frame, i.e. the rotor fixed coordinate system. The transformed natural frequencies, as they would appear in the nonrotating frame are shown in fig. 4.3b. Note that the forward and backward whirl curves still refer to whirl direction as viewed in the rotor frame. The shaft stiffnesses determined by the simple 2 DOF model fit of section 4.2 were used as well as the inertial properties listed in Appendix A.

The predicted system behavior depicted in fig. 4.3 was seen to differ from the experimentally observed natural frequencies when the rotor was not rotating ($\Omega = 0$). The low disk rigid body translation dominated mode which was experimentally observed at 222 Hz was calculated by the model to occur at 219 Hz. The high disk rigid body pitching dominated mode was experimentally observed at 325 Hz and was calculated at 315 Hz. The blade one nodal diameter mode was experimentally observed at 388 Hz and was predicted to occur at 408 Hz. These discrepancies can be seen by noting the experimentally observed frequencies in fig. 4.3a. The primary reason for the discrepancy between the observed and predicted $\Omega = 0$ natural frequencies is due to the fact that the stiffness parameters input to eq. (4.4.4) were determined by fitting the experimental disk rigid body dominated mode dynamic data to a 2 DOF model which did not include blade flexibility effects, eq. (4.3.1).The blade cantilever frequency of 374 Hz and the observed disk rigid body pitch dominated mode frequency of 325 Hz are in too close proximity to ignore the flexibility of the blades in the high disk mode motion. As a result the subsequent inclusion of blade flexibility in the system equations of motion (4.4.4) depresses the $\Omega = 0$ frequencies for the two lower modes which primarily consist of disk translation and pitch motion, while increasing the blade one nodal diameter frequency. The disk pitch mode was in closer proximity to the blade cantilever mode for $\Omega = 0$ than was the

disk translation mode. Hence the inclusion of the blade flexibility effects in the model depressed the disk pitch mode more than the disk translation mode.

Since the elements of the stiffness matrix were chosen to best fit the nonrotating modes, it was decided to further refine the fits using the full system model. This refinement will be done in two steps. First only the support stiffnesses will be modified, and later both the support and blade stiffnesses will be modified.

In order to obtain a more refined fit for the support stiffnesses, the measured frequencies used in the earlier fit were precompensated. This precompensation for the decrease in the frequency of the pitch mode predicted by eq. (4.4.4) was achieved by changing the dynamic data input to the 2 DOF stiffness fit from the experimentally measured values of 222 Hz and 325 Hz to 222 Hz and 335 Hz.

A second discrepancy in the prediction of the system natural frequencies shown in fig. 4.3a is the high rotor critical speed (defined as the point of intersection of the low forward whirl branch with the $\omega = 0$ axis). This point is experimentally known to occur in the vicinity of $\Omega = 215$ Hz. In order to precompensate for this difference, the coupling stiffness $K_{x\eta}$ was reduced by 35% from that predicted in section 4.2. The resultant K_x and K_η for a value of $K_{x\eta}$ chosen to be 35% less than the value used in fig. 4.3 was then calculated from eq. (4.3.1). The decrease in $K_{x\eta}$ corresponds to a decrease in the stiffness coupling parameter $\hat{k}$ from 0.331 to 0.164. The 2 DOF system stiffness matrix for the precompensated system is then:

$$[K] = \begin{bmatrix} 5.47\ \text{N/m} & -3.44\ \text{N} \\ \text{SYM.} & 1.32\ \text{Nm} \end{bmatrix} 10^6$$

This is approximately the best fit to the $\Omega = 0$ data that can be

made without modifying the blade stiffness.

The resultant system natural frequency behavior as a function of rotor speed is shown in figures 4.4a and 4.4.b. The effect of using the precompensated 2 DOF stiffness data in the full 6 DOF whirl model is a slightly better agreement for the disk pitch and translation modes at zero rotation speed. The $\Omega = 0$ disk translation mode is then predicted to occur at 220 Hz, which is in better agreement with the experimentally determined frequency of 222 Hz than the prediction using the baseline fit. Also, the $\Omega = 0$ disk pitch mode was predicted to appear at 317 Hz which agrees more closely with the measured mode at 325 Hz. However, the nonrotating blade one nodal diameter mode is further raised from 408 Hz, the prediction using the baseline stiffness fit shown in fig. 4.3a, to 416 Hz in fig. 4.4a. This error in predicting the $\Omega = 0$ blade one nodal diameter mode prompted another attempt to better fit the nonrotating data.

A second approach to precompensating the dynamic stiffness data follows in a manner similar to the first compensation scheme. In addition to the to the measures taken in the first scheme, the blade modal stiffness K_B determined by eq. (2.2.2) was decreased by 19% in order to precompensate for the incorrect prediction of the $\Omega = 0$ blade one nodal diameter modes at too high a frequency. The results of this final refinement are plotted in the rotor frame in fig. 4.5a and in the nonrotating frame of reference in fig. 4.5b. The results of this precompensated stiffness fit were used as the prediction of the system natural frequencies of whirl in order to assist in choosing the correct operating point for the whirl experiments. The correlation between the predicted and the experimentally determined frequencies for both the zero rotation speed and those speeds tested will be discussed in section 5.4. The results of the three stiffness fits are summarized in Table A.2.

Thus as a result of direct measurement of the inertial

properties and careful modal surveys of the rotor while not rotating, a complete set of system parameters have been found. Solving the system equations of motion with these parameters yields a reasonable prediction of the nonrotating behavior of the system and its the critical speed. The parameters are all internally consistent with the nonrotaing mode shapes, that is they satisfy the modal orthogonality relationships. In the next chapter the results of an experimental program of whirl testing on the MIT AE rotor will be discussed and the predicted and measured frequencies will compared.

5. Whirl Test Results

A program of experimental testing was carried out to determine the natural whirl frequencies of the MIT Aeroelastic rotor installed in the Blowdown Compressor Facility. The tests involved running the rotor at constant rotational speed while applying an excitation force phased to excite either forward or backward whirl. The response of the system was monitored by means of the blade piezoelectric displacement transducers. Peaks in the blade response amplitude were found to occur during the constant amplitude forcing sweeps. These resonant peaks were used to define the natural frequencies of the system.

The tests were performed at specific constant rotation speeds for both the forward and backward whirl excitation phasing. The rotation speeds chosen for study were: Ω = 30, 60, 90, 120, 150 Hz (1800, 3600, 5400, 7200, 9000 rpm). The data obtained up to and including Ω = 150 Hz was sufficient to illustrate the trends of the rotor system natural whirl frequencies with rotor speed, and to allow for comparison of predicted and experimental results.

Tests were also carried out at 5 Hz rotation speed in order to obtain a check of the nonrotating natural frequencies determined by this procedure with those reported in section 4.3 for Ω = 0. The natural frequencies at this low speed are only influenced slightly by the effects of rotation, hence the natural frequencies determined by the rotating instrumentation (the blade piezoelectric displacement transducers) were correlatable to the natural frequencies determined in the nonrotating modal surveys. The low speed tests were also useful in order to determine the observability of the modes of the system by the rotating instrumentation. Note that during the nonrotating modal surveys, discussed in section 4.3, it was possible to employ many shaft, disk, and blade mounted accelerometers in addition to the blade displacement transducers which comprised the rotating

instrumentation.

The technique employed for whirl testing is described in section 5.1. The verification of the successful excitation of the rotor in whirl is illustrated for both the forward and backward whirl case in section 5.2. The reduction of the forcing sweep data is shown in section 5.3, and the comparison between the predicted system frequencies and those experimentally measured is made in section 5.4. Finally, the experimental results are tabulated in Appendix B.

5.1) Whirl Test Procedure

The rotating whirl tests performed in the Blowdown Compressor Facility were essentially forced response tests using a slowly varying sinusoidal sweep technique. The natural modes of the rotor running at a constant speed were excited by sweeping in frequency, with the shakers set to force in a fixed whirl direction (forward or backward). During the development of the experimental technique single shaker, impulsive, and broadband excitation techniques were also evaluated. However due to the complex and possibly nonlinear response, clear interpretation of the data was best achieved using sine sweeps phased for pure forward or backward excitation.

An important consideration in devising the experimental procedure was that the total elapsed time during a test be kept as short as possible, especially at high speeds. This was done in order to minimize the run time on the bearings which, as previously discussed, were running above their DN rating. Bearing failures had previously occurred in the blowdown facility and, given the vigourous nature of the whirl forcing excitation, such an event was a major concern. In addition to influencing the test procedure, this concern for bearing life was what set the choice of a maximum test speed of ω = 150 Hz (9000 rpm). Another motivation for keeping test times short was to prevent the drive

motor from overheating. The motor temperature was monitored during the tests by a thermocouple on its casing.

At the beginning of a test run, the test section of the Facility was evacuated to a vacuum of approximately 0.1 mm Hg. During this pump down time the LeCroy A/D system was initialized and the desired forcing sweep range and sweep rate was set on the Wavetek Mod. 184 master sweep function generator. The Wavetek Mod. 186 phase lock slave function generator was set for the proper phase difference with respect to the Mod. 184 master sweep generator signal. These excitation signals were input to the two separate Altec 800W power amplifiers, the gains of which were set for the desired forcing amplitudes. Typical forcing amplitudes were measured at 80 lb_f (peak to peak) by the PCB Piezotronics force transducers.

When the desired vacuum was achieved the test would begin. The HP 3960 FM recorder and the Ampex FM recorder were set to start recording and the rotor was brought up to the desired rotational speed. When the target rotational speed was reached, the forcing sweep was started. Typically frequency sweep rates were approximately 1 Hz/s. During the sweep the rotor speed was maintained constant by manually correcting the motor input power and monitoring the tachometer. Typically the rotor speed was held stable within 0.5 Hz during a test run. At a predetermined forcing frequency during the sweep, the A/D was triggered and 32 channels of data were digitized at a rate of 5 kHz per channel for 200 ms duration. Of course the FM tape recorders were recording data during the entire test run. At the end of the forcing sweep the shaker excitation and the analog recorders were turned off. The rotor was stopped, and the A/D data was transferred to the PDP 11/70 computer for storage and later analysis.

After the test the primary data, the 2 force transducer and 2 blade displacement signals recorded on the HP recorder,

were played back and inspected on an oscilloscope to ensure that no loss of the primary instrumentation occurred during the run. One force transducer and one blade signal were played back into the HP 3582A spectrum analyzer for blade response amplitude inspection as a function of forcing frequency. Provided that the data appearred to be consistent, all the data was archived to await detailed data reduction. The data reduction procedure will be discussed in section 5.3.

5.2) Verification of Whirl Excitation Direction

The shaker excitation system described in Section 3.3 was designed to excite the rotor at any desired frequency and whirl direction, independent of the rotor speed. There remains the question of whether this excitation system was successful, and how pure the forward and backward whirl excitation was. This excitation process was monitored at four points: at the input to the shaker amplifiers (the output of the signal generators) by phase and voltmeters; at the input to the bearing housing centerbody by the the force transducers; by the response of the centerbody by two accelerometers; and by the response of the blades. By analyzing these signals, it will be shown that the target whirling modes and frequencies were successfully produced by the shaker system. The presence of the excitation patterns will first be shown for the forward whirl case, then for the backward whirl case.

5.2.1) Forward Whirl Excitation Case

As an example of the successful excitation of forward whirl motion, the case of the rotor turning at Ω = 120 Hz (7200 rpm) will be considered. The response of the bearing housing centerbody will first be examined, then the displacement of the blades will be shown. The time history of the forces applied to the bearing housing centerbody are shown in fig. 5.1a. The

shakers are each applying a sinusoidal force at the frequency ω_{FN} = 449 Hz and are phased such that the force applied by shaker #2 lags that of shaker #1 by 90°. This corresponds to a phase angle ϕ of -90° in eq. (3.3.1), and therefore a forward whirl excitation. As can be seen from the excitation system configuration diagram in fig. 3.4b, this ϕ = -90° excitation pattern produces a resultant force vector that rotates at a frequency of ω_{FN} = 449 Hz in the direction of the rotor as viewed in the nonrotating frame.

The spectral content of the signals from the force transducers are shown in fig 5.2. The plots, which were produced by power spectral density (PSD) software on the PDP 11/70, are the frequency domain representation of the signals shown in fig. 5.1a. The plots both show peaks of nominally equal magnitude at exactly at the forcing frequency of ω_{FN} = 449 Hz. Therefore the force applied to the system by the two shakers exactly follows the commanded force, i.e. two force components of equal amplitude, a -90° phase difference, and of a single pure harmonic content of the desired excitation frequency.

Next the response of the nonrotating bearing housing centerbody to this excitation will be examined. The acceleration response of the bearing housing centerbody is shown in fig. 5.1b. The signal from accelerometer #2 (located diametrically opposite to shaker #2) lags the signal from accelerometer #1 (located diametrically opposite to shaker #1) by about 90°. This indicates that the nonrotating structure did respond to the excitation force vector, which was rotating in the direction of the rotor at a speed of ω_{FN} as seen in the nonrotating frame. However note that the response amplitude of accelerometer #1 was about three times greater than that of accelerometer #2. Thus the bearing housing centerbody moved along a nominally elliptical pattern in the direction of the rotor at an inertial angular rate of ω_{FN}.

Similarly, the power spectral densities of the bearing housing accelerometer signals are shown in fig. 5.3. A sharp spike is seen in the PSD of accelerometer #1 at ω_{FN} = 449 Hz while the corresponding spike on the PSD of accelerometer #2 is only about one ninth the magnitude. This is because the acceleration amplitude of the two accelerometer signals differed by a factor of three and the PSD amplitude is proportional to the square of the signal amplitude. This verifies that the bearing housing centerbody did respond in a forward whirling motion at a frequency equal to the excitation frequency, although in an elliptic rather than circular pattern. The reason for this preferential direction is suspected to be associated with a nonuniformity of the centerbody support structure in the Blowdown Facility. Other peaks in the PSD amplitude traces can be seen at integer multiples of the rotor speed Ω, primarily at $\omega_R = \Omega$. The additional once per revolution response is of course due to the slight residual imbalance of the rotor exciting the support structure at the rotation speed.

Having established that the nonrotating centerbody responds to the whirl excitation at ω_{FN}, it remains to be determined how the excitation is viewed in the rotating system and how the blades respond. The transformation of forces from the nonrotating to the rotating system was discussed in section 3.3 and summarized in fig. 3.5. The case being considered is: shaker phase angle $\phi = -90^0$, shaker excitation frequency ω_{FN} = 449 Hz, and a rotor speed of Ω = 120 Hz (7200 rpm). Since the inertial forcing frequency ω_{FN} is greater than the rotor speed Ω, the rotating assembly should sense a rotating force vector at a frequency of: $\omega_{FR} = \omega_{FN}-\Omega$ = 329 Hz and rotating in the direction of rotor rotation as viewed in the rotor frame. This corresponds to a point on curve 2 of fig. 3.5, which is the forward whirl excitation characteristic. The characteristics to establish this specific point are shown in fig. 5.4, superimposed

on the predicted system resonance plot of fig. 4.5a. Thus one would expect the blades to respond at ω_{FR} = 329 Hz in a one nodal diameter forward whirl pattern.

The time response of the blade piezoelectric displacement transducers to the excitation pattern are shown in fig. 5.5 in their correct relative angular positions on the rotor hub. The signal from blade displacement transducer #1 is repeated after the signal from blade transducer #23 for reference. These response signals were recorded simultaneously with the excitation signals by the LeCroy A/D. By inspection, it can be seen that the dominant displacement pattern of the blades is a one nodal diameter mode with a nominal interblade phase angle of: $\beta \simeq 360^0/23$ blades = 15.7^0 and the sense of the travelling wave is in the forward whirl direction. Therefore the blades are responsing to the forward whirl excitation. Note that the signal from blade displacement transducer #2 is null because its wire insulation in the forward slip ring assembly was damaged, and the signal was shorted to ground. Constraints in the Facility test schedule did not permit a shutdown to remove the slip ring assembly and repair the wire.

In order to determine the frequency content of the blade response, the power spectral density of a typical blade displacement transducer (#9) is shown in fig. 5.6. A large peak is seen at the frequency of the excitation in the nonrotating frame of 449 Hz (all blade signal frequencies are referred to as frequencies observed in the rotor frame). Response is also seen at the target forcing frequency: $\omega_{FR} = \omega_{FN}-\Omega \simeq 327$ Hz. A small peak is also seen at the frequency at which backward whirl would be sensed in the rotating frame: $\omega_{FN}+\Omega \simeq 571$ Hz. Two possible mechanisms for the appearance of these undesired whirl response frequencies are: responses stemming from asymmetries in the bearing support structure and amplitude differences between the two shaker forces during the excitation sweep.

For a rotor system with stiffness asymmetries in both the nonrotating structure and in the rotating assembly, the resulting equations of motion expressed in any coordinate system will involve periodic coefficients. The forced response or nonhomogeneous solutions to periodic forcing inputs can be seen, by Floquet or harmonic balance methods [12], to involve frequency components shifted from the forcing frequency by harmonics of Ω. For a forward whirl excitation, a symmetric linear system would respond at the freqency of excitation ($\omega_{FN}-\Omega$), but a nonsymmetric system would also respond at: $\omega_{FN}-2\Omega$, ω_{FN}, $\omega_{FN}+\Omega$, etc. . Although the system asymmetries were relatively weak in the rotating structure and slightly more apparent in the nonrotating structure, this effect may be the cause of the unexpected response frequencies.

Blade frequency response shifts due to amplitude differences in the shaker output forces are readily explained within the realm of linear theory. Consider a forcing input to the bearing housing centerbody with a fractional amplitude difference 2e between each shaker:

$$F_{N1} = (1+e)\ f\ \sin\omega_{FN}t$$

$$F_{N2} = (1-e)\ f\ \sin(\omega_{FN}t+\phi)$$

For the case of forward whirl with $\omega_{FN} > \Omega$ and $\phi = -90^{\circ}$, the rotor senses the following excitation pattern:

$$F_{R1} = f\ \sin(\omega_{FN}-\Omega)t + ef\ \sin(\omega_{FN}+\Omega)t$$

$$F_{R2} = -\ f\ \cos(\omega_{FN}-\Omega)t + ef\ \cos(\omega_{FN}+\Omega)t$$

Therefore a component of backward whirl of magnitude ef and frequency $\omega_{FN}+\Omega$ exists in the rotor excitation as sensed in the rotating frame. Thus a response is to be expected at this frequency if the shakers are not producing equal force amplitudes, or in an analogous manner, the bearing centerbody does not respond with equal receptance to a symmetric excitation

pattern. It was shown in fig. 5.1b that the centerbody responded with unequal amplitudes in the two orthogonal directions in spite of the nominally equal excitation amplitudes. Therefore a possible mechanism for the blade response at the undesired whirl frequency, the frequency corresponding to backward whirl, is the unequal response amplitude of the bearing housing centerbody to the forward whirl excitation.

In the power spectral density plot of the displacement response of blade #9, shown in fig. 5.6, it is evident that the blade is also responding at harmonics of the rotor speed Ω. The response at integer "engine" orders is quite significant, with a large PSD spike at $2\Omega \approx 244$ Hz and smaller spikes at: $1\Omega \approx 122$ Hz, $3\Omega \approx 366$ Hz, and $4\Omega \approx 483$ Hz. The origin of this excitation is somewhat uncertain. It is certainly due to some interaction of the rotating and nonrotating frames since it clearly occurs at multiples of the rotor speed. It could be due to bearing noise or a complex interaction of the rotor imbalance with the nonuniform nonrotating centerbody support structure.

The overall conclusion is that the forward whirl excitation is indeed sensed by the rotor, but due to nonuniformity of the support and the presence of additional excitation sources, the signal-to-noise ratio of the desired response of the blade compared to the total response is not good (clearly less than one in this case). Therefore in the data reduction process, great care must be taken to identify the response associated with each excitation source. Then only the response associated to the desired whirl direction should be considered in the determination of the system resonances.

5.2.2) Backward Whirl Excitation Case

In a procedure parallel to that of the previous subsection, the results of a backward whirl excitation will be traced from the shakers, through the bearing housing centerbody, and ultimately to the blade response. The particular case of a rotor speed Ω = 60 Hz (3600 rpm) run will be discussed to illustrate the backward whirl response. The shaker input signals are instantaneously commanding a backward whirl excitation at ω_{FN} = 290 Hz. The time history of the force transducer signals as logged by the A/D system are shown in fig. 5.7a. The shakers are phased such that the force exerted by shaker #2 leads that of shaker #1 by 90°. This corresponds to a phase angle ϕ = 90° as defined in eq. (3.3.1) and a backward rotating force vector as viewed in both the nonrotating and rotor frames. The spectral content of the shaker force transducer signals are shown in fig. 5.8. A pair of sharp peaks are seen at the forcing frequency of ω_{FN} = 290 Hz. The two peaks are of nominally equal amplitude, indicating again that a pure uniform force vector is produced by the excitation system.

The acceleration response of the bearing housing centerbody to the applied shaker forcing is shown in fig. 5.7b. The signal from accelerometer #2 is seen to nominally lead that from accelerometer #1 by 90°. Upon inspection of the excitation system layout shown in fig. 3.4b, the vector sum of the two acceleration vectors (and hence displacement vectors), is seen to rotate in a direction opposite to that of the rotor. The two acceleration signals are of similar amplitude, thus the bearing housing centerbody executes a nominally circular backward whirling motion. The power spectral density of the accelerometer signals is shown in fig. 5.9, where again a relatively clean response at ω_{FN} = 290 Hz is seen. Note that the slight difference in excitation force amplitude between shaker #1 and #2 is reflected by a consistent slight difference in centerbody

response amplitude (fig. 5.9), in both cases the 2 direction responding with slightly less amplitude than in the 1 direction. This is an indication that at this frequency, the centerbody support structure is approximately symmetric.

The frequency and sense of the excitation must again be transformed to the rotor frame. In this case the force vector applied by the shaker system rotates at an angular rate of ω_{FN} = 290 Hz opposite to the direction of rotor rotation, viewed in the nonrotating frame. Following the discussion of section 3.3, for a rotor speed Ω = 60 Hz, the rotor should sense an applied force vector rotating opposite to the direction of rotor rotation at an angular rate of $\omega_{FN}+\Omega$ = 350 Hz, as viewed in the rotor frame. This corresponds to a point along curve 1 of fig. 3.5, the force transformation summary plot.

The simultaneous time response of the blade displacement transducers can be seen in fig. 5.10. The blades are shown in their correct relative angular position on the rotor hub with the signal from blade transducer #1 repeated after that of blade transducer #23. The blades are executing a one nodal diameter motion with a nominal interblade phase angle of $\beta \simeq -15.7^{0}$, corresponding to a backward whirl motion. A typical blade displacement signal PSD, specifically for blade #12, is shown in fig. 5.11. The PSD clearly shows that the blades are responding at a frequency of ω_{FR} = 350 Hz, which corresponds to backward whirl excitation. Comparison of fig. 5.11 and fig. 5.5 indicates that the backward whirl motion was excited in a more pure manner than was the forward whirl motion.

Further inspection of fig. 5.11 reveals the presence of peaks in the PSD of the blade response at frequencies other than the excitation frequency ω_{FR}. These peaks are of relatively low amplitude compared to the response forced at ω_{FR}. One low amplitude PSD spike is seen at the rotor speed: 1Ω = 60 Hz, which is excited by the mechanisms discussed in section 5.2.1. Two

other peaks are also seen, one at 386 Hz and another with a higher amplitude at 406 Hz. It will be seen in section 5.3 that these two response frequencies correspond to the Ω = 60 Hz one nodal diameter blade forward and backward whirl natural frequencies, respectively. The response observed at these system natural frequencies are probably due to broadband background noise excitation. The response of the backward whirl mode at 406 Hz is of the greater amplitude and its effect can be seen as a beating signature on the time response of the blades. By contracting the time scale on a single trace of fig. 5.10, this beating can be seen. This is shown in fig. 5.12, where the response of blade displacement transducer #12 is shown with a the time axis contracted by a factor of four in comparison to the axis in fig. 5.10. The beating is due to the proximity of the forcing frequency ω_{FR} = 350 Hz to the natural frequency of the one nodal diameter backward whirl mode (ω_{BB}) of 406 Hz for a rotor speed of 60 Hz. The envelope of the beating signal has a frequency of:

$$\omega_{beat} = \frac{\omega_{BB} - \omega_{FR}}{2} = 28 \text{ Hz}$$

which agrees well with the graphically measured beat frequency of 29 Hz.

Therefore it can be seen that the signal-to-noise ratio of the backward whirl blade response compared to blade response at other frequencies is on the order of ten, much greater than that obtained for the forward excitation case. Therefore the excitation system is seen to be very effective at selectively exciting backward whirl response and somewhat less effective for forward whirl.

5.3) Whirl Spectral Data

In order to determine the natural frequencies of whirl for the rotor at speed, the signals recorded on the HP 3960 recorder were analyzed in the frequency domain. Two of the four recorder channels were the force transducer signals representing the controlled excitation applied to the system. The two other channnels were two of the blade piezoelectric displacement transducers which represented the response of the system to the shaker input. These tape recorded signals were the most useful of the data because they were continuous records of the input to and the response of the rotor system. In contrast, the A/D data provided only a "snapshot" of the rotor state at one instantaneous forcing frequency. By transforming the tape recorded data into the frequency domain, the system transfer functions could be inferred as a function of rotor speed and whirl direction. These peaks in the blade response transfer functions were used to define the natural frequencies of the rotor.

5.3.1) Spectral Data Reduction Scheme

The transformation of the data to the frequency domain was achieved by playing back the tape recorded data into the HP 3582A spectrum analyzer. The spectrum analyzer performs fast Fourier transforms (FFT) upon its input and provides graphical display of the FFT magnitude record on its video display. The FFT record could also be read from the spectrum analyzer over an IEEE-488 bus into an IBM Personal Computer for storage and subsequent plotting. Since the spectrum analyzer had only two channels, only one force transducer and blade displacement transducer signal were transformed into the frequency domain.

This procedure allowed for an input-output transfer function to be constructed by plotting the relevant peak in the FFT of the blade displacement response as a function of the forcing frequency. For a particular blade response FFT, the

corresponding excitation frequency was determined from a simultaneous FFT of the force transducer signal. As discussed in section 3.3 and summarized in fig. 3.5, there is a frequency shift in the excitation sensed by the rotating assembly compared to the forcing frequency exerted on the nonrotating bearing housing. Therefore the system excitation, which is measured in the nonrotating frame of reference by the force transducers, must be shifted in the frequency domain in order to determine the spectral content of the forcing input to the rotating system.

The frequency domain data reduction scheme is summarized in fig. 5.13. For a particular test case the rotor speed Ω and the whirl excitation phase angle ϕ are held constant. The forcing frequency is swept at a relatively low rate in comparison to the frequencies being excited. Therefore during a data sampling window for the spectrum analyzer, the forcing frequency ω_{FN} was essentially constant. This is illustrated in fig. 5.13a where the time record of the shaker output is shown. A simultaneous sample of the blade response signal over the same sample window is shown in fig. 5.13b. The force transducer signal of fig. 5.13a is transformed by the spectrum analyzer into the FFT plot of fig. 5.13c. The forcing FFT plots are typically characterized by a single clean peak at the shaker forcing frequency of ω_{FN} and, since the amplitude of the forcing is maintained constant during a sweep, the amplitude of the FFT peak is constant over the sequential sample windows. The corresponding blade response FFT is shown in fig. 5.13d. In the example shown, the case of forward whirl excitation is depicted, therefore the desired response is expected at $\omega_{FR} = \omega_{FN}-\Omega$. Again the frequency components of the blade signals are referred to the rotor frame and the frequency components of the force transducer signals are with respect to the nonrotating or inertial frame. As discussed in section 5.3 there are other frequency components in the blade response, specifically at harmonics of the rotor speed, ω_{FN},

and the undesired whirl direction (in this case at $\omega_{FN}+\Omega$).

As the window over which the FFT samples are taken is shifted along the time axis of figures 5.13a and 5.13b, the forcing frequency increases according to the sweep rate commanded by the function generators at the time of the test. By sequentially performing FFT's on the shaker force and blade response signals, the spectral cascade plots of figures 5.13e and 5.13f are produced. The cascade plot of the shaker forcing input, fig. 5.13e, shows the sweeping forcing frequency ω_{FN} as a clean frequency component peak that translates along the frequency axis according to the sweep rate. The desired blade response frequency component, in this example the forward whirl component at $\omega_{FR} = \omega_{FN}-\Omega$, also translates along the frequency axis of the cascade plot of fig. 5.13f. The amplitude of the blade frequency component corresponding to the target response of forward whirl is then plotted as a function of excitation frequency ω_{FR}, referred to the rotor frame. Since the amplitude of the excitation was constant over a sweep, a blade response transfer function such as fig. 5.13g can be constucted by plotting the amplitude of the Fourier component at ω_{FR} versus the excitation frequency ω_{FR}. The peaks in the transfer function are assumed to correspond to natural frequencies of the rotor system, at the given set of rotor speed and whirl phasing conditions.

Because each test is performed at a constant shaker phase angle ϕ, then only three of the six system modes should be excited by the forcing sweep. The modes that are excited are those with mode shapes of whose direction correspond to that of the whirl excitation. Also, because each test is performed at a constant rotor speed, the transfer function plot occurs along a constant speed (vertical) line in a system response plot such as fig. 4.3. This is shown for the forward whirl case in fig. 5.13h, where the transfer function is overplotted as a vertical trace on the system natural frequency plot. The peaks of the transfer

function plot define the system natural frequencies for those particular test conditions. By varying the rotor speed and performing tests with the shakers phased for both forward and backward whirl, the experimental system natural frequency (in the rotor frame) plot can be constructed. This data reduction scheme will be applied to the forward whirl excitation data, then to the backward whirl excitation data in the next two subsections. The results of the data analysis will be overplotted on a system natural frequency plot and tabulated in Appendix A.

5.3.2) Forward Whirl Spectral Data

The spectral response data from the forward excitation tests will be examined by analyzing the HP 3960 tape recorder data according to the procedure outlined in the previous subsection. The data will be presented in the form of cascade plots of the blade response power spectral density as in fig 5.14. Each trace on the cascade plot corresponds to a single excitation frequency ω_{FR}, which is referred to the rotor frame. All of the traces on a given cascade plot are for the same rotor speed and whirl phasing. The range of experimentally applied excitation frequencies for some of the forward whirl data are graphically shown as vertical bars on the predicted system frequency plot shown in fig. 5.27.

The cascade plot of fig. 5.14 depicts the blade spectral response for the case of a rotor speed of Ω = 30 Hz, forward whirl shaker phasing, and an excitation frequency range of ω_{FR} = 365 to 397 Hz. This range of excitation is in the neighbourhood of the blade one nodal diameter forward whirl mode at this speed and is graphically shown on the system frequency plot of fig. 5.27. The traces of the cascade plot of fig. 5.14 show that the blade response contains a dominant frequency component at the desired response, ω_{FR}, and a smaller response at ω_{FN}. The response peak at ω_{FR} is a maximum for the

excitation frequency trace of ω_{FR} = 379 Hz and the signal-to-noise ratio of the desired response frequency component is about four for that trace. Upon inspection of the data at smaller intervals of excitation frequency, a more precise location of the blade one nodal forward whirl mode at Ω = 30 Hz is found to be at 378 Hz. This provides one data point for the system natural frequency plot of fig. 5.37.

The cascade plot of fig. 5.14 is summarized in the system transfer function plot of fig. 5.15. The plot depicts blade response amplitude as a function of forcing frequency ω_{FR} for a constant forcing amplitude, rotor speed, and whirl phasing direction. Only the two higher forward whirl modes are shown, since the disk rigid body translation mode appears below the frequency range of fig. 5.15. The resonant peak for forward whirl blade one nodal diameter motion at 378 Hz is very sharp indicating that the observability of the blade modes is relatively much greater than that of the disk rigid body modes. In fact the blade response to the disk forward whirl rigid body pitching modes has such a low signal-to-noise ratio that it was very difficult to determine the experimental natural frequencies of this mode. Therefore this mode does not appear in the experimental data overplot on the system natural frequency plot of fig. 5.37. As will be seen in this section, the disk forward whirl rigid body translation modes were discernable only after careful inspection of the data because of the poor signal-to noise ratio of the blade response at that frequency range.

The difference in amplitude within the transfer function plots such as fig. 5.15 is primarily because the sensors used to monitor the system response were piezoelectric displacement transducers The transducers are specifically sensitive to blade motion, hence blade displacement modes are more observable than the disk rigid body translation and pitching modes. This difference in the observability of the blade displacement and

disk rigid body motion will be apparent in all the rotating data, and it will affect the ability to detect the disk rigid body modes with a high degree of certainty.

The cascade plot of blade response for the case of: forward whirl excitation, rotor speed Ω = 60 Hz (3600 rpm), and excitation frequency range of ω_{FR} = 130 Hz to 172 Hz is shown in fig. 5.16. The rotor operating point and excitation range corresponding to this cascade plot are sketched on the system frequency plot of fig. 5.27. This cascade plot contains many frequency components other than the target forced response at $\omega_{FR} = \omega_{FN}-\Omega$. The spectra show response peaks at the frequencies ω_{FN} and at $\omega_{FN}+\Omega$, the frequency at which a backward excitation would appear. These undesired response peaks are often of larger amplitude than the desired forward whirl response, indicating that a poor signal-to-noise ratio was achieved. Harmonics of the rotor speed Ω also appear, with the fourth harmonic response approaching 30% of the amplitude of the forward whirl forced response. In spite of the difficulty in attaining a pure forward response pattern, a peak in the forward whirl cascade plot is seen on the trace corresponding to the excitation frequency ω_{FR} = 150 Hz. Further analysis of the tape recorder data indicate that the exact position of the peak response occurs between the spectrum traces of ω_{FR} = 144 Hz and 150 Hz, specifically at ω_{FR} = 146 Hz. Therefore this is the natural frequency of the disk rigid body translation mode at a rotor speed of Ω = 60 Hz.

The cascade plot corresponding to the same operating conditions (forward whirl and Ω = 60 Hz) as fig. 5.16, but at the higher excitation frequency range of ω_{FR} = 374 Hz to 402 Hz is shown in fig. 5.17. This excitation frequency range is in the neighbourhood of the blade one nodal diameter forward whirl mode. The response of the blade is seen to be much cleaner than in fig. 5.16, with the peaks corresponding to ω_{FR} being the only

significant ones and the response amplitudes are of much higher amplitude as can be seen in the transfer function plot of fig. 5.18. In the cascade plot of fig. 5.17, the resonance peak can be seen on the ω_{FR} = 386 Hz trace. This corresponds exactly with the peak on the transfer function plot which was determined at much finer intervals of excitation frequency. Therefore the blade one nodal diameter forward whirl mode is seen to occur at a frequency of 386 Hz, in the rotor frame of reference. Again, this higher response amplitude of the blade one nodal diameter modes is due to their higher observability than the disk rigid body dominated modes.

Another example of a cascade plot in the neighbourhood of the disk rigid body translation dominated mode is shown in fig. 5.19. This plot corresponds to the case of forward whirl excitation of the rotor at a speed near Ω = 90 Hz, specifically 91.3 Hz. The spectral content of this cascade plot is similar to that seen in fig. 5.16, the previous forward whirl cascade plot in the vicinity of a disk rigid body dominated mode. The response at the target forward whirl frequency is seen to occur at a slightly lower amplitude than the responses at ω_{FN} and $\omega_{FN}+\Omega$. There is also an appreciable amplitude of response at harmonics of the rotor speed. Therefore a poor signal-to-noise ratio was achieved in driving the target response frequency. The forward response does peak in the vicinity of the 112 Hz trace, specifically at ω_{FR} = 114 Hz. therefore the disk forward whirl rigid body disk transaltion mode at a rotor speed Ω = 91.3 Hz is determined to be 114 Hz in the rotor frame of reference. The blade response transfer function plot for this case of a rotor speed $\Omega \simeq$ 90 Hz (91.3 Hz) and forward whirl phasing is shown in fig. 5.20.

Forward whirl response cascade plots for the rotor speed of Ω = 120 Hz and the excitation ranges of ω_{FR} = 73 Hz to 99 Hz and ω_{FR} = 444 Hz to 468 Hz are shown in figures 5.21 and 5.22

respectively. Figure 5.21 depicts the blade spectral response in the neighbourhood of the disk rigid body translation dominated mode. As is typical of the lower disk modes, the response at the undesired response frequency ω_{FN} is of larger amplitude relative to the target response frequency $\omega_{FR} = \omega_{FN}-\Omega$. Also, harmonics of the rotor speed Ω appear in the spectral content of the blade response. These undesired response frequencies combine to result in a poor signal-to-noise ratio. The peak in the response at ω_{FR} is seen in the vicinity of the 85 Hz trace. Further inspection at smaller excitation frequency increments yields a resonant frequency for the forward whirl disk rigid body translation dominated mode of 84 Hz, as seen in the transfer function plot of fig. 5.23. Figure 5.22 depicts the response in the vicinity of the blade one nodal diameter forward whirl mode. In addition to the response at ω_{FR}, a significant response at the third and fourth harmonics of the rotor speed are seen. The spectra indicate a resonance in the neighbourhood of ω_{FR} = 456Hz, and upon closer inspection the one nodal diameter forward whirl blade mode is seen at 454 Hz as shown in the transfer function of fig. 5.24. This resonance is also seen to be excited by broadband background excitation during the experiment as can be seen on the ω_{FR} = 476 Hz trace of fig. 5.22.

The disk rigid body translation dominated mode cascade plot for the forward whirl, Ω = 150 Hz case is shown in fig. 5.25. It can be seen from the plot that the signal-to-noise ratio of the desired response is decreased by the presence of frequency components at ω_{FN} and at 1Ω. The peak response at the forward frequency is seen near ω_{FR} = 62 Hz. The transfer function corresponds to this range of excitation frequency is seen in fig. 5.26, where the more precise location of the forward whirl disk rigid body translation mode is seen at 60 Hz.

The operating points for the spectral response data to the forcing sweeps are all depicted graphically in fig. 5.27.

The correlation of the experimentally determined natural frequencies to those predicted by the model developed in Chapter 2 will be discussed in Section 5.4.

5.3.3) Backward Whirl Spectral Data

The cascade plot spectral data and blade response transfer function results of some of the backward whirl tests will be be presented in this subsection. The operating point and excitation range that corresponds to each cascade plot will be overplotted on a system natural frequency plot in fig. 5.36.

The cascade plot for the case of: backward whirl excitation, a rotor speed Ω = 5 Hz, and an excitation in the range of the disk rigid body pitching mode is shown in fig. 5.28. The spectral content of each of the traces is essentially a pure backward whirl response at $\omega_{FR} = \omega_{FN}+\Omega$. The resonant peak is seen to occur in the vicinity of the ω_{FR} = 332 Hz trace. Further analysis of the tape recorded data at smaller excitation frequency increments show a peak response at ω_{FR} = 331 Hz. The cascade plot for the excitation range in the vicinity of the blade one nodal diameter backward whirl mode is seen in fig. 5.29. Again, a relatively pure blade spectral response is seen with the one nodal diameter blade mode resonant peak occuring in the vicinity of 389 Hz.

The cascade plots for the Ω = 60 Hz backward whirl disk rigid body translation and one nodal diameter blade modes are shown in figures 5.30 and 5.31, respectively. The spectra contain evidence of undesired response at $\omega_{FN}-\Omega$ and ω_{FN}, but the target backward whirl response at $\omega_{FR} = \omega_{FN}+\Omega$ occurs at a much improved signal-to-noise ratio compared to the desired response obtained for the forward whirl excitation case. The cascade plot in fig. 5.30 indicates that the resonant frequency for the disk rigid body translation mode occurs in the vicinity of ω_{FR} = 279 Hz. Upon a more detailed inspection of the tape

data, an identical natural frequency is obtained. Figure 5.31 indicates that the blade one nodal diameter natural frequency appears in vicinity of ω_{FR} = 405 Hz, which is very close to the frequency of 406 Hz obtained upon a more detailed inspection of the data. The blade response transfer function for the Ω = 60 Hz backward whirl case is shown in fig. 5.32.

The cascade plots for the highest rotor speed tested, Ω = 150 Hz are shown in figures 5.33 and 5.34. Both plots show relatively pure backward whirl forced response with negligible amplitudes of response at ω_{FN}. In the range of the frequency scales used in the figures, the forward whirl frequency ω_{FN}-Ω response noise does not appear, but it is also of negligible amplitude. However in both figures there is evidence of a small amplitude response at harmonics of the rotor speed Ω. Figure 5.33, which corresponds to the excitation range for the disk rigid body translation dominated mode, indicates that the resonant frequency occurs in the vicinity of 365 Hz. A more detailed inspection of the tape recorded data indicates that the more precise location of the mode is at 364 Hz. The excitation range spanned by the response traces in fig. 5.34 includes the blade one nodal diameter mode, whose natural frequency is seen to occur near 461 Hz. A more detailed data reduction indicates that the mode actually occurs at 462 Hz. The blade response transfer function for the Ω = 150 Hz case is shown in fig. 5.35.

The blade response has been examined in the frequency domain for both forward and backward whirl excitation. In general it was evident that it was possible to excite a more pure backward whirl response compared to that obtained for forward whirl. The regions of excitation discussed in section 5.3 where outlined on the system frequency plots of figures 5.27 and 5.36. From these data and the other tests whose data were not detaied specifically, the experimentally determined system frequency plot of fig. 5.37 is obtained. The experimental natural frequencies

are overplotted on those predicted by the 6 DOF model described in Chapter 2. The correlation between the experimental and predicted results will be examined in the next section.

5.4) Correlation of Experimental Results with the Model Predictions

In this section the correlation between the system natural frequencies that were experimentally determined and those predicted by the analytical model of chapter 2 will be discussed. The agreement between the experimental and the predicted and experimental results is reasonable and shows the correct trends in dynamic behaviour, given the uncertainty in characterizing the system stiffness parameters required as input for the model.

The system natural frequencies determined by the 6 DOF model of eqn. (2.1.7) have been used as a prediction of the dynamic behaviour of the shaft-bladed disk system. The most refined stiffness fit, that is the fit that correlated best with the nonrotating modal data, was used as input to the system equations of motion (2.1.7). These stiffness data are tabulated in column (c) of Table A.2. The inertial properties of the rotor, which are listed in Appendix A, were also used. The resultant rotor dynamic behavior is shown in fig. 5.37. The comparison between the $\Omega = 0$ natural frequencies predicted by the model with the improved stiffness fit of fig. 5.37 and the experimentally measured frequencies are shown in Table 5.4.1.

Table 5.4.1 Comparison of Ω = 0 Predicted and Experimental Natural Frequencies

Mode	Predicted	Measured
Low Disk Translation Dominated	222.5 Hz	222 Hz
High Disk Pitch Dominated	311.3 Hz	325 Hz
Blade One Nodal Diameter	394.5 Hz	388 Hz

It can be seen that the high disk pitch mode is predicted to occur at a frequency lower than that measured. It can also be seen that the Ω = 0 blade one nodal diameter mode is predicted at a higher frequency than that measured. The disk translation mode is predicted accurately by the model however.

The correlation between the predicted and measured dynamic whirling behaviour of the MIT Aeroelastic rotor at speeds up to Ω = 150 Hz (9000 rpm) can be seen from fig. 5.37. The measured blade one nodal diameter natural frequencies correlate well with the predicted modes at low speeds, in spite of the offset between the two at zero rotor speed. At rotor speeds above approximately 90 Hz, the experimental blade modes correlated less well and were higher than those predicted by the model. This is an indication that the blade centrifugal stiffening effects were underestimated in the model. The measure of this blade centrifugal stiffening, the Southwell coeficient ℓ which is listed in Appendix A as 1.93, is probably too low. Another feature of the blade modes that is apparent in fig. 5.37 is the slight split in the blade forward and backward whirl natural frequencies. This would not be predicted in a conventional rigid shaft model.

The difficulty in obtaining a good signal-to-noise ratio for the forward whirl disk rigid body response led to difficulties in determining the forward whirl disk rigid body pitch modes above a rotor speed of 30 Hz. Therefore only the Ω = 0, 5, 30 Hz forward whirl disk rigid body pitch modes are indicated on fig. 5.37. The backward whirl disk rigid body

pitching modes were excited with a much greater signal-to-noise ratio. The correlation between the experimental natural frequencies for the backward whirl disk rigid body pitch modes with the predicted frequencies indicates that the measured modes occur at higher frequencies than those predicted by the model. This is partially due to the $\Omega = 0$ predictions being lower than the measured frequency, as seen in Table 5.4.1. However the degree of centrifugal stiffening of the pitch mode seems to also be underestimated by the model. The experimental data also indicates that the degree of interaction between the backward whirl disk rigid body pitching motion and the blade forward whirl one nodal diameter motion is underestimated by the model. No such interaction, of course, would be predicted by a conventional rigid shaft model.

The agreement between the experiment and the model for the disk rigid body translation mode is very good for low speeds. However at higher rotor speeds, the split of the disk translation modes is underestimated by the model. This is because the $\Omega = 0$ disk pitch and translation modes are more closely spaced in the model prediction than in the experimental case. Therefore the interaction between the disk translation and pitch modes is overestimated in the predictions of the model. The result of this is to predict the backward whirl mode at too low a frequency and the forward mode at too high a frequency. The experimental forward whirl disk translation data indicates that the model predicts a critical speed (the intersection of the forward whirl curve with the Ω axis) that is too high, specifically around 235 Hz. Extrapolation of the experimental data indicates an actual critical speed of approximately 215 Hz.

Therefore the results of the experimental forced whirl testing correlate reasonably well with the model given the uncertainty of the input parameters to the prediction. The physical coupling phenomena predicted in the model are clearly

exhibited in the experimental results.

6. Conclusions

A series of rotating whirl tests have been performed in the vacuum of the MIT Blowdown Compressor Facility on the MIT Aeroelastic Rotor, which is structurally typical of modern high bypass ratio cantileverd turbofan stages. The test section of the Facility was modified to install an electromagnetic shaker whirl excitation system. This arrangement allowed for dynamic testing of the rotor at at arbitrary rotor speed, direction of whirl excitation, and excitation frequency. Using the 23 blade piezoelectric displacement transducers as the primary response monitoring instrumentation, the rotor was excited at speed with an excitation pattern of constant whirl direction and slowly sweeping frequency. The frequencies at which the driven response attained a maximum amplitude were found as the rotor natural frequencies.

In order to predict the natural frequencies of the MIT AE Rotor as installed in the Facility, the analytical model of Mokadam [5] was modified to include the effects of the system center of mass not coinciding with the disk centroid for a massive shaft. The structural properties of the rotor were then required in order to use the model to predict the system dynamic behavor. The inertial properties of the system were calculated by careful measurements and the use of holographic blade mode shape determination. Attempts to measure the shaft and support structure stiffnesses by static loading and displacement measurement were unsuccessful. The results of the static tests showed large scatter and nonlinearity, probably due to the use of angular contact ball bearings in the rotating assembly. Therefore the shaft and support structure stiffnesses were determined by a series of nonrotating dynamic testing of the low shaft-disk dominated modes. The resulting dynamic data and inertial parameters were fit to a simple 2 DOF model of a rigid

bladeless disk in order to calculate the effective stiffnesses of the system. The resulting stiffnesses were then further fit to the full 6 DOF whirl analytical model in order to obtain the best possible fit to the nonrotating dynamic measurements.

With the benefit the predicted natural frequency information, the rotating whirl tests were carried out. Slow sweeps of excitation frequency were performed at constant rotor speed and whirl direction and the resulting blade displacement data were analyzed in the frequency domain and the following results were observed:

1. The whirl excitation system was successful in forcing the target whirl response directions. However, the backward whirl motion was excited at a much greater signal-to-noise ratio than the forward whirl motion. The response of the system also included response at harmonics of the rotor speed Ω, at the inertial forcing frequency ω_{FN}, and at untargeted whirl direction.
2. The dynamic behavor of the rotor followed the general predictions of the analytical model. In the rotor frame of reference the disk rigid body translation dominated mode shows the split into forward and backward whirl legs, the forward whirl curve apporoaching a zero frequency static divergence at the rotor critical speed. The rigid body pitch dominated modes also showed some splitting with increasing rotor speed due to the small component of translation in their eigenvectors. The blade one nodal diameter modes exhibited centrifugal stiffening but with a slightly stronger dependence on rotor speed than predicted. this indicates that the Southwell coefficient may have been underestimated.
3. The degree of interaction observed between the bladed disk modes was seen to be stronger in the experimental results than predicted by the model. This is probably due

to the uncertainty associated with the determination of the shaft and support structure stiffness properties.

The nonrotating modal surveys performed in order to determine the stiffness properties revealed that the nonrotating support structure for the rotor did exhibit stiffness asymmtries. The rotating assembly was found to be symmetric in its dynamic behavior, as would be expected of a precision axisymmetric structure. The asymmetry in the nonrotating assembly could be in part responsible for the rotor whirl response at the inertial forcing frequency ω_{FN} and at the undesired whirl direction frequency.

Finally the nondimensionalization of the equations of motion yielded the relevant parameters for evaluating the propensity for, and magnitude of interactions between the bladed-disk and the shaft-disk dynamics. Consideration of a rotor with only translation or pitch disk degrees of freedom yields the result that the effect of the Southwell coefficient being greater than one (as it is in gas turbine blading) is to decrease the propensity for interaction of the shaft-disk modes with the bladed-disk modes with increasing rotor speed.

References

1. Coleman, R.P. and Feingold, A.M., "Theory of Self-Excited Mechanical Oscillations of Helicopter Rotors with Hinged Blades", NACA TR 1351, 1958.

2. Crandall, S.H. and Dugundji, J., "Resonant Whirling of Aircraft Propellor-Engine Systems", J. Appl. Mech., Vol. 48, December 1981, pp. 929-935.

3. Palladino, J.A. and Rossettos, J.N., "Finite Element Analysis of the Dynamics of Flexible Disk Rotor Systems", ASME Paper No. 82-GT-240, 1982.

4. Loewy, R.G. and Khader, N., "Structural Dynamics of Rotating Bladed-Disk Assemblies Coupled with Flexible Shaft Motions", AIAA J., Vol. 22, No. 9, September 1984, pp. 1319-1327.

5. Mokadam, D.R., "Structural Response of a Rotating Bladed Disk to Whirl", S.M. thesis, Department of Aeronautics and Astronautics, MIT, September 1983.

6. Kerrebrock, J.L., et.al., "The MIT Blowdown Compressor Facility", J. Engineering for Power, Vol. 96, No. 4, pp. 394-405, October 1974.

7. Den Hartog, J.P., Mechanical Vibrations, 4^{th} ed., McGraw-Hill, New York, 1956.

8. Crawley, E.F., "In-Plane Inertial Coupling in Tuned and Severely Mistuned Bladed Disks", ASME Paper No. 82-GT-288, 1982.

9. Crawley, E.F. and Mokadam, D.R., "Stagger Angle Dependence of Inertial and Elastic Coupling in Bladed Disks", J. Vibration, Acoustics, Stress, and Reliability in Design, Trans.ASME, Vol. 106, pp. 181-188, April 1984.

10. Crawley, E.F., "Aerodynamic Damping Measurements in a Transonic Compressor", ASME Paper No. 82-GT-287, 1982.

11. Smith, B.T., et.al., Matrix Eigensystem Routines - EISPACK Guide, Lecture Notes in Computer Science, Vol. 6, Springer-Verlag, New York, 1976.

12. Dugundji, J. and Wendell, J.H., "Some Analysis Methods for Rotating Systems with Periodic Coefficients", AIAA J., Vol. 21, No. 6, pp. 890-897, June 1983.

Appendix A: Structural Properties of the MIT Aeroelastic Rotor

i) Dimensional Parameters

The inertial properties of the entire shaft-disk-blading assembly with respect to a coordinate system shown in fig. 2.1 and a system center of mass offset from the disk centroid as shown in fig. 2.2b are:

M = total mass of rotor assembly = 25.4 kg

S = axial mass imbalance = -0.741 kg•m

I_p = total rotor moment of inertia for pitching about a disk diameter = 0.297 kg•m^2

The holographically measured blade first bending mode shape [5] along the blade midchord line $\gamma(r)$, was determined as a fourth order polynomial fit:

$$\gamma(r) = c_0 + c_1 r + c_2 r^2 + c_3 r^3 + c_4 r^4$$

A careful process of laying out a grid on the blade surface and measuring the vloume of each resulting grid cell yielded a fourth order fit to the blade spanwise mass distribution along the midchord line:

$$\frac{\partial m}{\partial r} = d_0 + d_1 r + d_2 r^2 + d_3 r^3 + d_4 r^4 \qquad \left[\frac{g}{cm}\right]$$

The coefficients c_i and d_i of the fits are tabulated in Table A.1.

Table A.1 Polynomial Fit Coefficients†

Mode Shape Coefficients		Mass Distribution Coefficient	
c_0	$-6.8104 * 10^{-1}$	d_0	$4.1730 * 10^{1}$ g/cm
c_1	$1.0519 * 10^{-1}$ cm^{-1}	d_1	-3.1294 g/cm^2
c_2	$-5.5161 * 10^{-3}$ cm^{-2}	d_2	$1.1123 * 10^{-1}$ g/cm^3
c_3	$9.4717 * 10^{-5}$ cm^{-3}	d_3	$-2.0470 * 10^{-3}$ g/cm^4
c_4	$1.3225 * 10^{-6}$ cm^{-4}	d_4	$1.1887 * 10^{-5}$ g/cm^5

† for r in [cm].

From their integral definitions given in Chapter 2 and the fits shown above, the blade inertial properties are calculated:

m_0 = blade modal mass = $1.43 * 10^{-3}$ kg•m²

m_1 = blade consistent mass coupling disk pitch = $2.41 * 10^{-3}$ kg•m²

m_2 = blade consistent mass coupling disk translation = $1.01 * 10^{-2}$ kg•m

m_Ω = blade mass foreshortening = $3.70 * 10^{-3}$ kg•m²

The stiffness parameters of the system were fit with various degrees of sophistication. These fits are tabulated in Table A.2. Column (a) of the table corresponds to the shaft and support structure stiffness fit to the simple 2 DOF model of eq. (4.3.1) using the uncompensated nonrotating modal data. The resulting behavior of the system natural frequencies at speed for this "baseline" fit areshown in the rotor frame in fig. 4.3a and in the nonrotating frame in fig. 4.3b.

The stiffness data in column (b) of Table A.2 corresponds to an improved fit using some information resulting from the $\Omega = 0$ frequency predictions of the 6 DOF model. The shifting in the

predicted disk frequencies that occurs when the blade effects are included with the full model is precompensated for by using the frequencies of 222 Hz and 335 Hz as input to the 2 DOF model instead of the experimentally observed values of 222 Hz and 325 Hz. The resulting translation / pitch stiffness coupling term calculated by the 2 DOF fit is decreased by 35% and the 2 DOF characteristic equation is again solved to find the corresponding transaltion and pitch stiffnesses. the blade stiffness remains uncompensated in this fit. The resulting system natural frequencies predicted by the model using this fit is shown in the rotor frame in fig. 4.4a and in the nonrotating frame in fig. 4.4b.

A further improvement in the fit between the experimentally measured frequencies and those predicted by the model is presented in column (c) of Table A.2. This fit was obtained by: precompensating the measured nonrotating natural frequencies as in the column (b) case, decreasing the resulting stiffness coupling by 30%, calculating the corresponding translation and pitch stiffnesses, and decreasing the blade modal stiffness by 19%. The resulting dynamic behavior of the system is shown in the rotor frame in fig. 4.5a and in the nonrotating frame in fig. 4.5b.

Table A.2 Stiffness Fits for the MIT AE Rotor

Stiffness Parameter	a	b	c
K_{xR}, K_{yR} [10^7 N/m]	8.10	5.47	5.68
$K_{\xi R}$, $K_{\eta R}$ [10^6 N•m/rad]	1.05	1.32	1.40
$K_{x\eta R}$, $-K_{y\xi R}$ [10^6 N/rad]	5.29	3.44	3.70
K_B [10^3 N•m]	7.90	7.90	6.43

ii) Nondimensional Parameters

The nondimensional inertial parameters for the MIT AE Rotor as defined in section 2.2 are:

$$\mu_{TP} = 0.073 \qquad \mu_{TB} = 0.021$$
$$\rho = 0.0048 \qquad \mu_{PB} = 0.054$$

The centrifugal stiffening of the blade, or Southwell coefficient is:

$$\ell = 1.93$$

The nondimensional stiffness parameters for the three stiffness fit cases are listed in Table A.3:

Table A.3 Nondimensional Stiffness Parameters

Stiffness Parameter	a	b	c
ω_x/ω_B, ω_y/ω_B	0.759	0.624	0.636
ω_ξ/ω_B, ω_η/ω_B	0.798	0.897	0.924
$\hat{k}$	0.331	0.164	0.172

Appendix B: Experimental Natural Frequencies

Table B.1 lists the natural frequencies of the disk translation dominated mode, disk pitch dominated mode, and the blade one nodal diameter (1ND) mode for both forward and backward whirl as a function of rotor speed.

Table B.1 Experimental Natural Frequencies

Rotor Speed [Hz]	Translation Mode [Hz]		Pitch Mode [Hz]		Blade 1ND [Hz]	
	FW	BW	FW	BW	FW	BW
0	222		325		388	
5	217	228	320	331	390	389
30	188	253	295	349	378	393
60	146	279	-	373	386	406
91.3	114	313	-	384	399	424
120	84	339	-	410	442	445
150	60	364	-	424	450	462

FW = forward whirl mode, BW = backward whirl mode

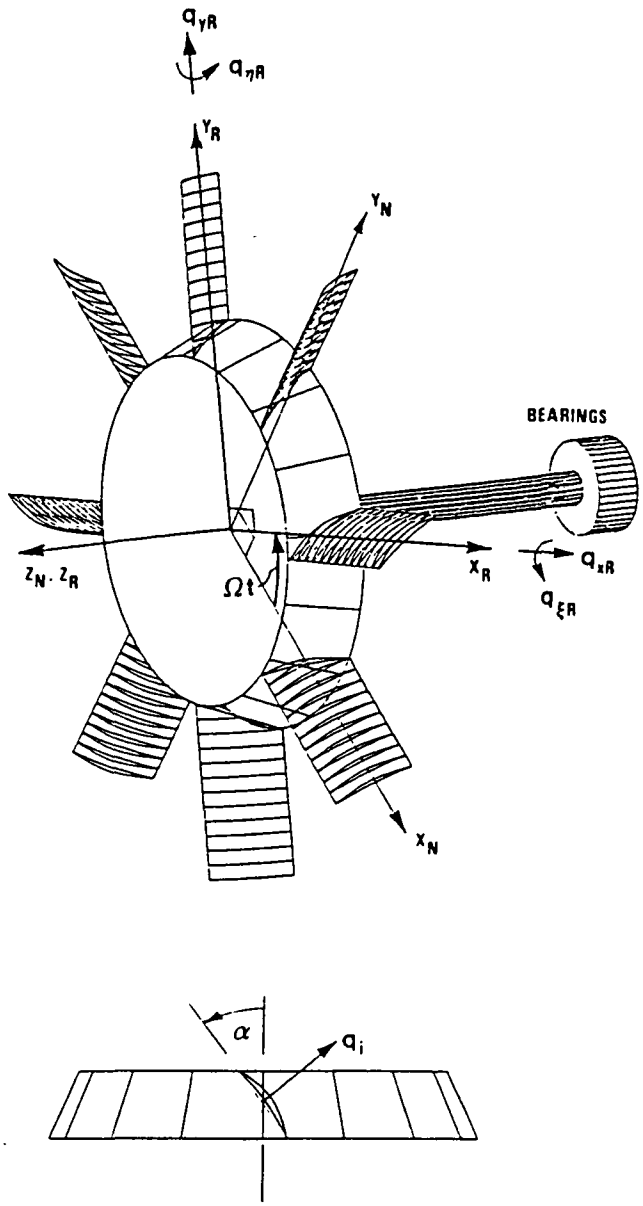

Fig. 2.1 Coordinate system for the whirl equations of motion for an N bladed shroudless fan cantilevered on a flexibe shaft.

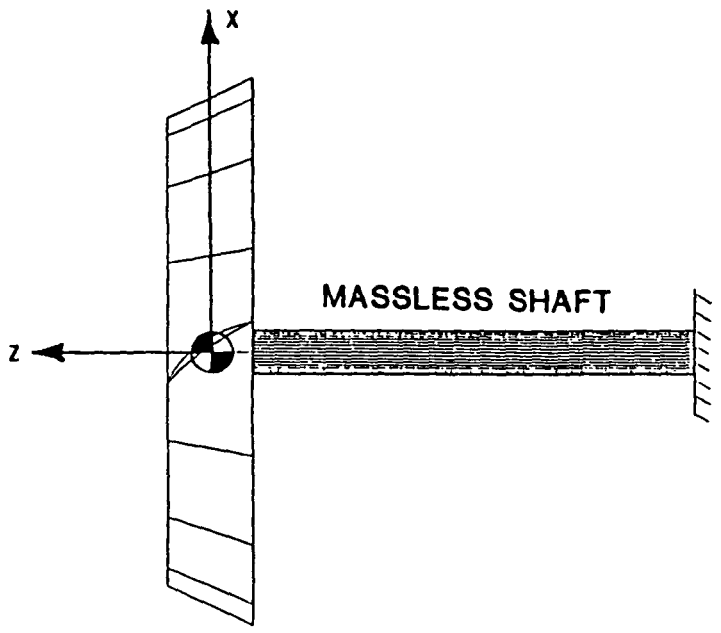

Fig. 2.2a System center of mass location for eq. (2.1.5)

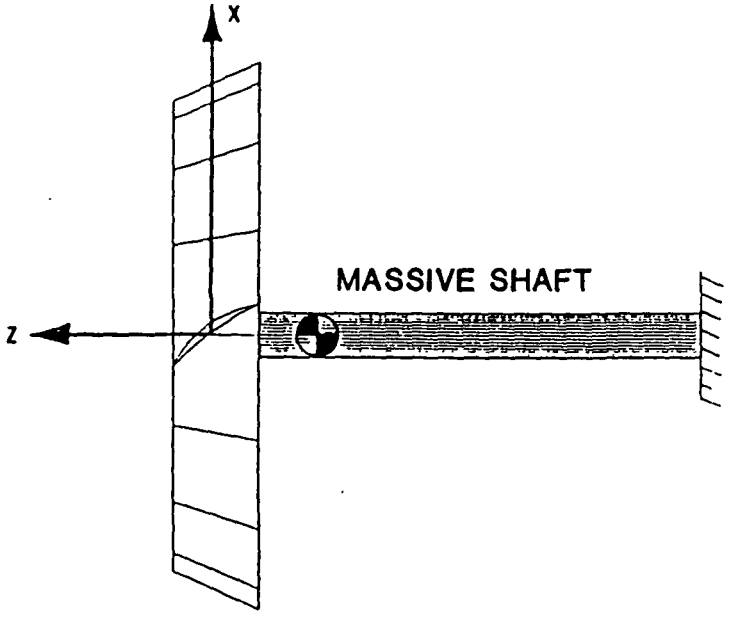

Fig. 2.2b System center of mass location for eq. (2.1.7)

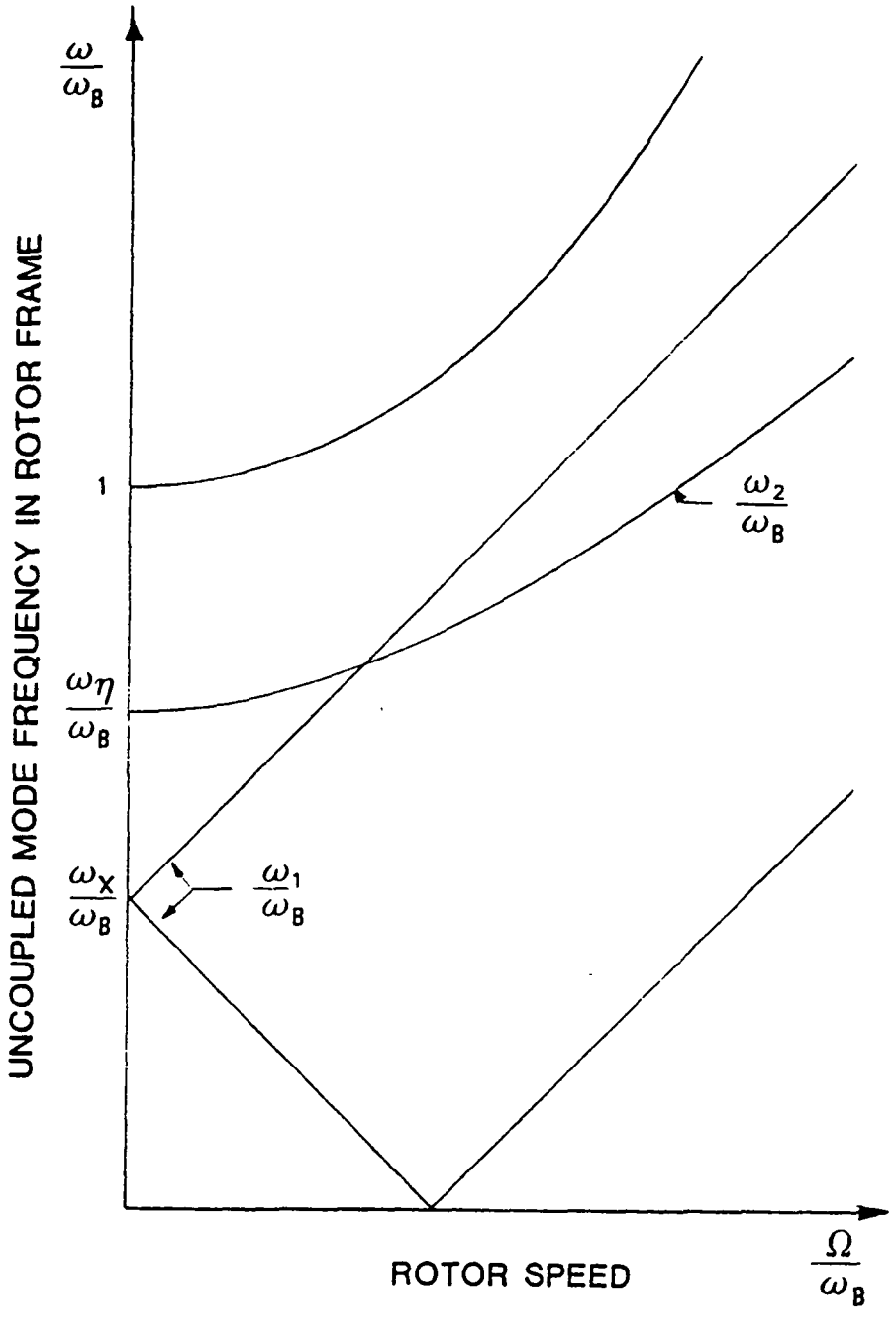

Fig. 2.3 Dynamic behavior of the uncoupled disk translation mode (ω_1), disk pitch mode (ω_2), and blade mode as a function of rotor speed.

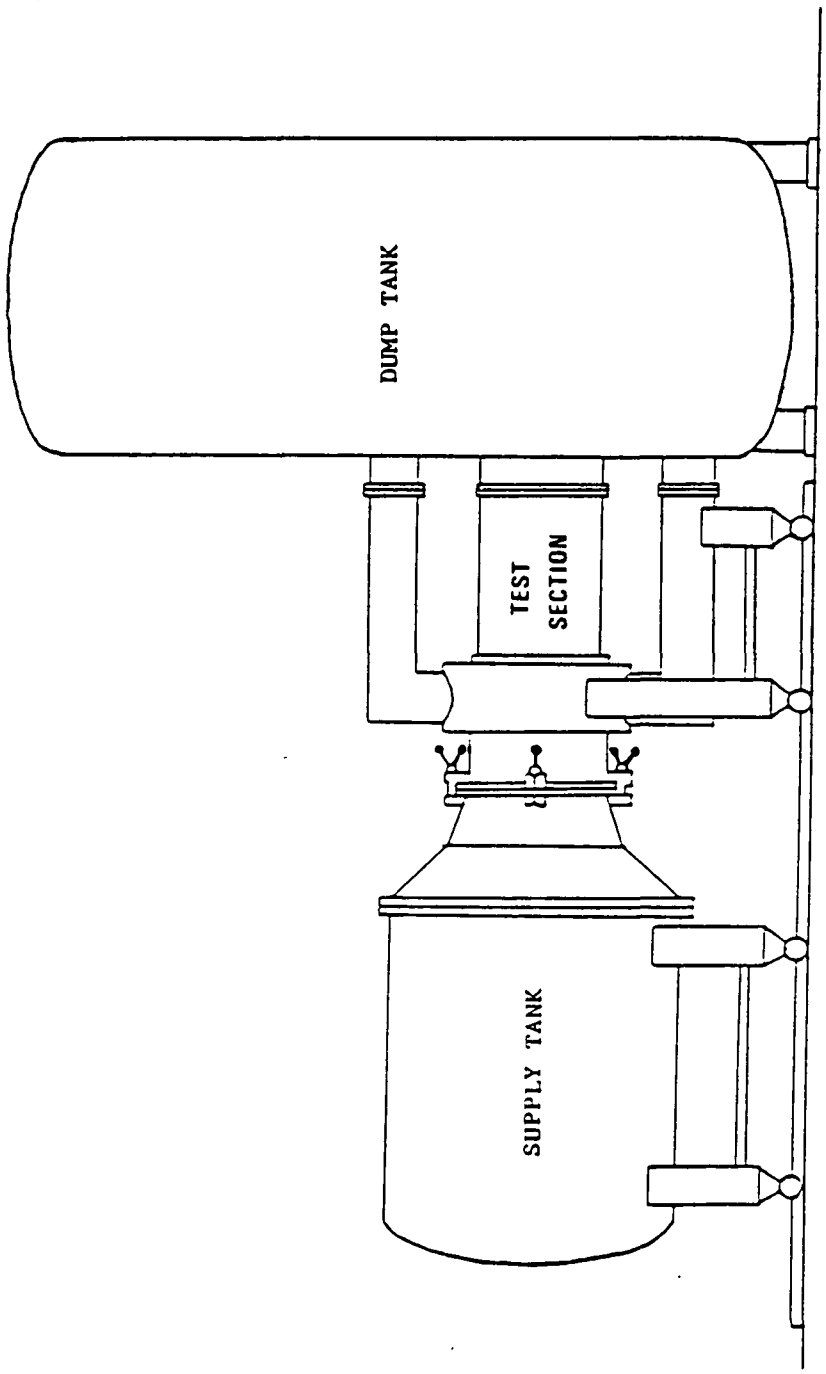

Fig. 3.1 The MIT Blowdown Compressor Facility

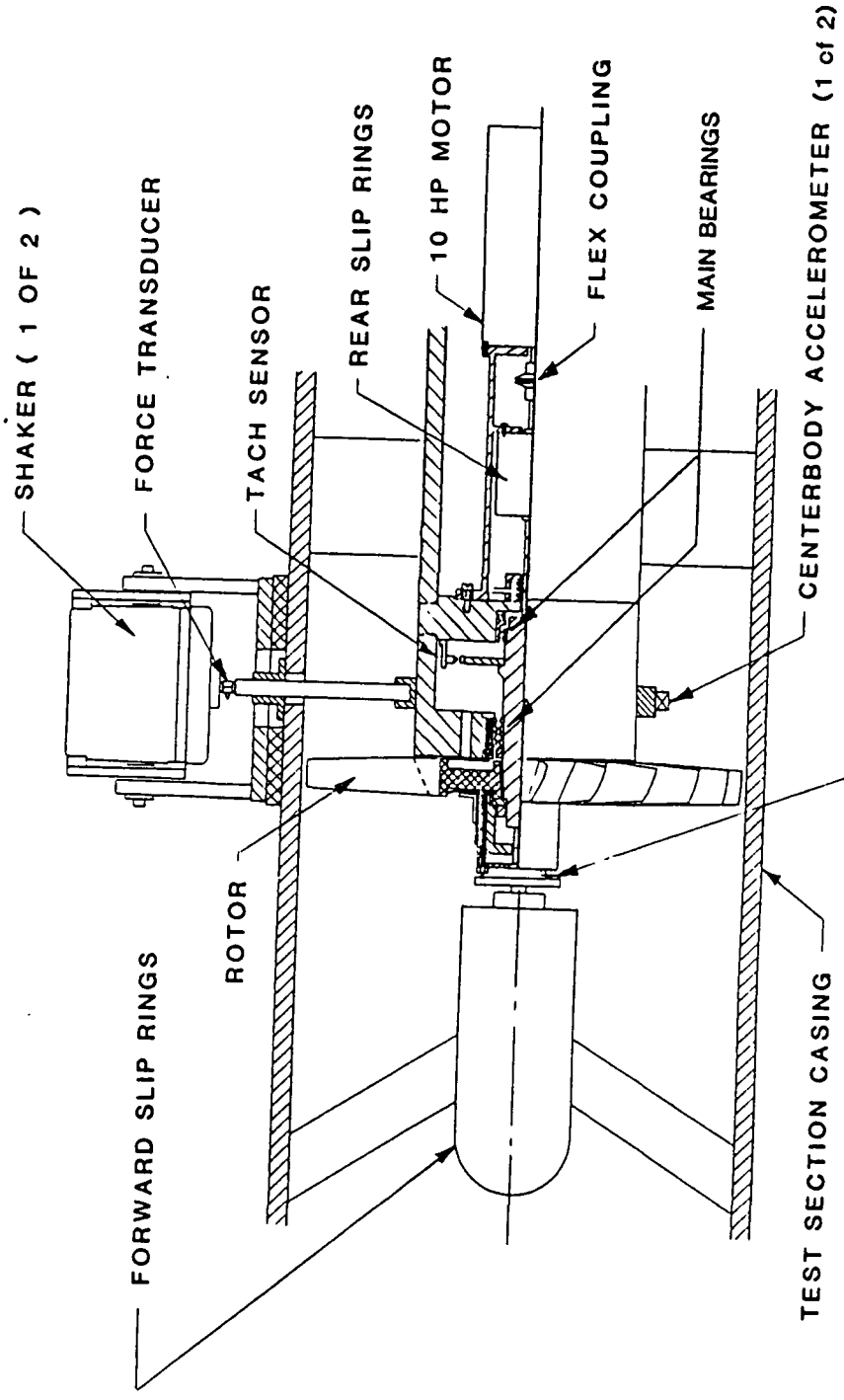

Fig. 3.2 Cutaway view of the the test section modified for whirl testing.

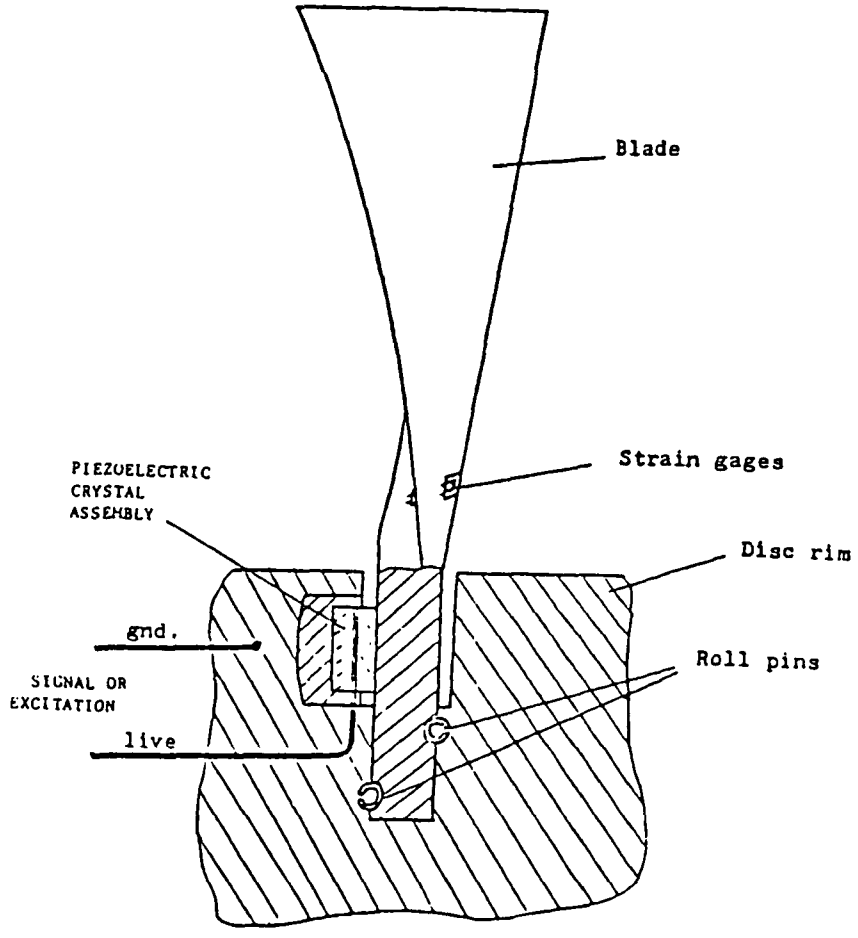

Fig. 3.3 Blade root attachment detail showing piezoelectric displacement transducer.

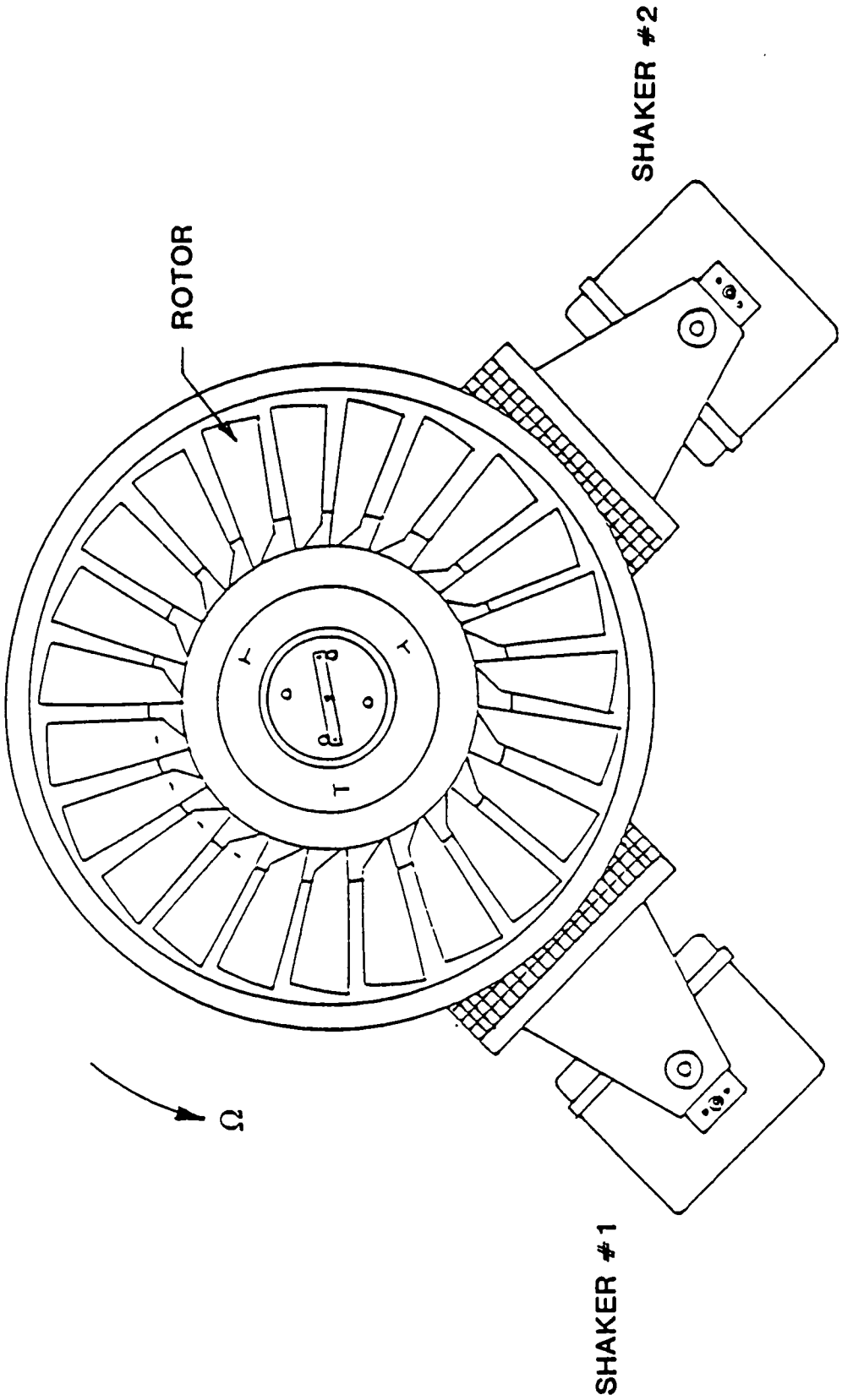

Fig. 3.4a Front view of the MIT AE Rotor installed in the test section with the whirl excitation system.

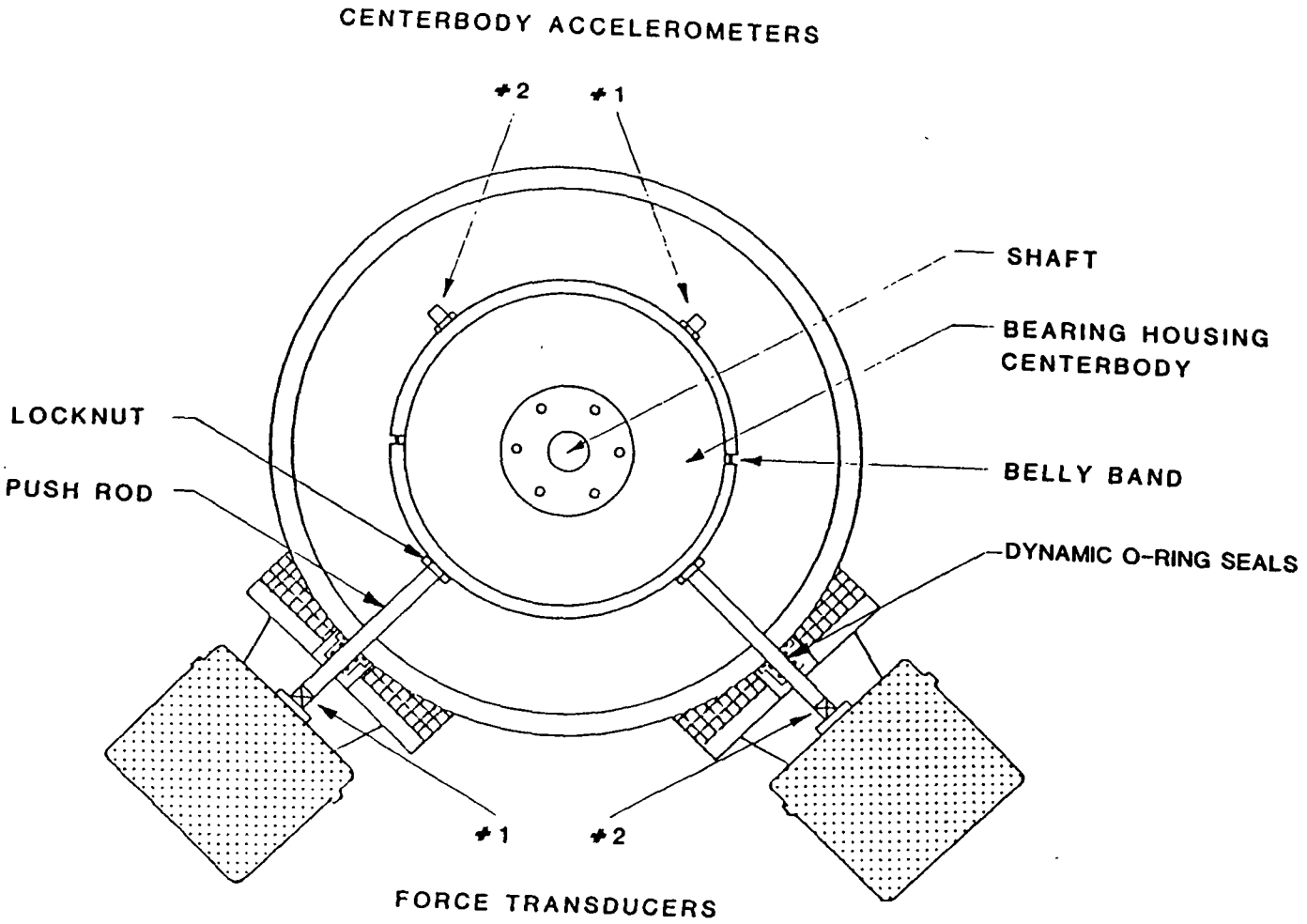

Fig. 3.4b View looking downstream of the whirl excitation system with the rotor removed.

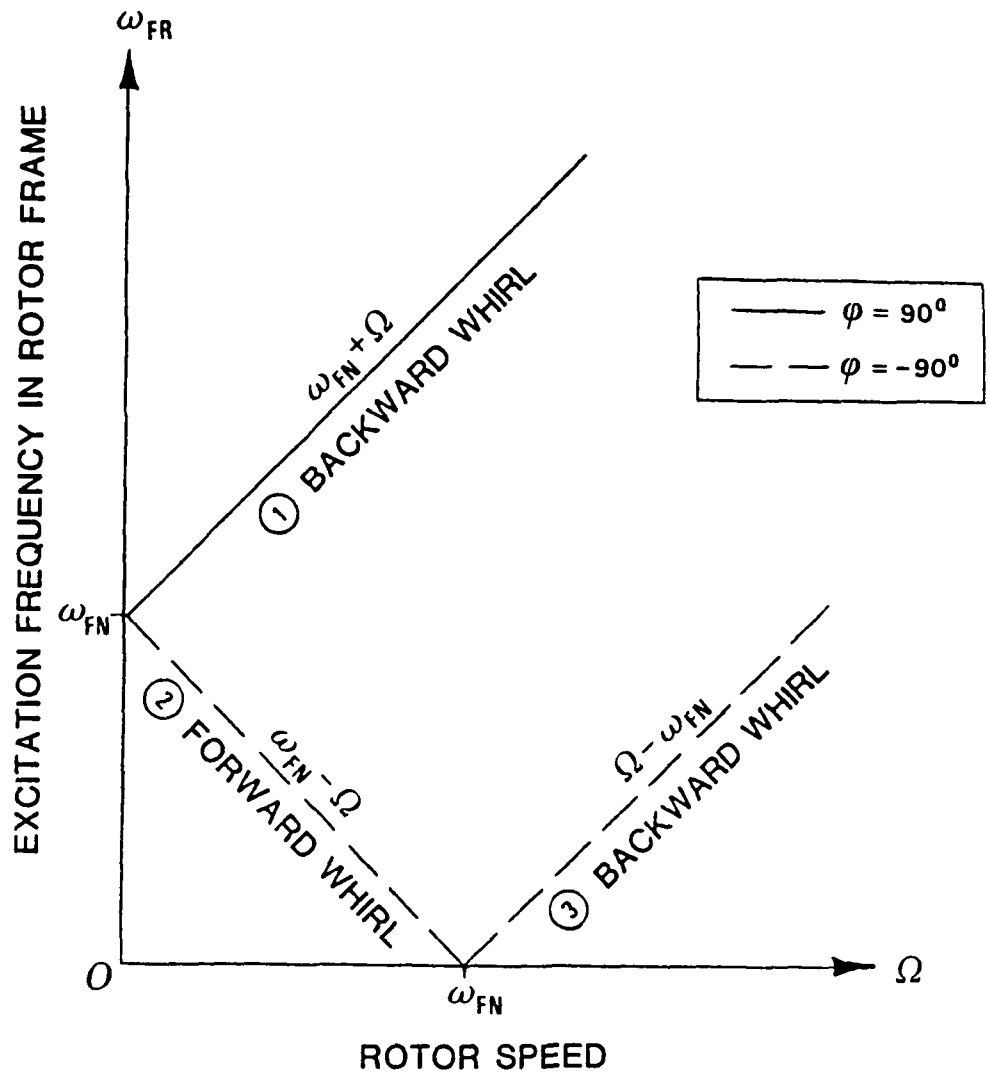

$$F_{N1} = F \sin \omega_{FN} t$$

$$F_{N2} = F \sin[\omega_{FN} t + \varphi]$$

Fig. 3.5 Summary plot of the whirl excitation transformation from the inertial to the rotor frame.

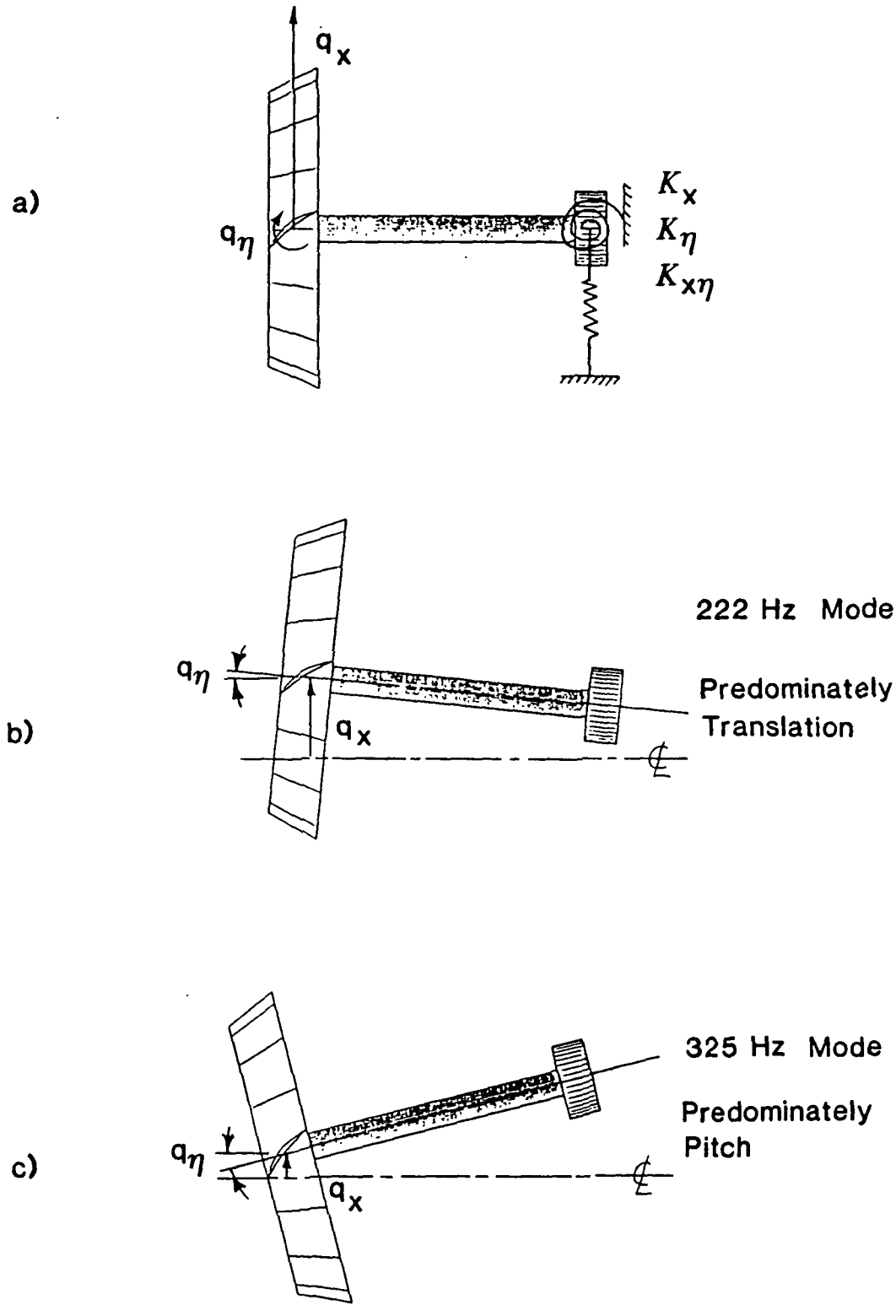

Fig. 4.1 Nonrotating shaft-disk modes of the of the MIT AE Rotor.

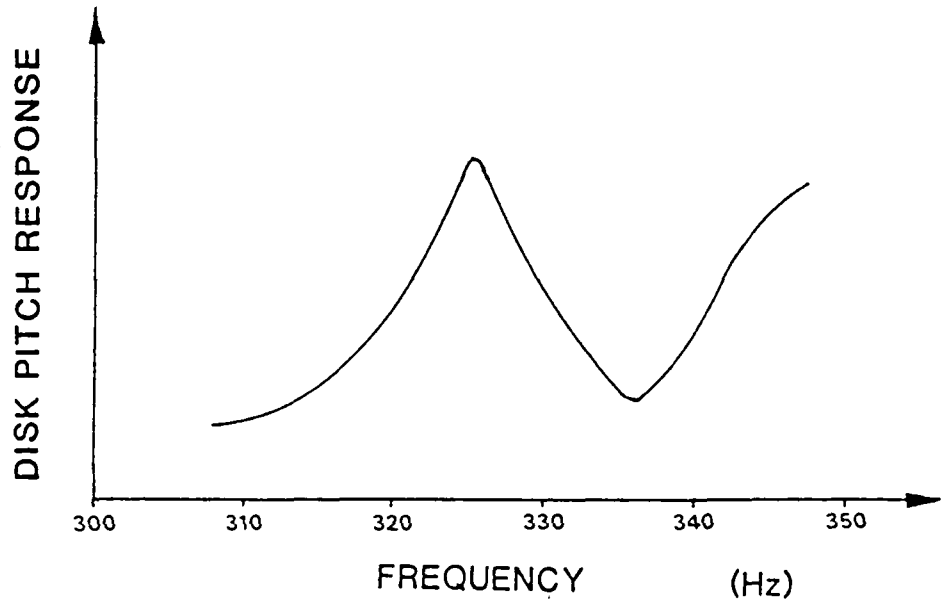

a) forcing direction and rotor position do not coincide with the system principal axes.

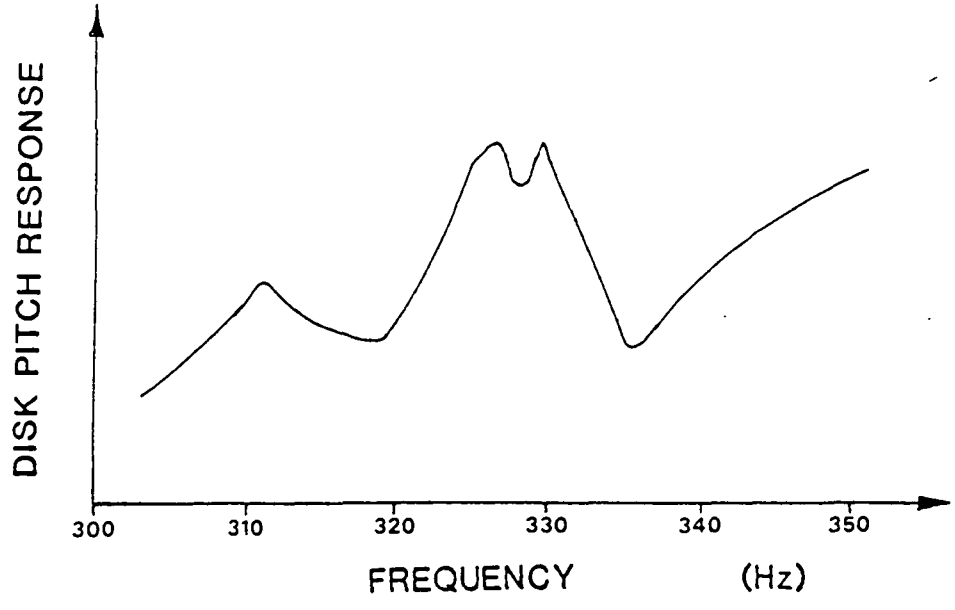

b) forcing direction and rotor position do coincide with system principal axes.

Fig. 4.2 Disk response amplitude as a function of forcing frequency in the neighborhood of the disk pitch mode.

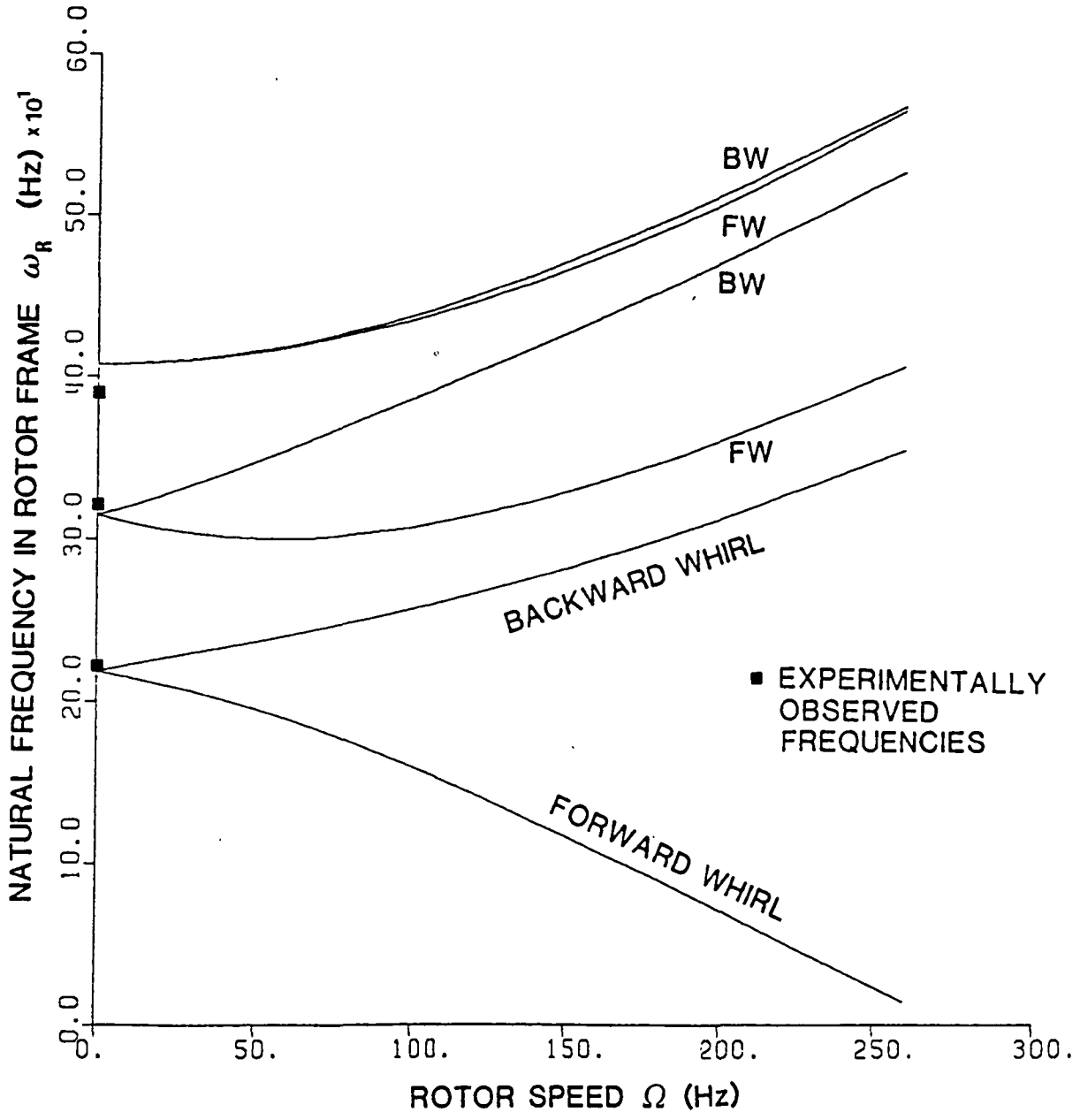

Fig. 4.3a System natural frequencies in the rotor frame predicted using stiffness parameters in Table A.2(a).

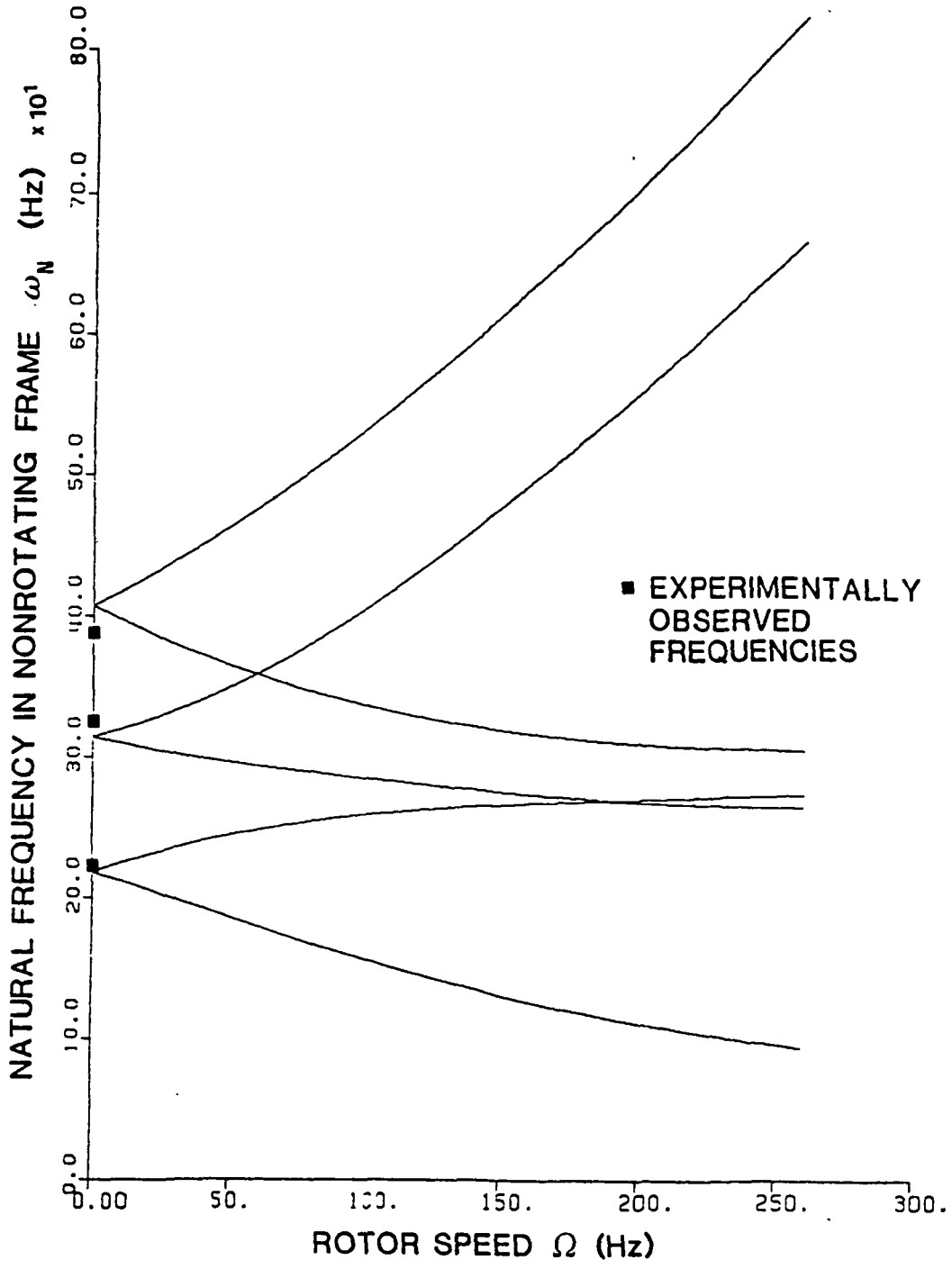

Fig. 4.3b System natural frequencies in the nonrotating frame predicted using stiffness parameters in Table A.2(a).

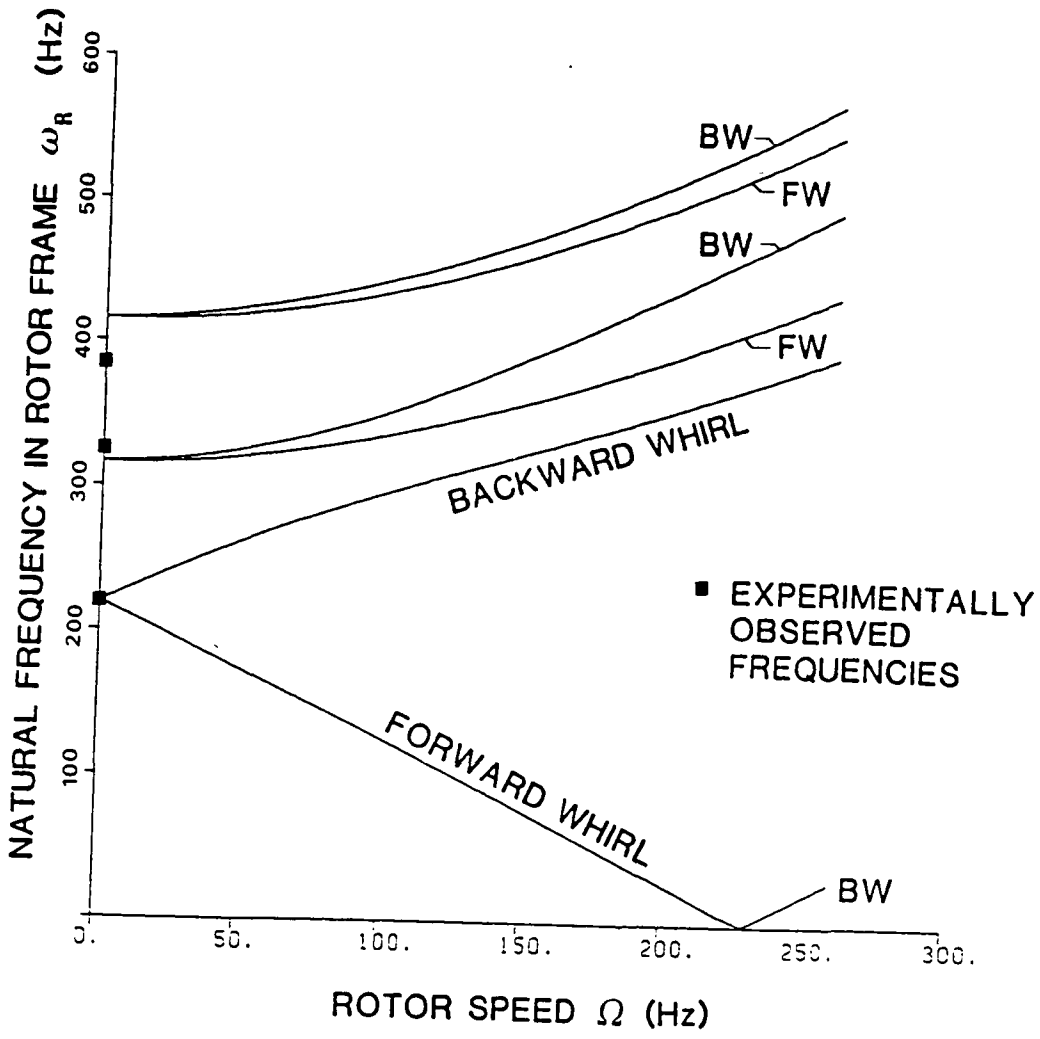

Fig. 4.4a System natural frequencies in the rotor frame predicted using stiffness parameters in Table A.2(b).

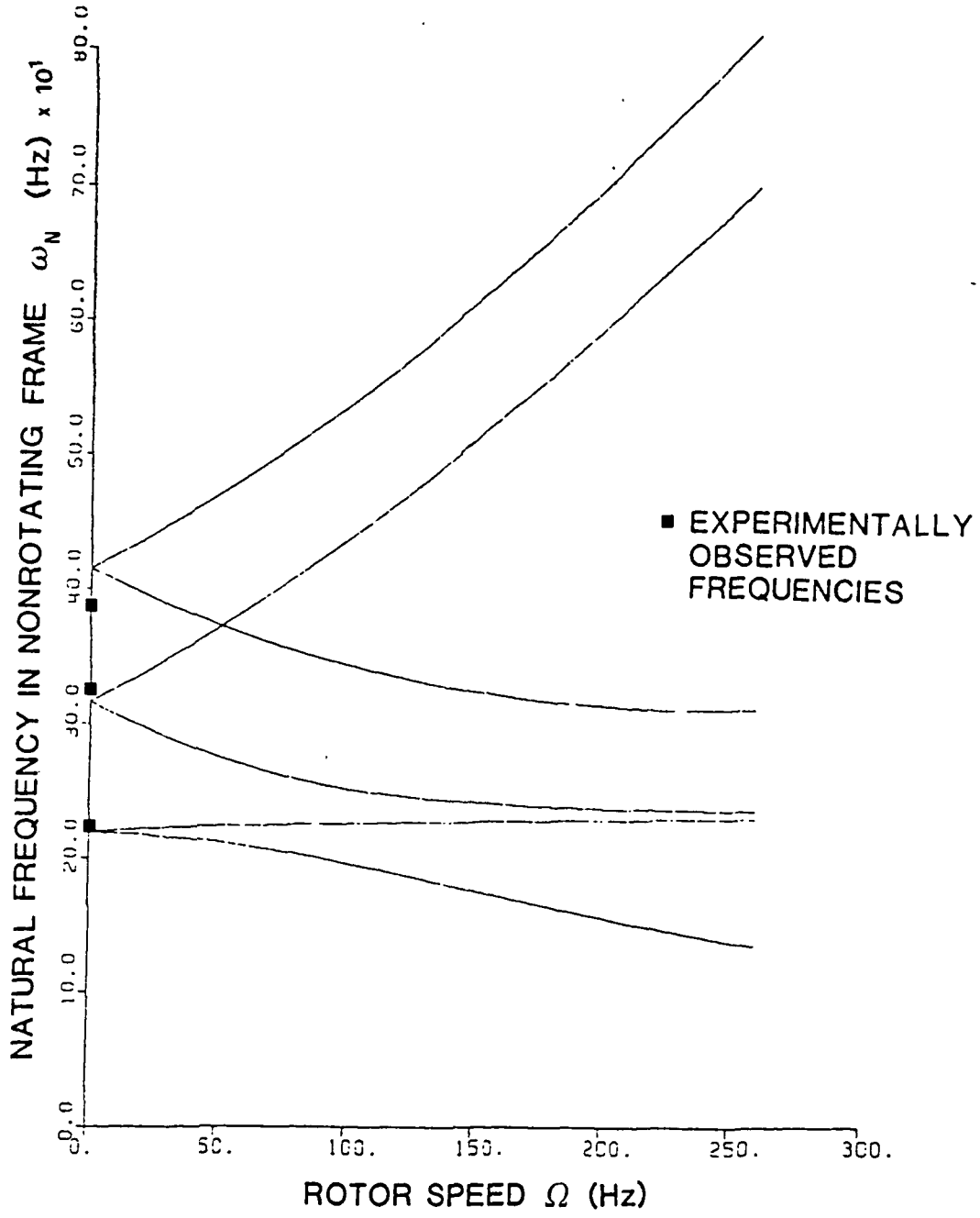

Fig. 4.4b System natural frequencies in the nonrotating frame predicted using stiffness parameters in Table A.2(b).

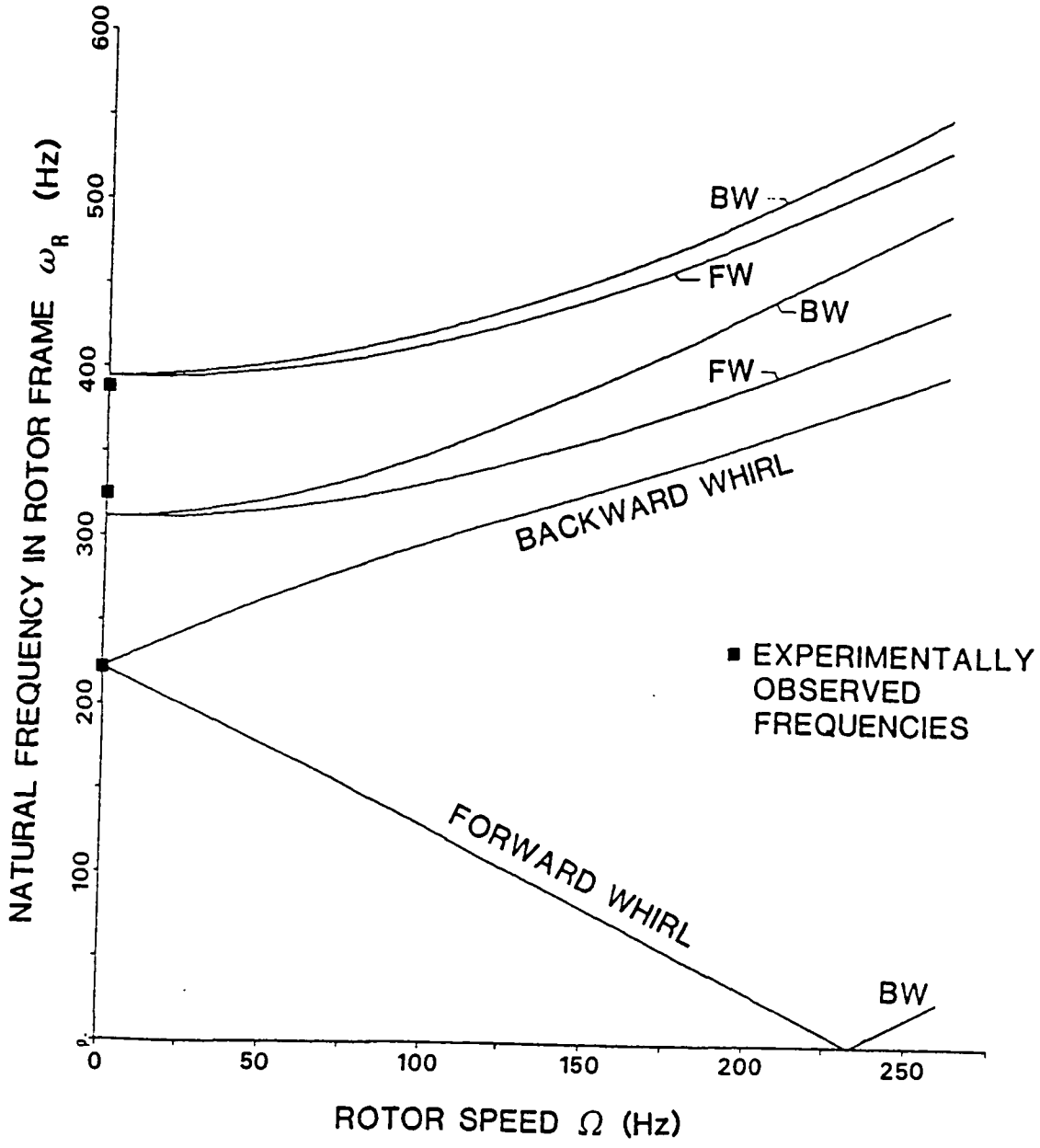

Fig. 4.5a System natural frequencies in the rotor frame predicted using stiffness parameters in Table A.2(c).

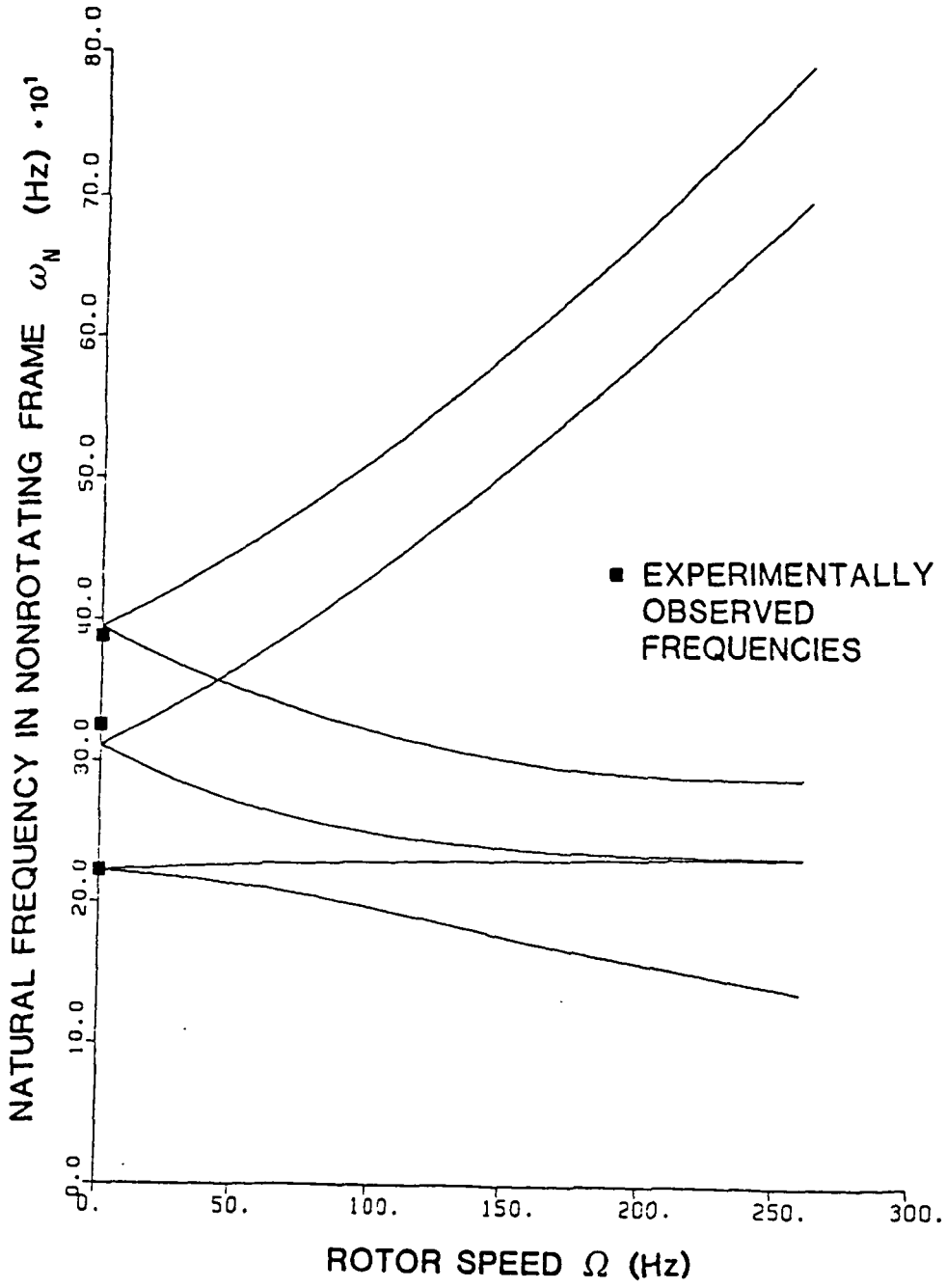

Fig. 4.5b System natural frequencies in the nonrotating frame predicted using stiffness parameters in Table A.2(c).

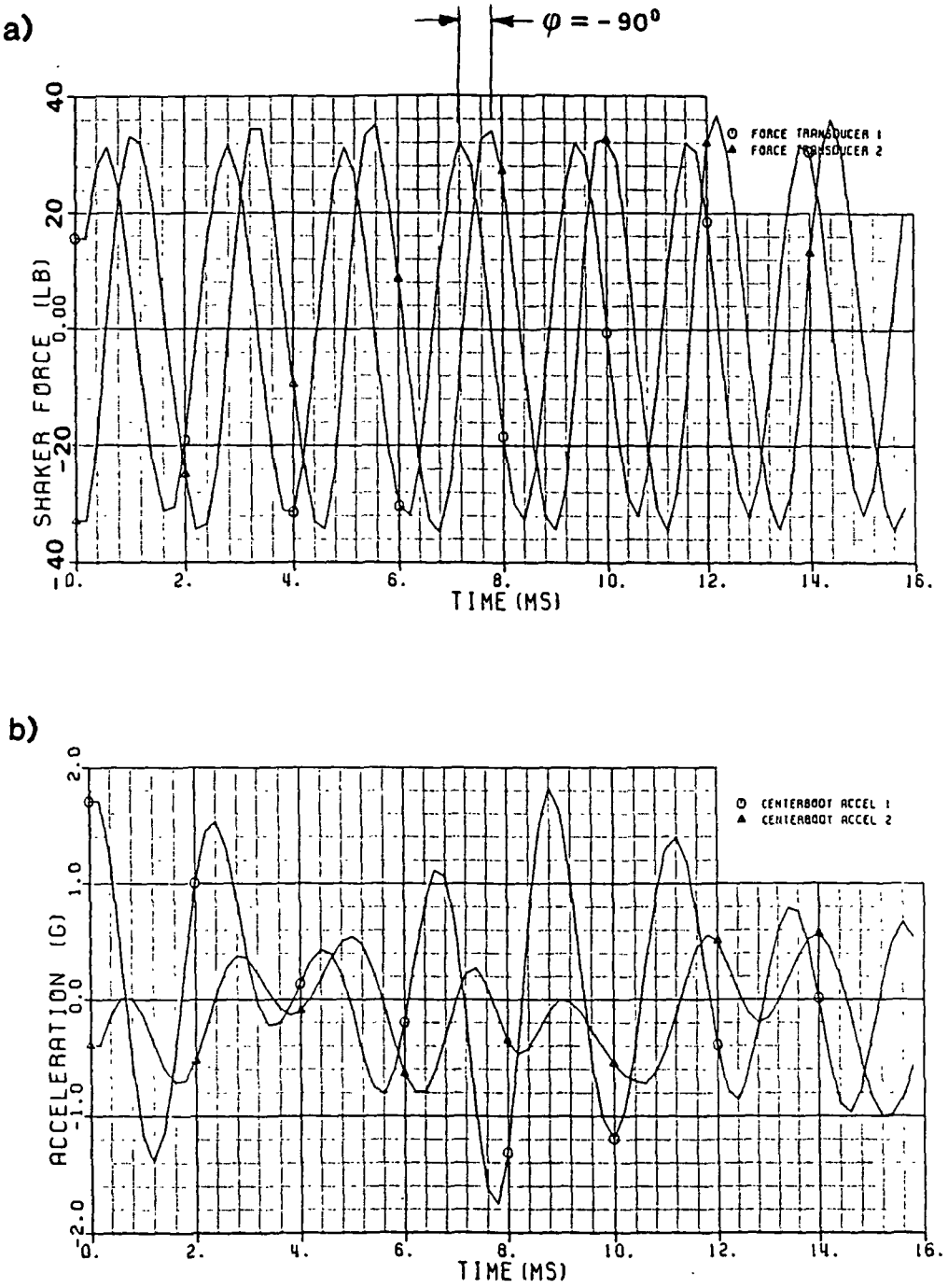

Fig. 5.1 Time history of the shaker force transducer signal (a) and bearing housing acceleration response (b) for the case of: forward whirl excitation, ω_{FN} = 449 Hz, Ω = 120 Hz.

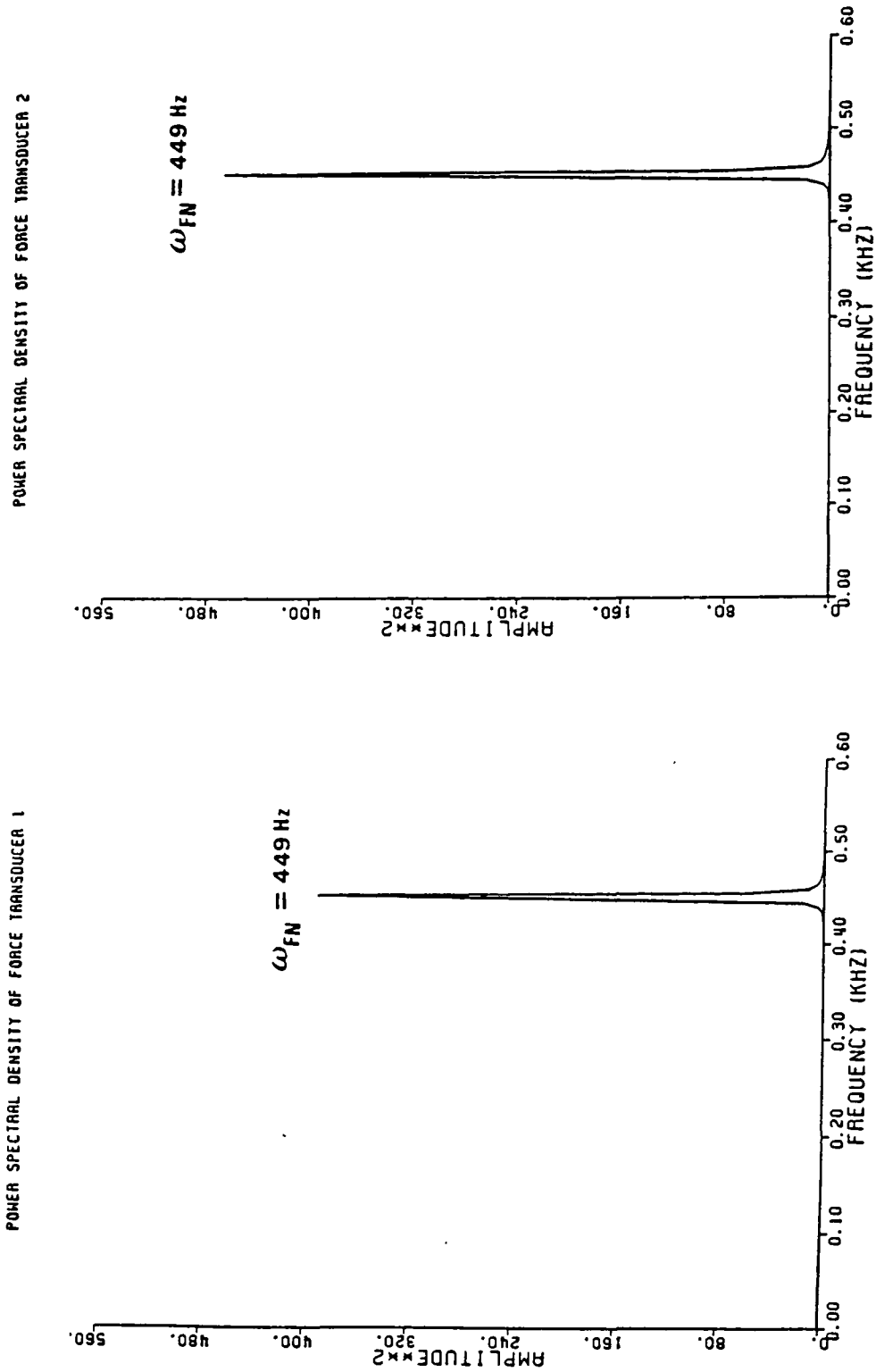

Fig. 5.2 Power spectral densities of the force transducer signals of fig. 5.1.

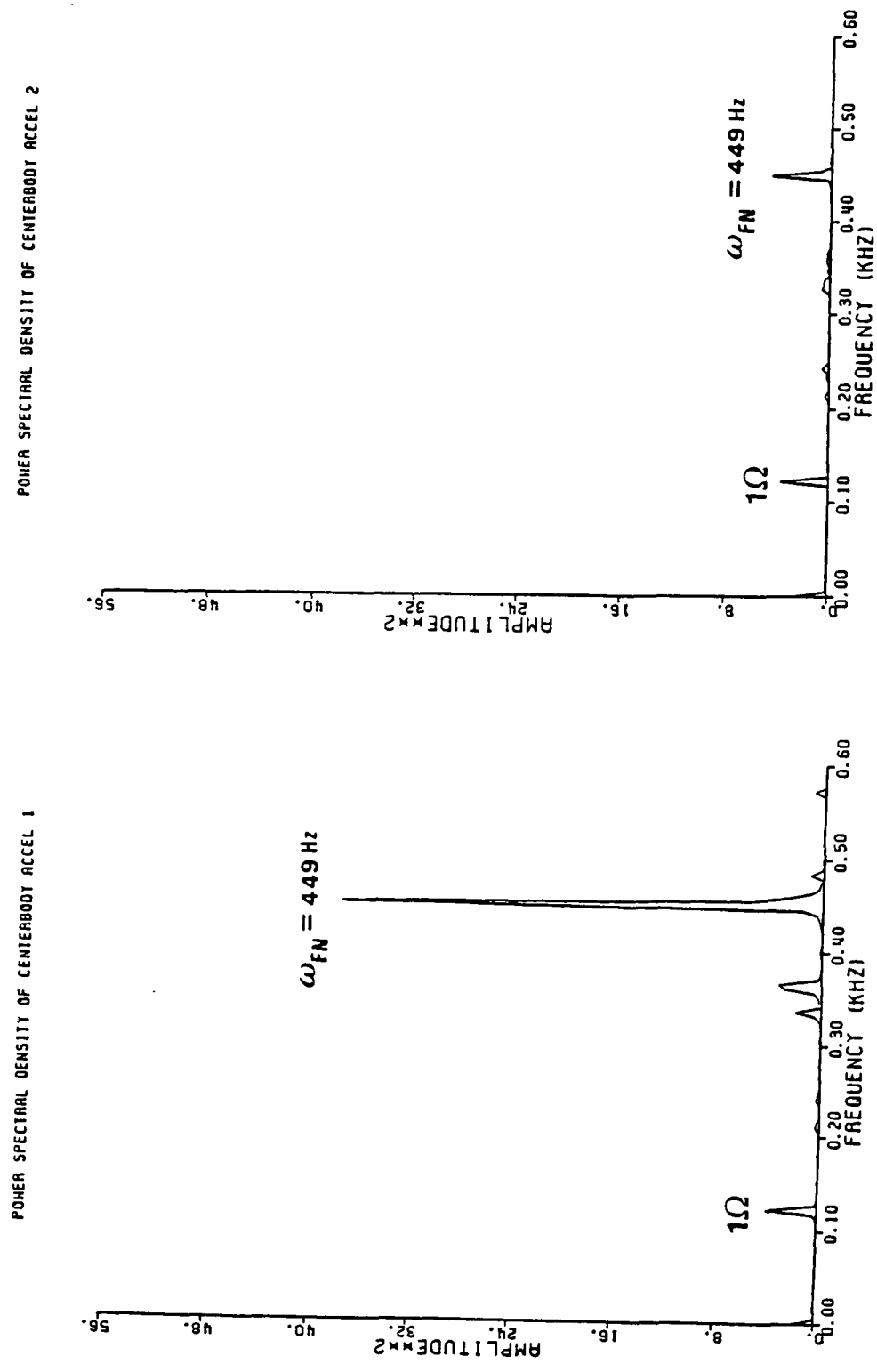

Fig. 5.3 Power spectral densities of the centerbody accelerometer signals of fig. 5.1.

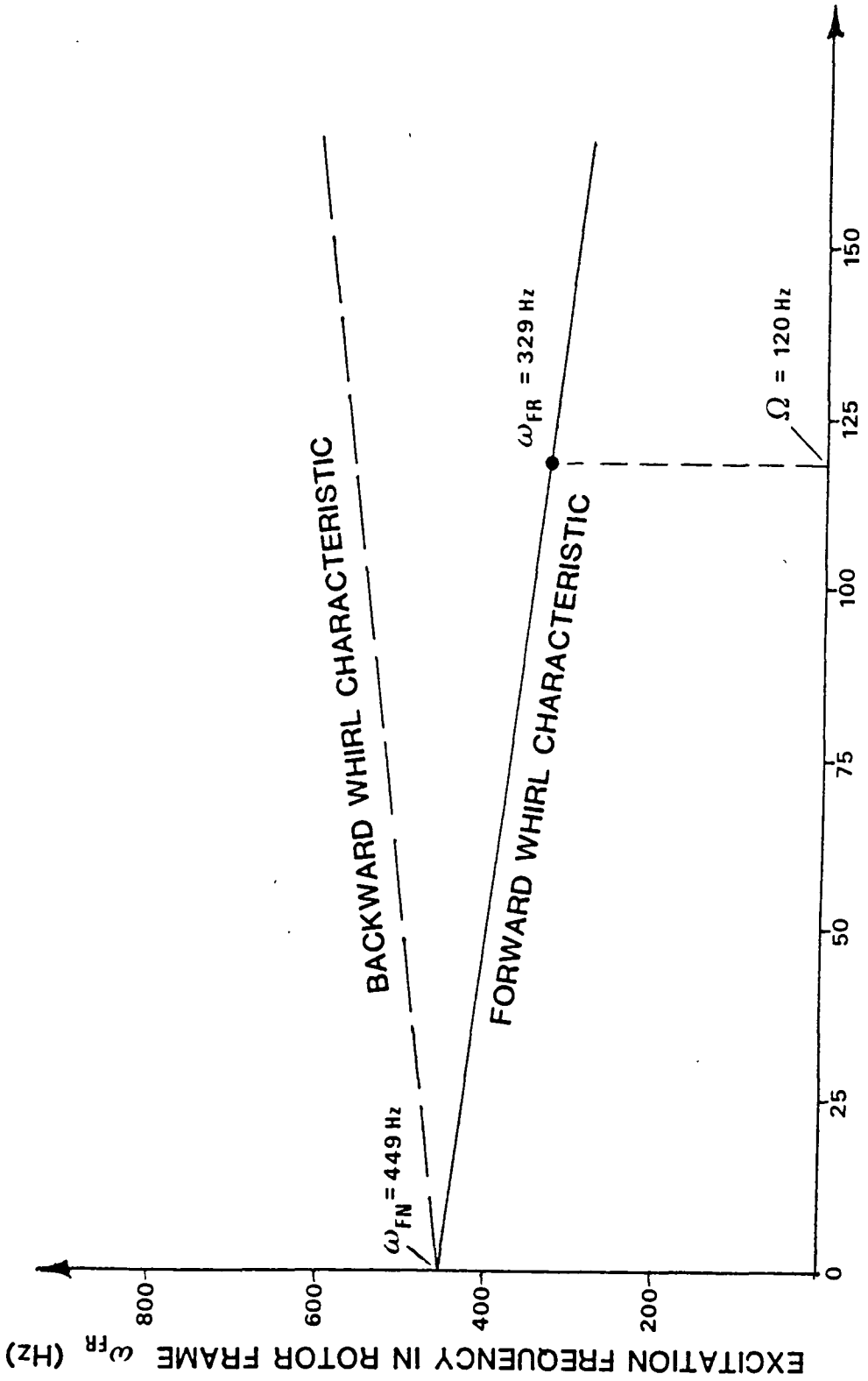

Fig. 5.4 Rotor excitation state corresponding to the data presented in fig. 5.1. Case of: forward whirl excitation, ω_{FN} = 449 Hz, Ω = 120 Hz, ω_{FR} = 329 Hz.

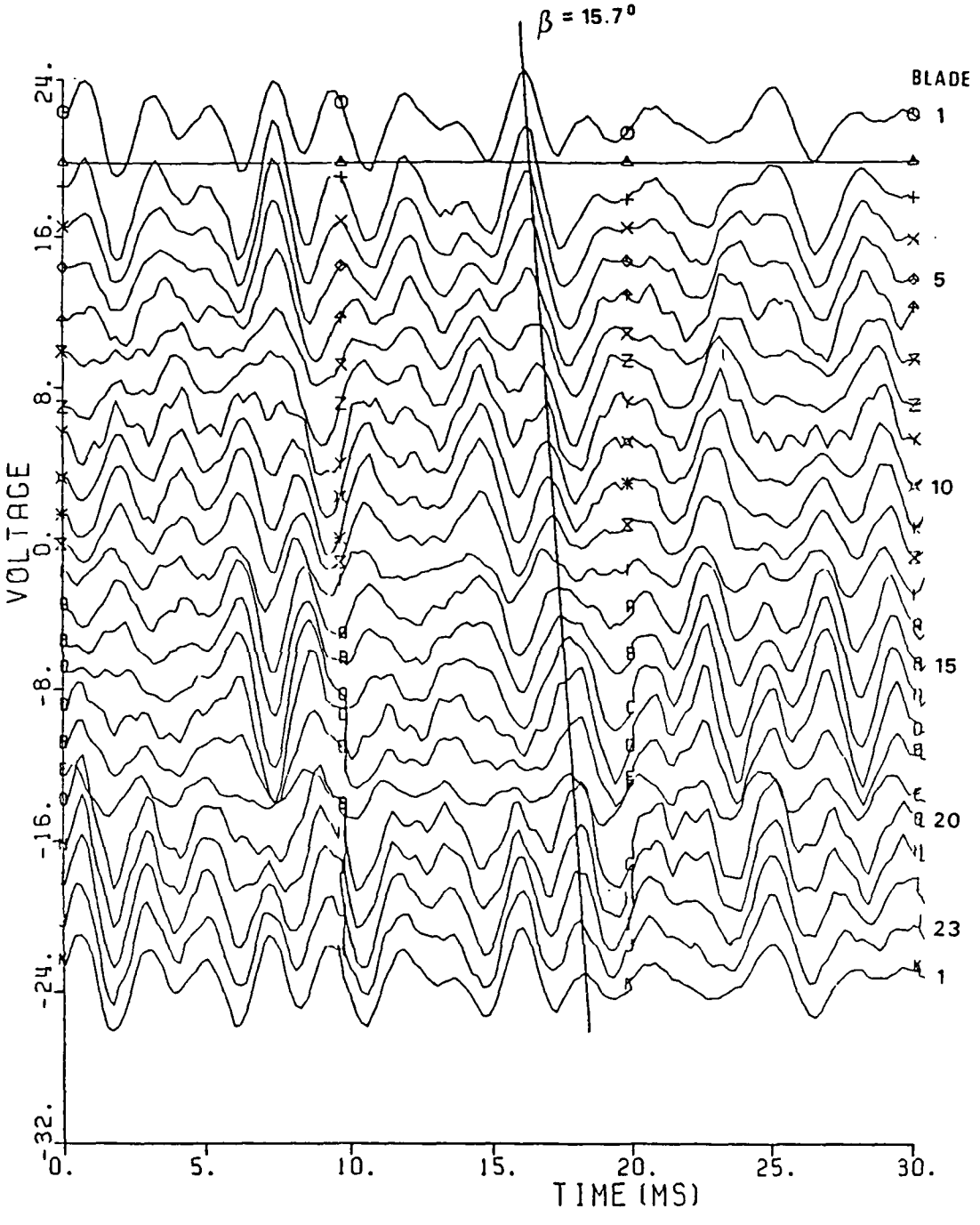

Fig. 5.5 Simultaneous displacement time histories of all blades showing one nodal diameter forward travelling wave pattern. Case of: forward whirl excitation, ω_{FN} = 449 Hz, ω_{FR} = 329 Hz.

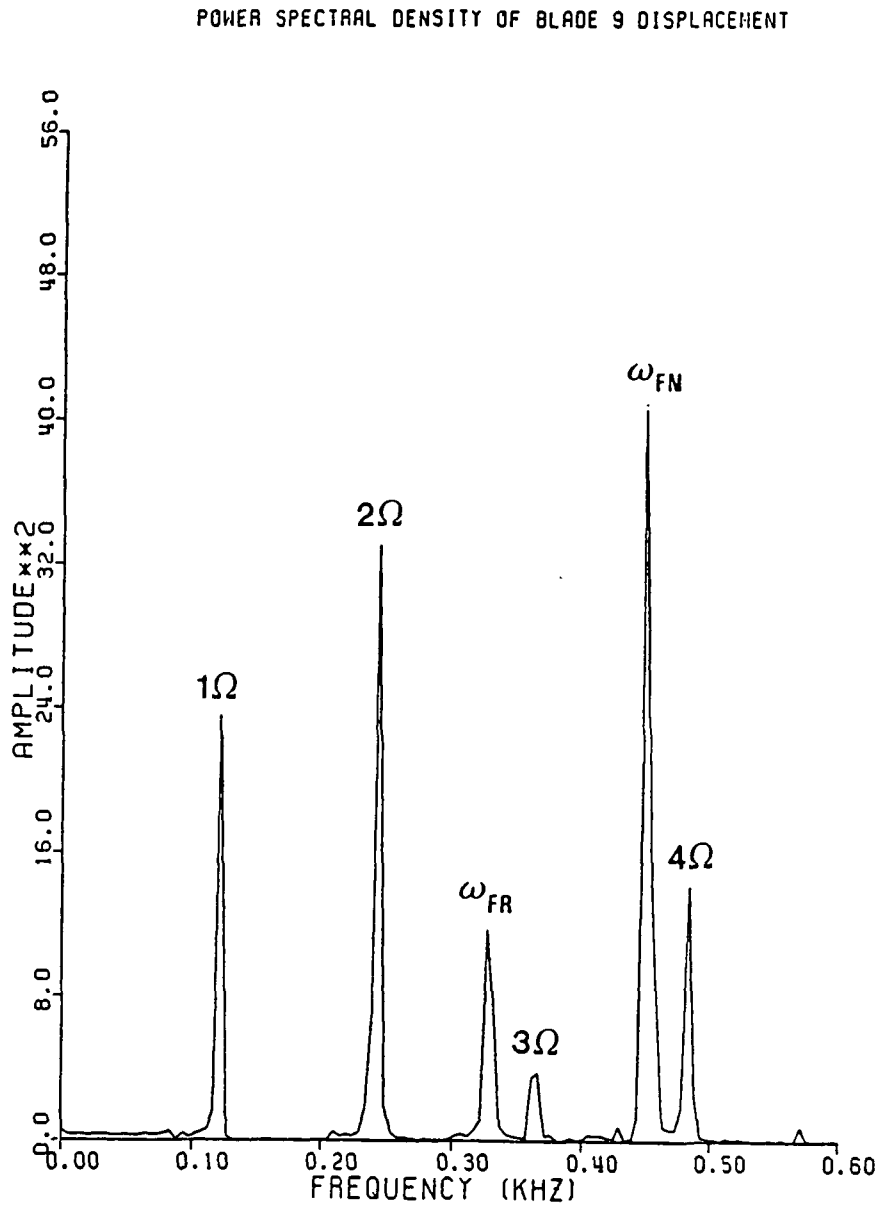

Fig. 5.6 Power spectral density of blade #9 displacement. Case of: forward whirl excitation, ω_{FN} = 449 Hz, Ω = 120 Hz, ω_{FR} = 329 Hz.

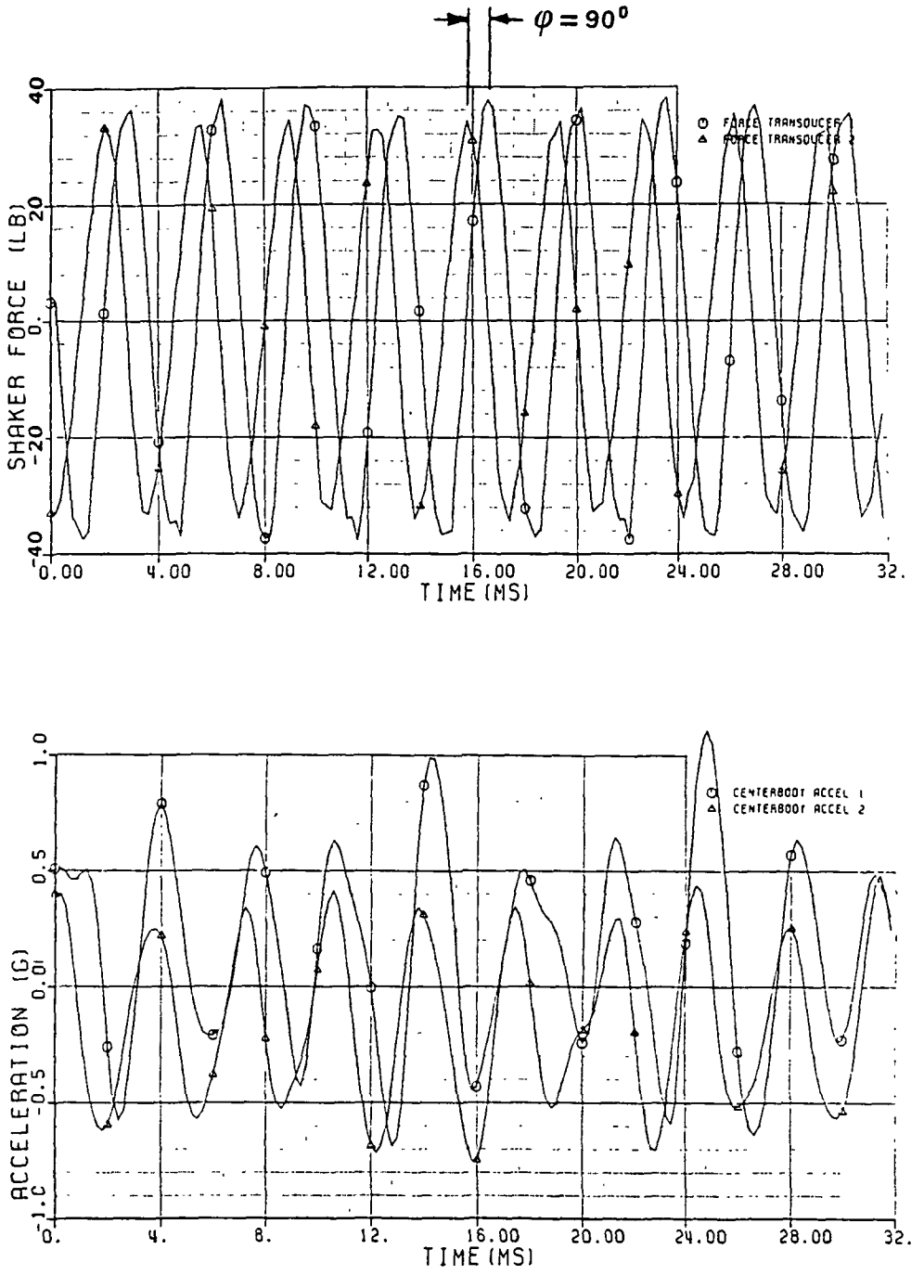

Fig. 5.7 Time history of the shaker force transducer signal (a) and bearing housing accelerometer (b) for the case of: backward whirl excitation, ω_{FN} = 290 Hz, Ω = 60 Hz.

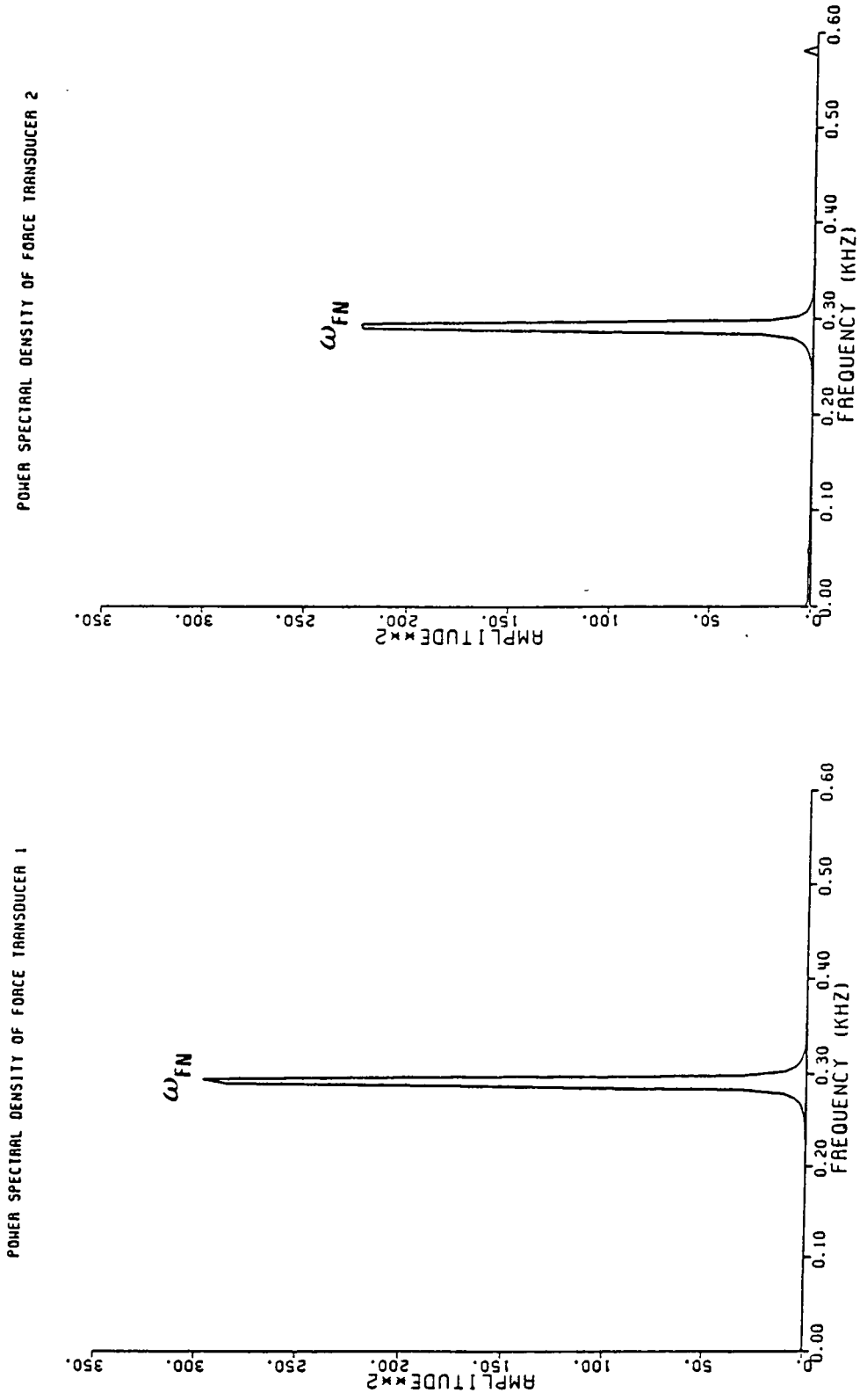

Fig. 5.8 Power spectral densities of the force transducer signals of fig. 5.7.

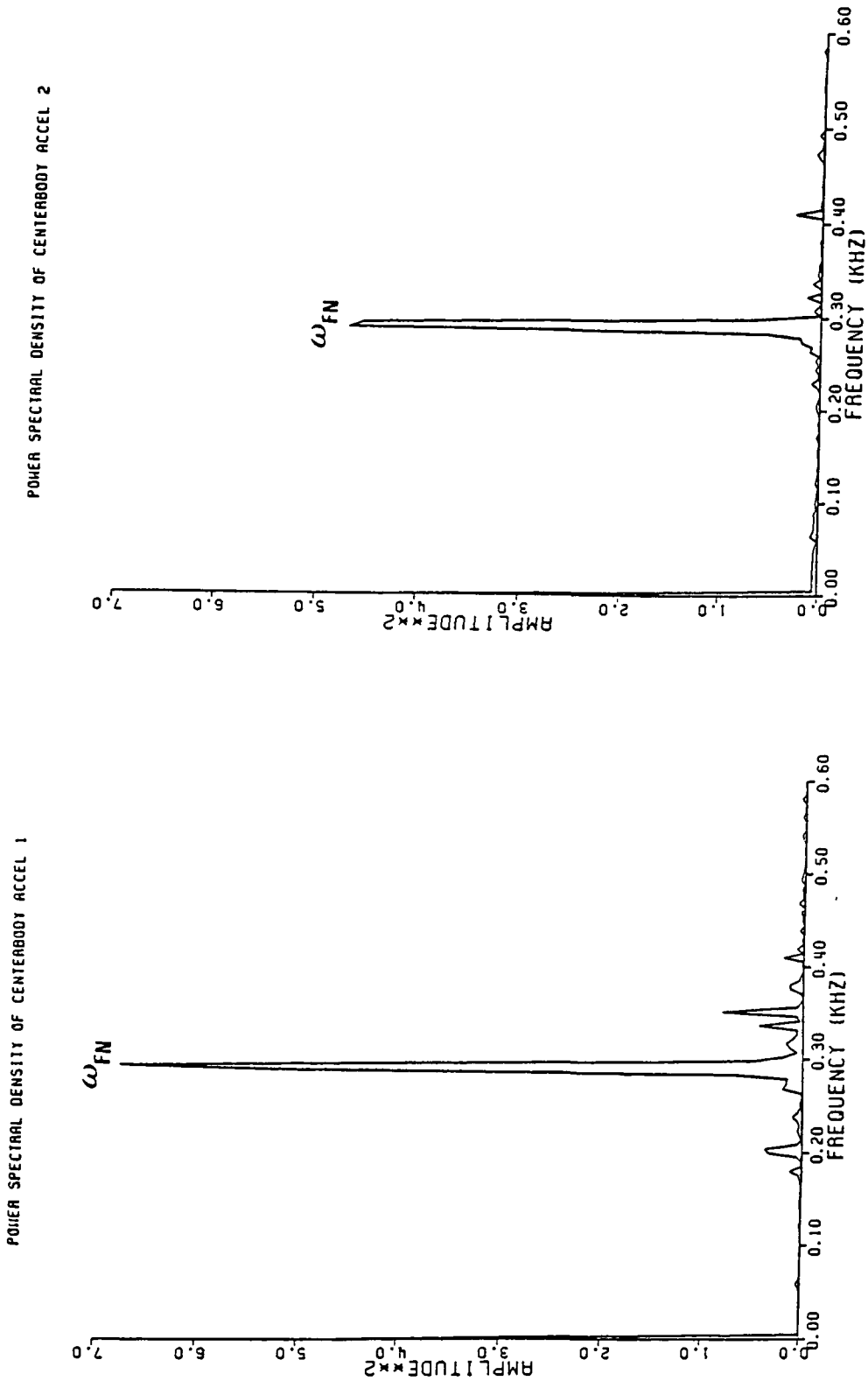

Fig. 5.9 Power spectral densities of the centerbody accelerometer signals of fig. 5.7.

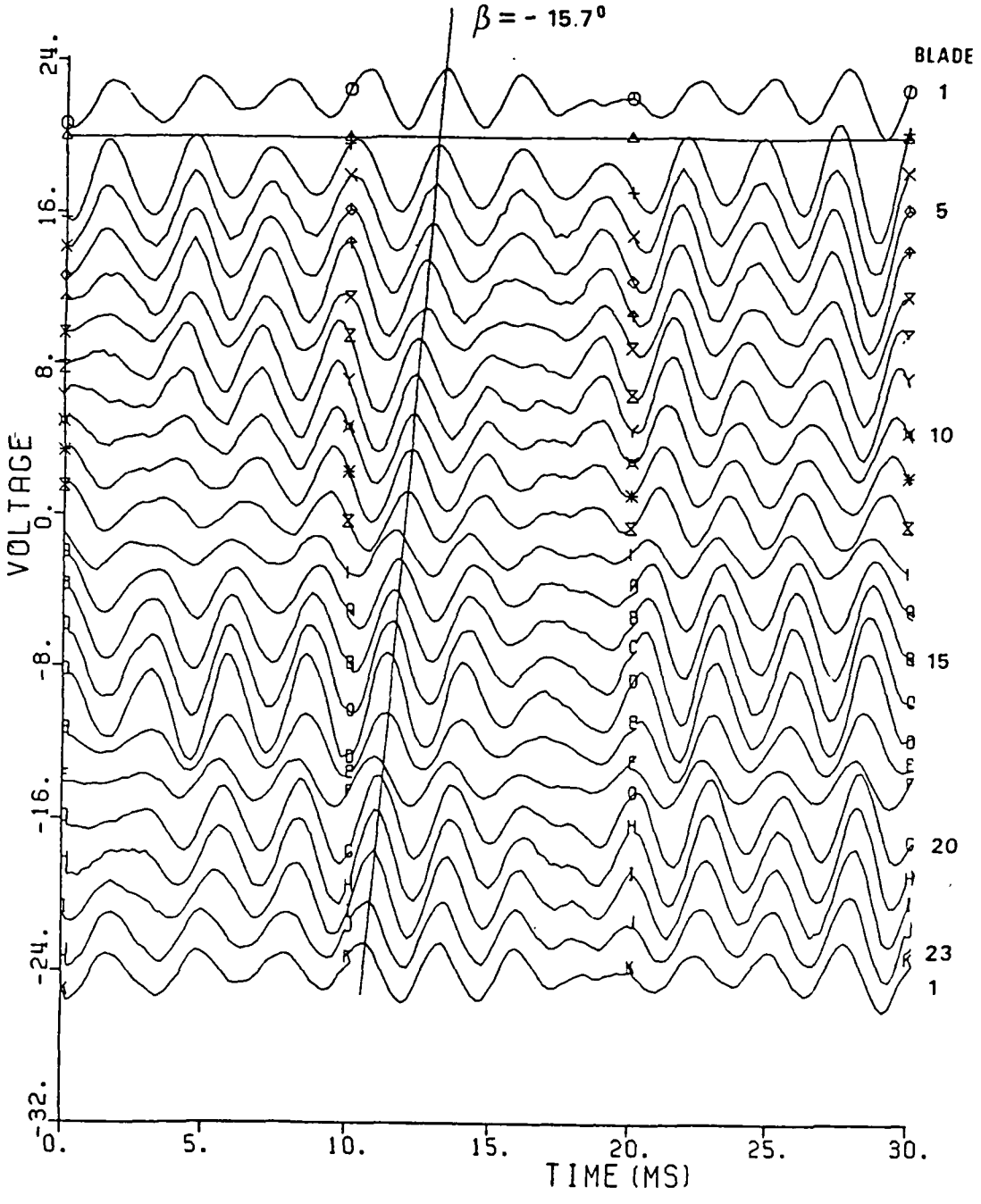

Fig. 5.10 Simultaneous displacement time histories of all blades showing a one nodal diameter backward whirl travelling wave pattern. Case of: backward whirl excitation, ω_{FN} = 290 Hz, Ω = 60 Hz, ω_{FR} = 350 Hz.

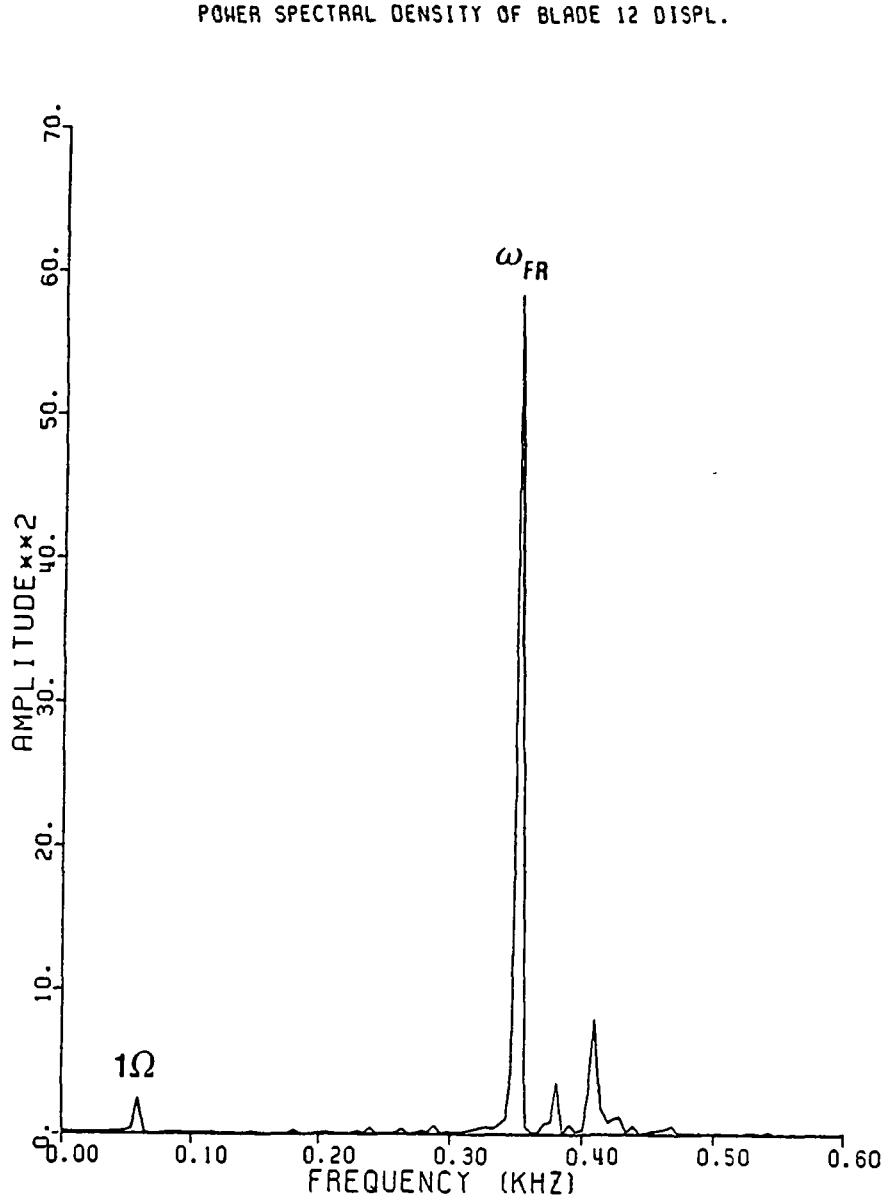

Fig. 5.11 Power spectral density of blade #12 displacement. Case of: backward whirl excitation, ω_{FN} = 290 Hz, Ω = 60 Hz, ω_{FR} = 290 Hz.

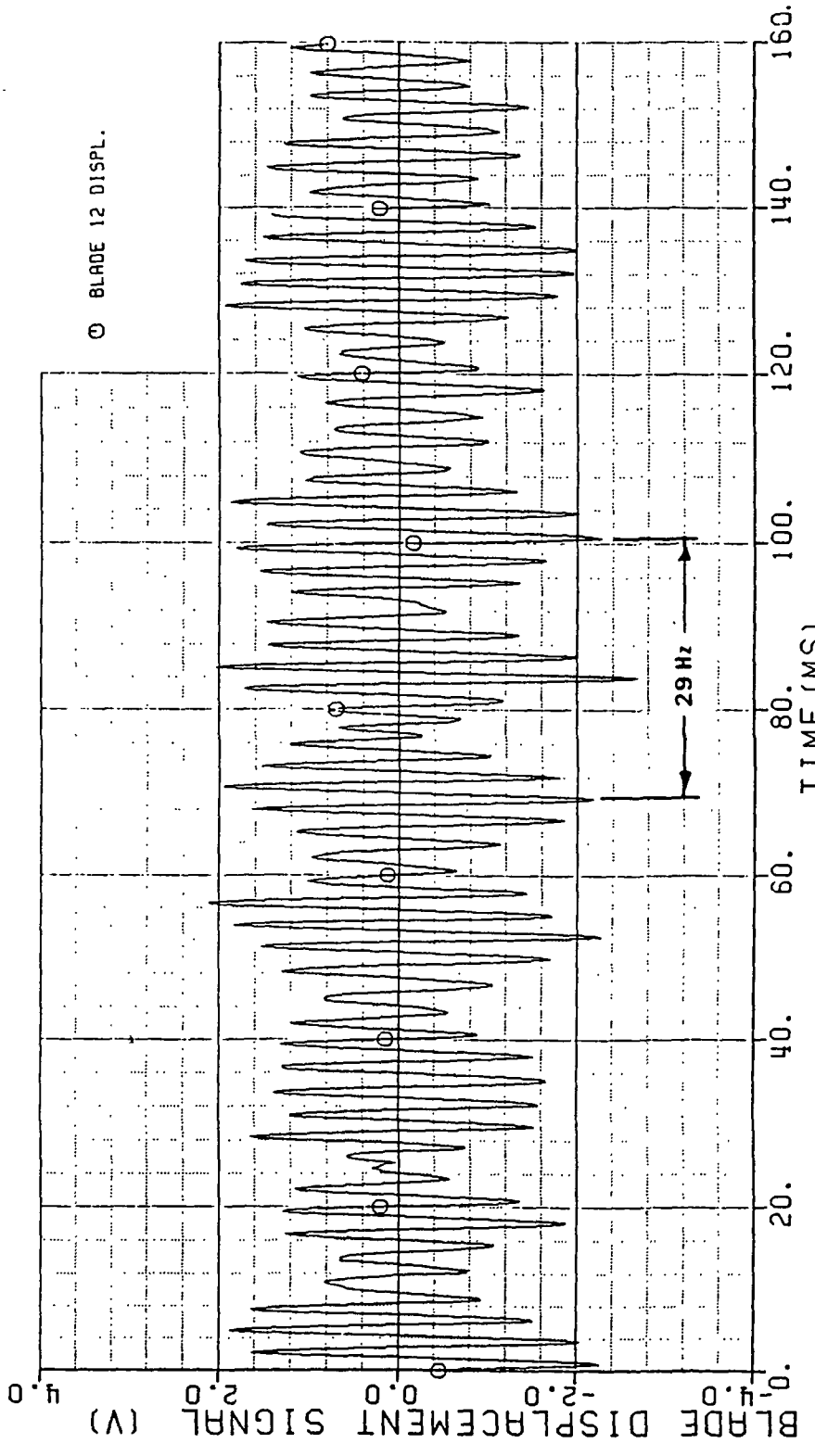

Fig. 5.12 Time history of blade #12 displacement showing beating phenomena due to excitation frequency near the blade 1ND Ω = 60 Hz backward whirl natural frequency of 406 Hz. Case of: backward whirl excitation, ω_{FN} = 290 Hz, Ω = 60 Hz, ω_{FR} = 350 Hz.

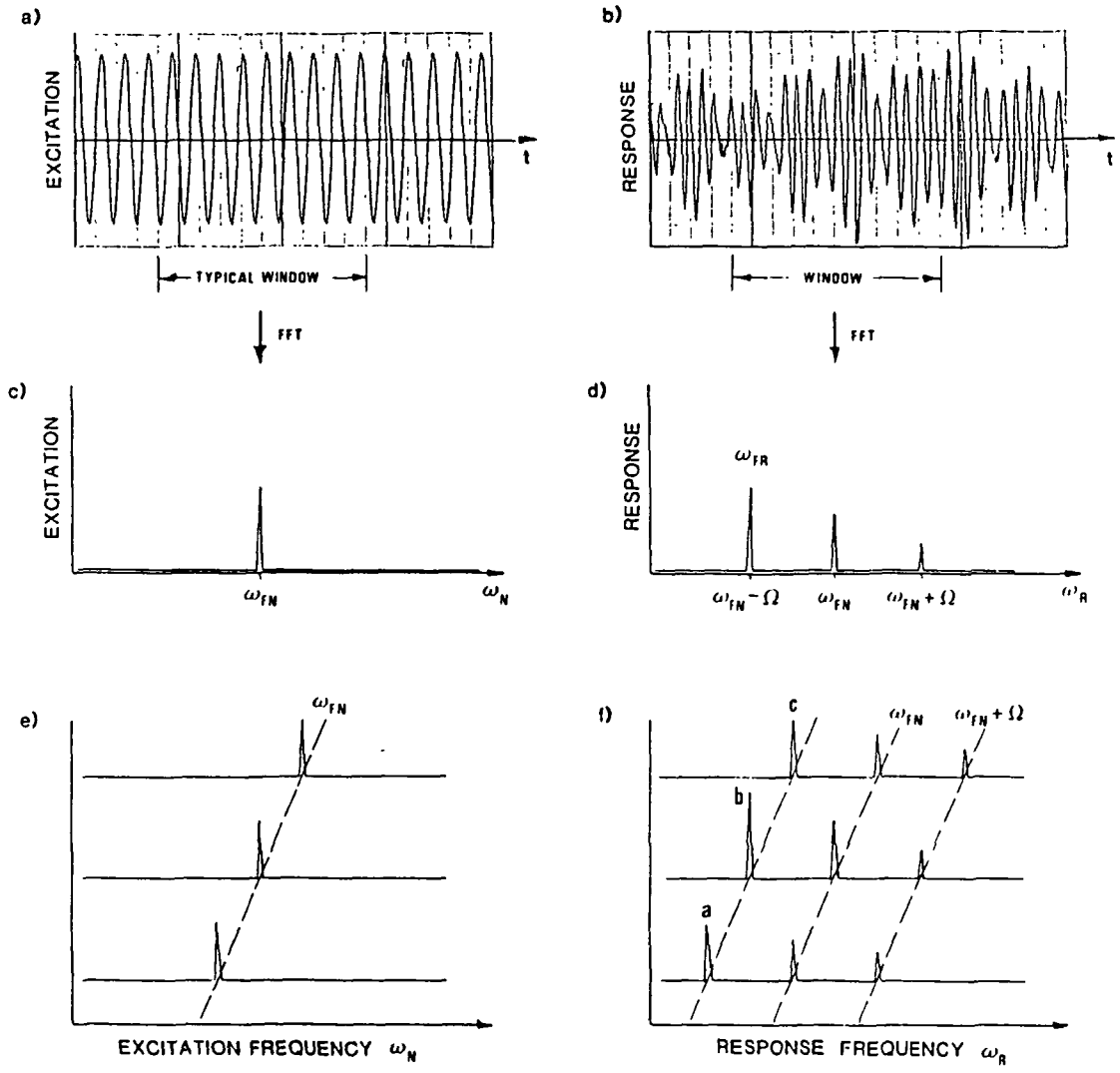

Fig. 5.13 Spectral data reduction scheme showing discrete Fourier transformation of the temporal excitation and response at discrete intervals of excitation frequency, construction of cascade plots, and determination of the system natural frequencies. The particular case shown is for forward whirl excitation.

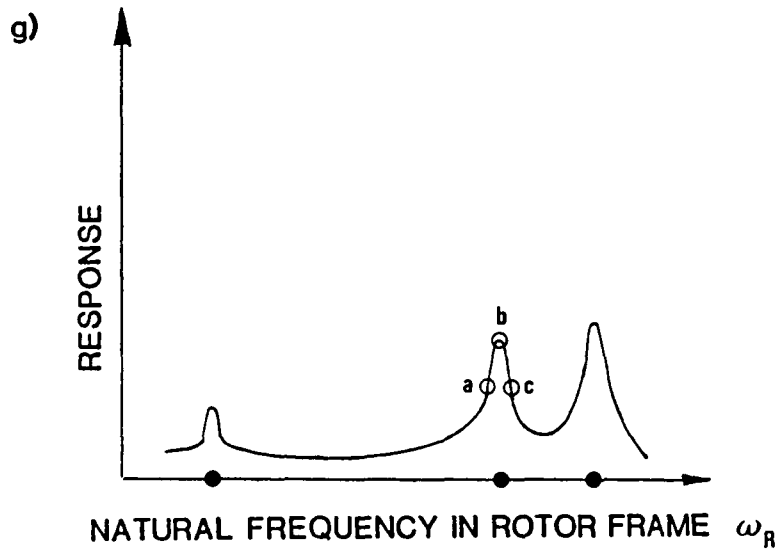

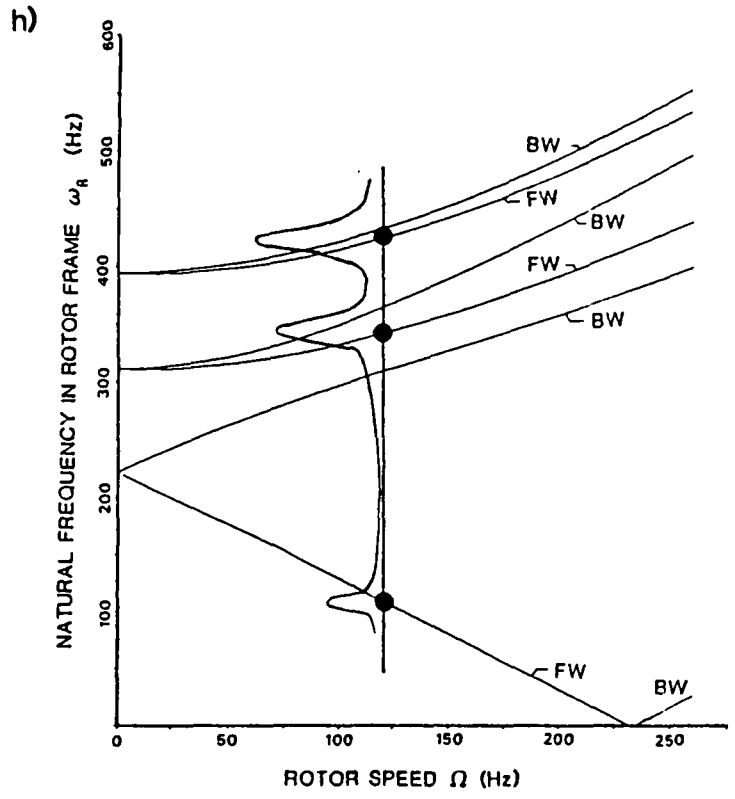

Fig. 5.13 continued

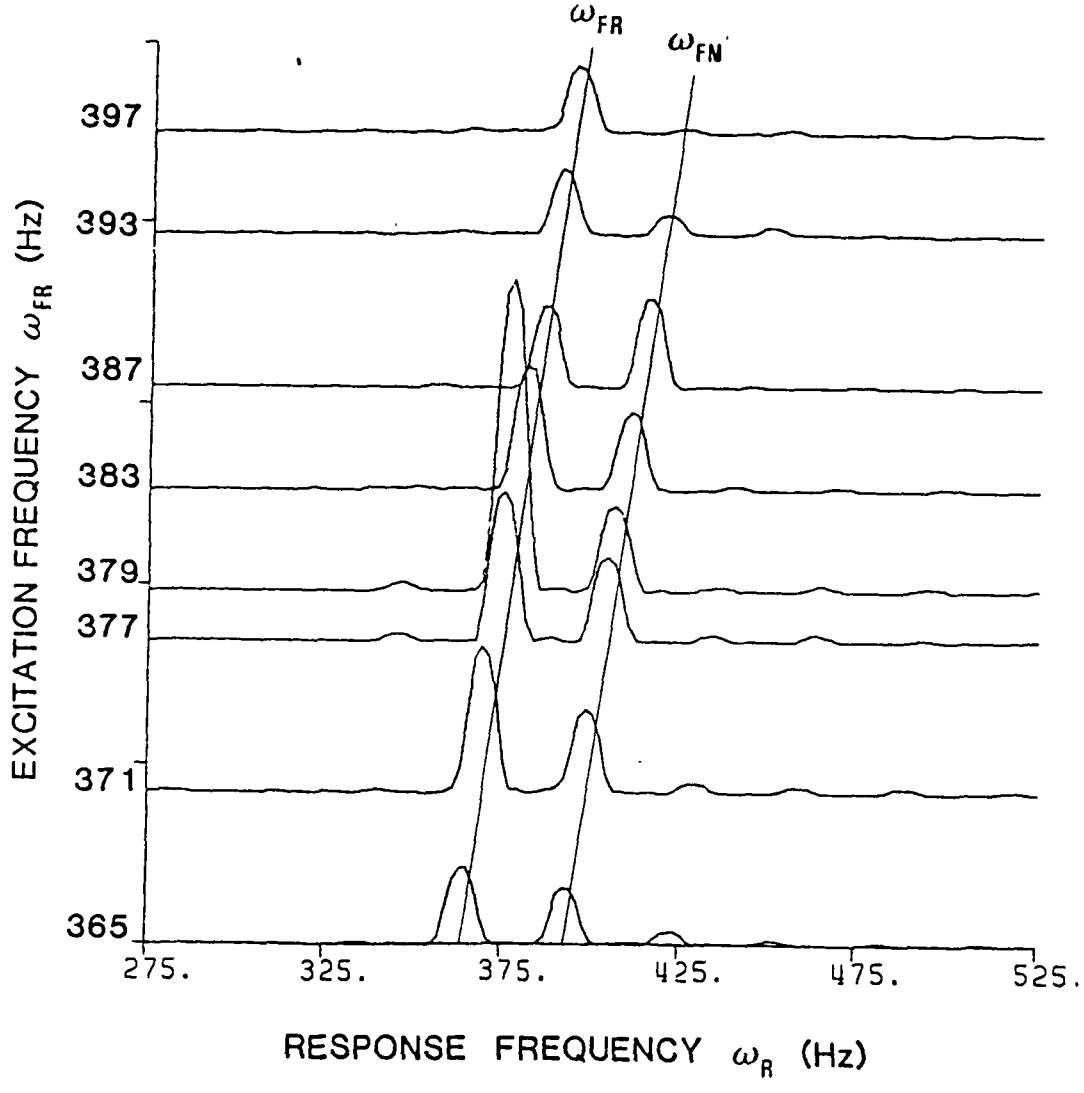

Fig. 5.14 Blade displacement spectral cascade plot for: Ω = 30 Hz, forward whirl excitation of the blade 1ND mode, excitation frequency range ω_{FR} = 365 to 397 Hz.

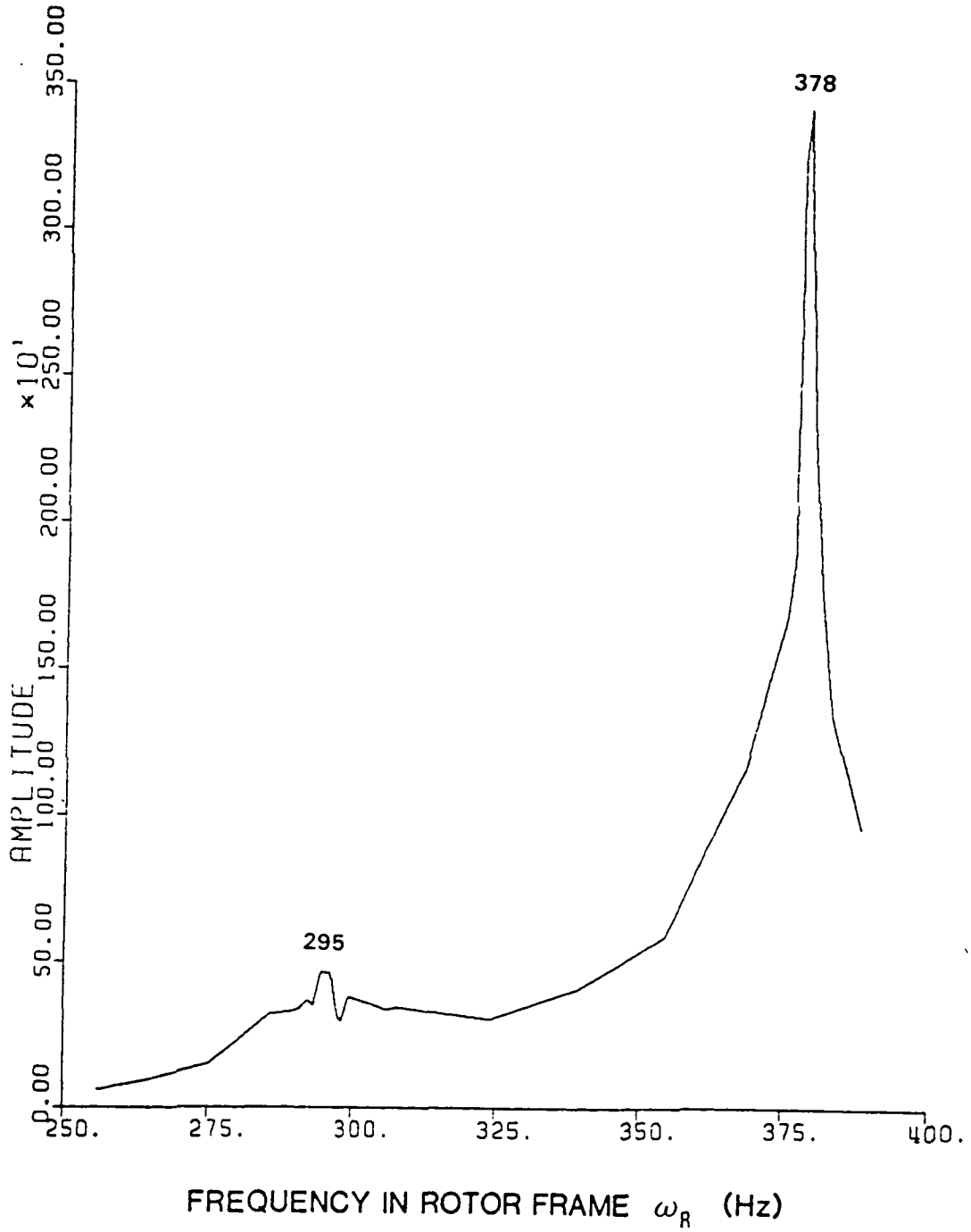

Fig. 5.15 Blade response transfer function for: Ω = 30 Hz, forward whirl excitation.

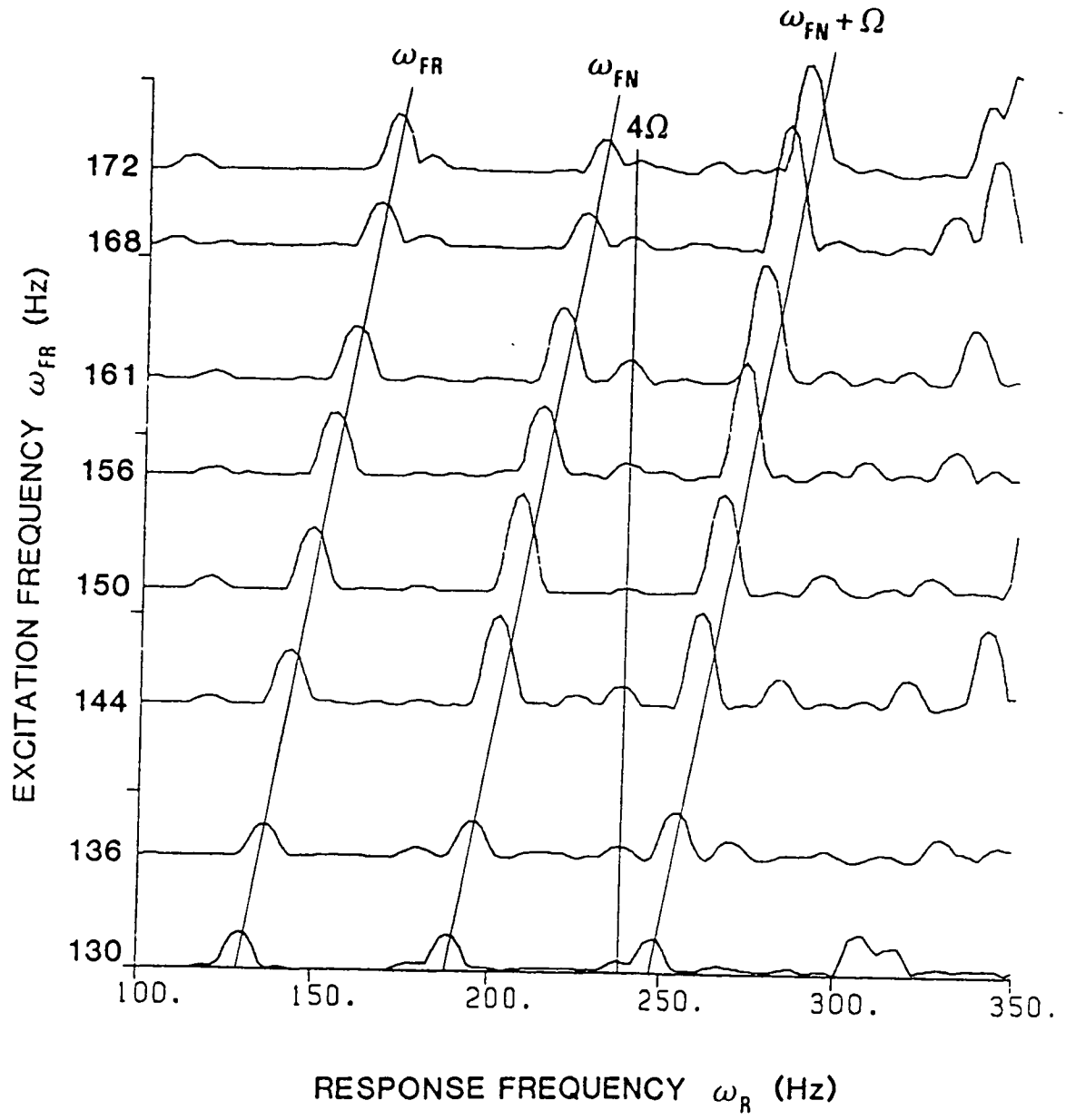

Fig. 5.16 Blade displacement spectral cascade plot for: Ω = 60 Hz, forward whirl excitation of the disk translation mode, excitation frequency range ω_{FR} = 130 to 172 Hz.

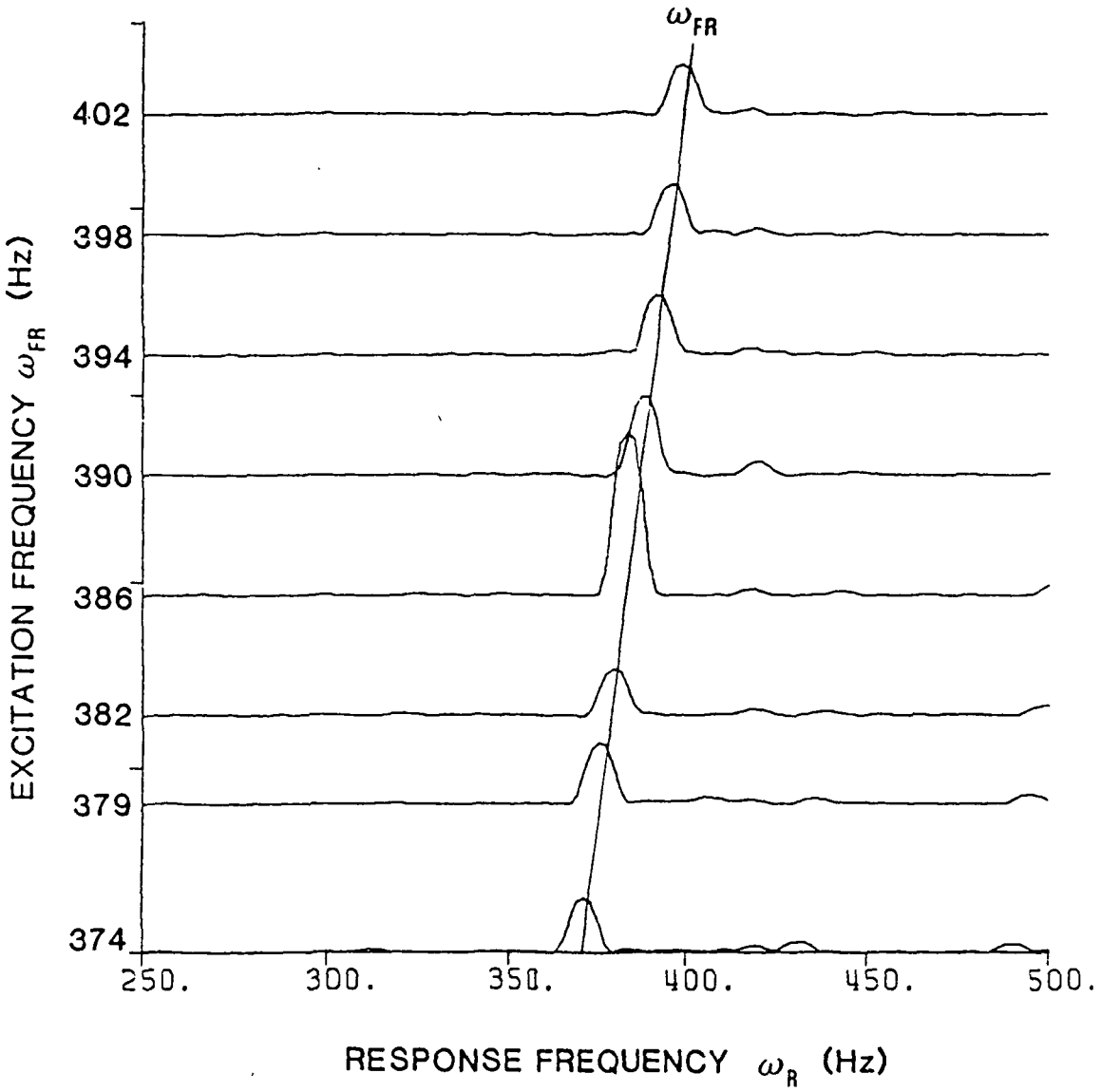

Fig. 5.17 Blade displacement spectral cascade plot for: Ω = 60 Hz, forward whirl excitation of the blade 1ND mode, excitation frequency range ω_{FR} = 374 to 402 Hz.

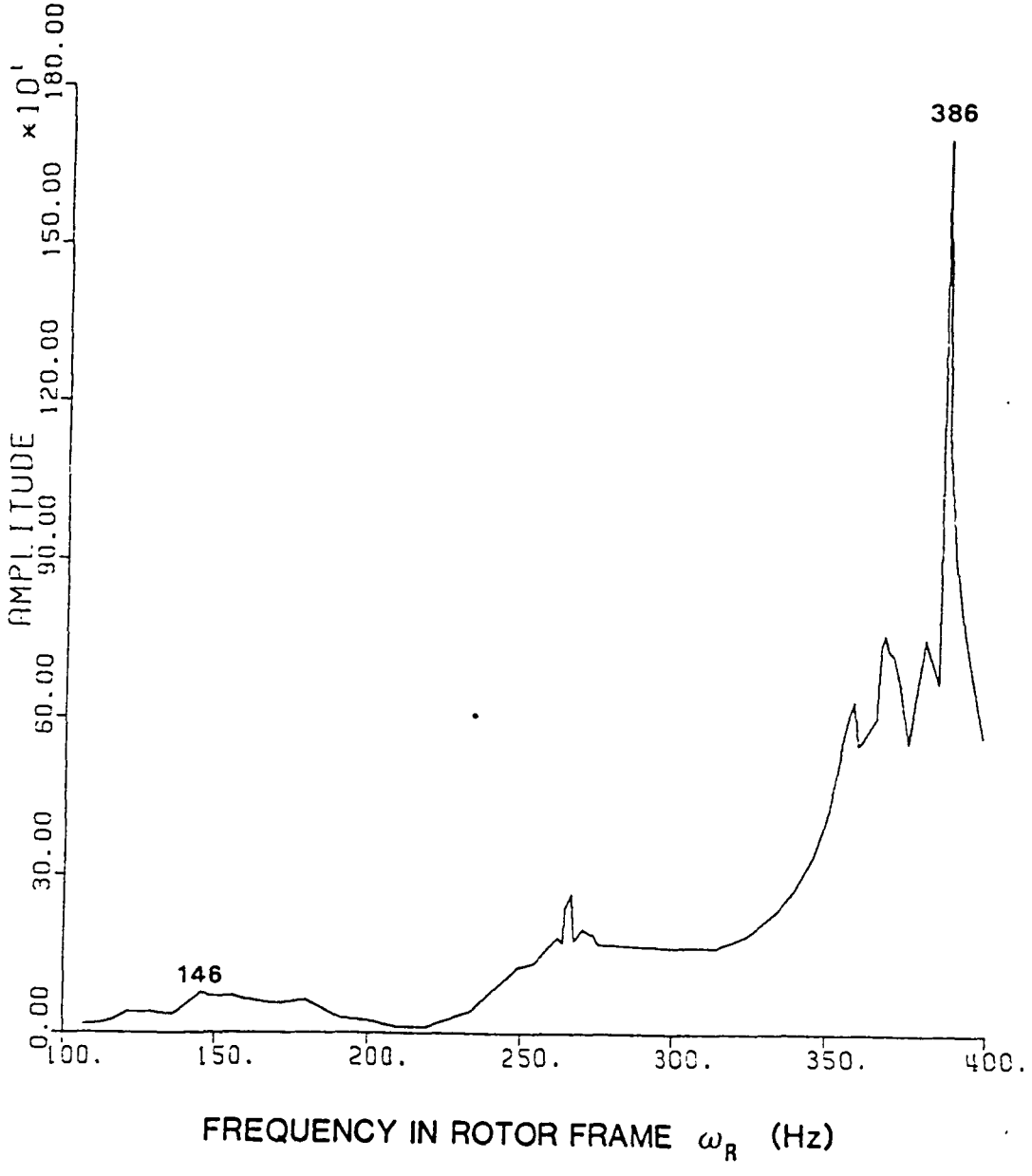

Fig. 5.18 Blade response transfer function for: Ω = 60 Hz, forward whirl excitation.

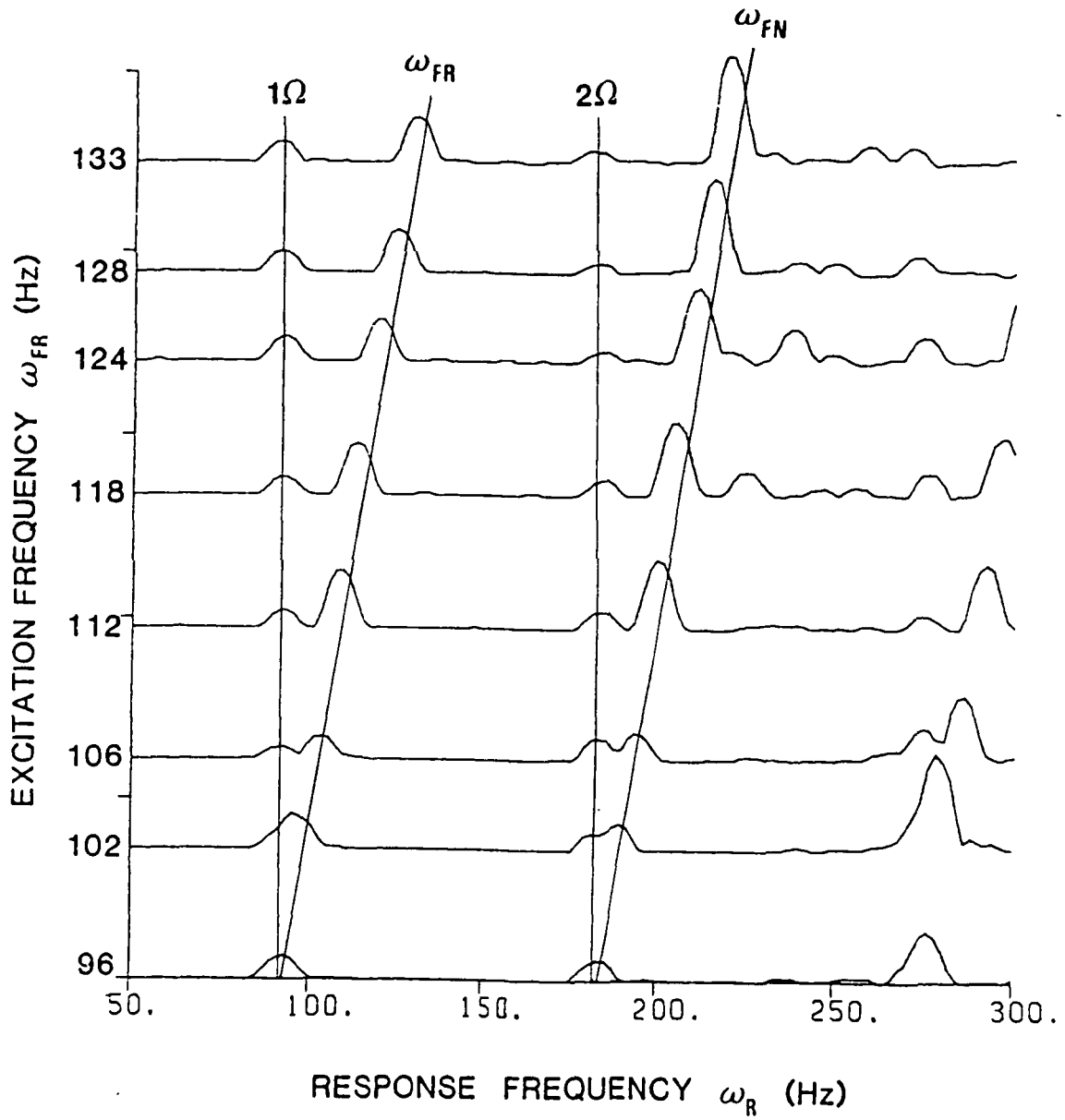

Fig. 5.19 Blade displacement spectral cascade plot for: $\Omega \simeq 90$ Hz, forward whirl excitation of the disk translation mode, excitation frequency range ω_{FR} = 96 to 133 Hz.

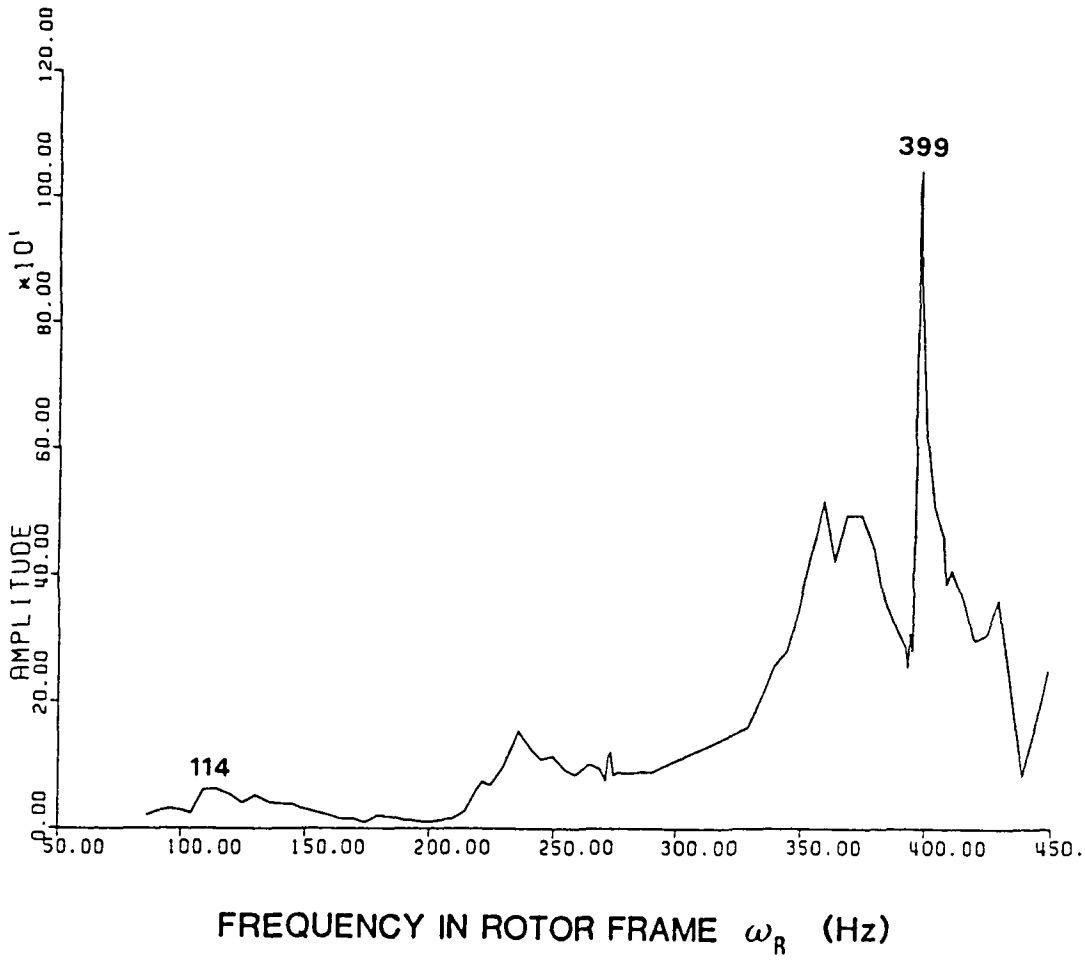

Fig. 5.20 Blade response transfer function for: $\Omega \approx 90$ Hz, forward whirl excitation.

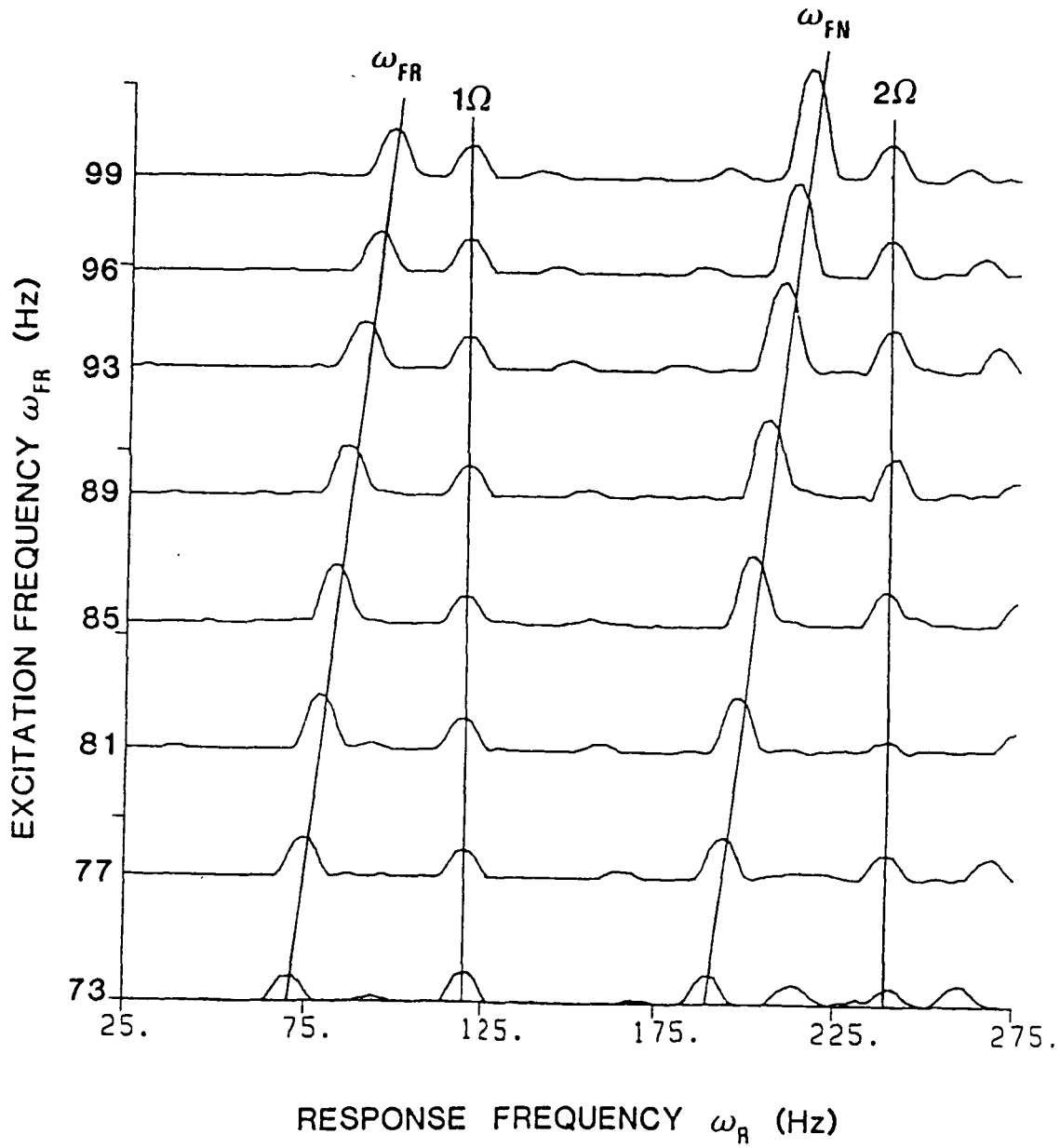

Fig. 5.21 Blade displacement spectral cascade plot for: Ω = 120 Hz, forward whirl excitation of the disk translation mode, excitation frequency range ω_{FR} = 73 to 99 Hz.

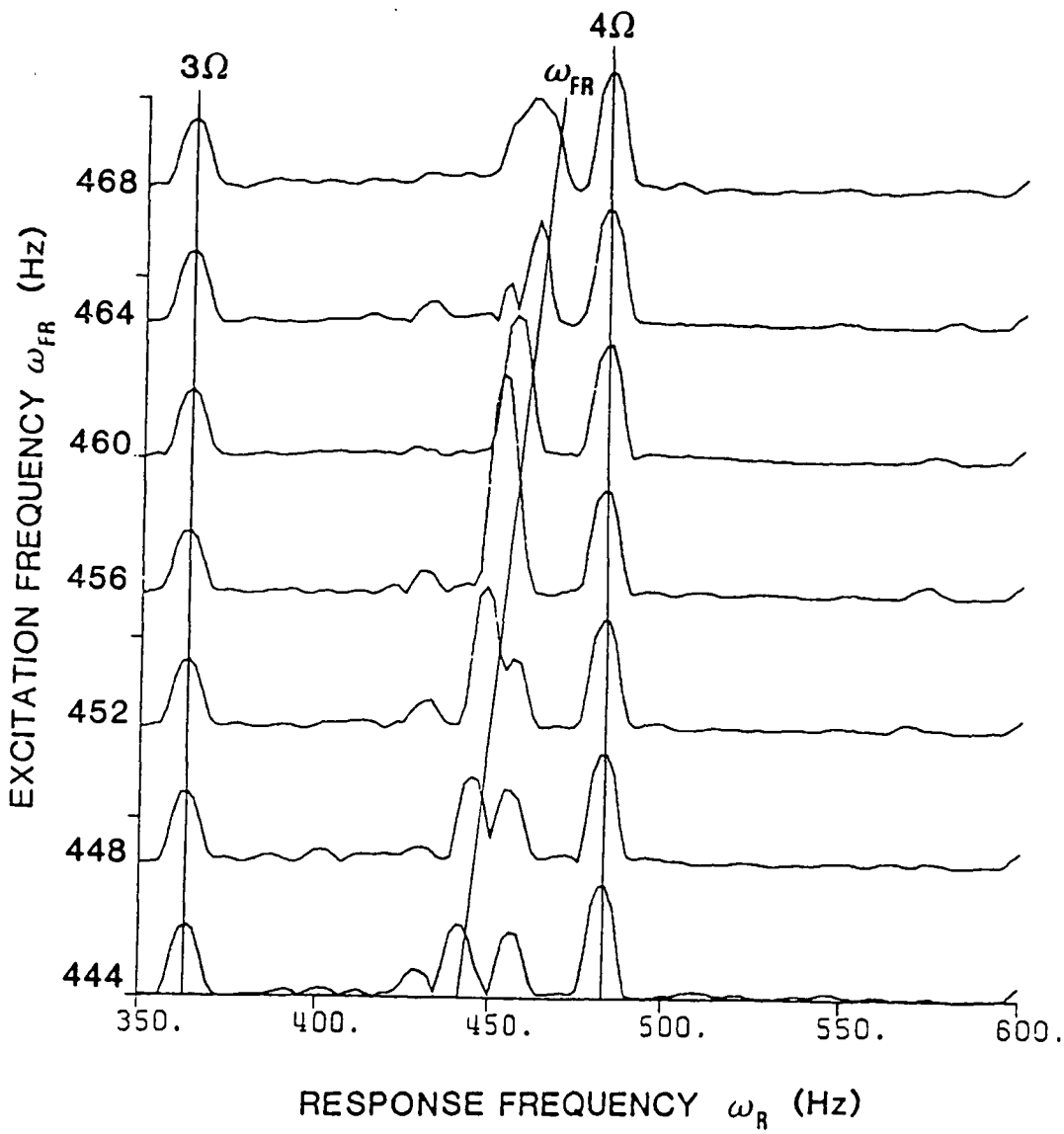

Fig. 5.22 Blade displacement spectral cascade plot for: Ω = 120 Hz, forward whirl excitation of the blade 1ND mode, excitation frequency range ω_{FR} = 444 to 468 Hz.

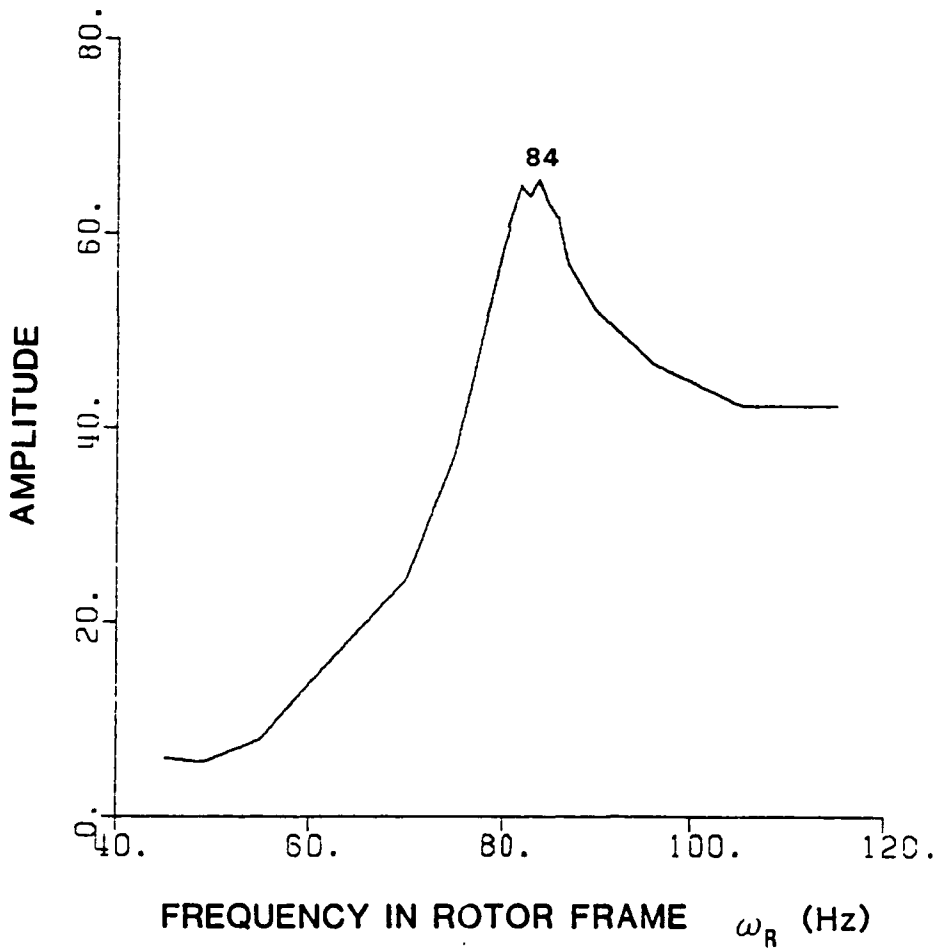

Fig. 5.23 Blade response transfer function for: Ω = 120 Hz, forward whirl excitation, low mode.

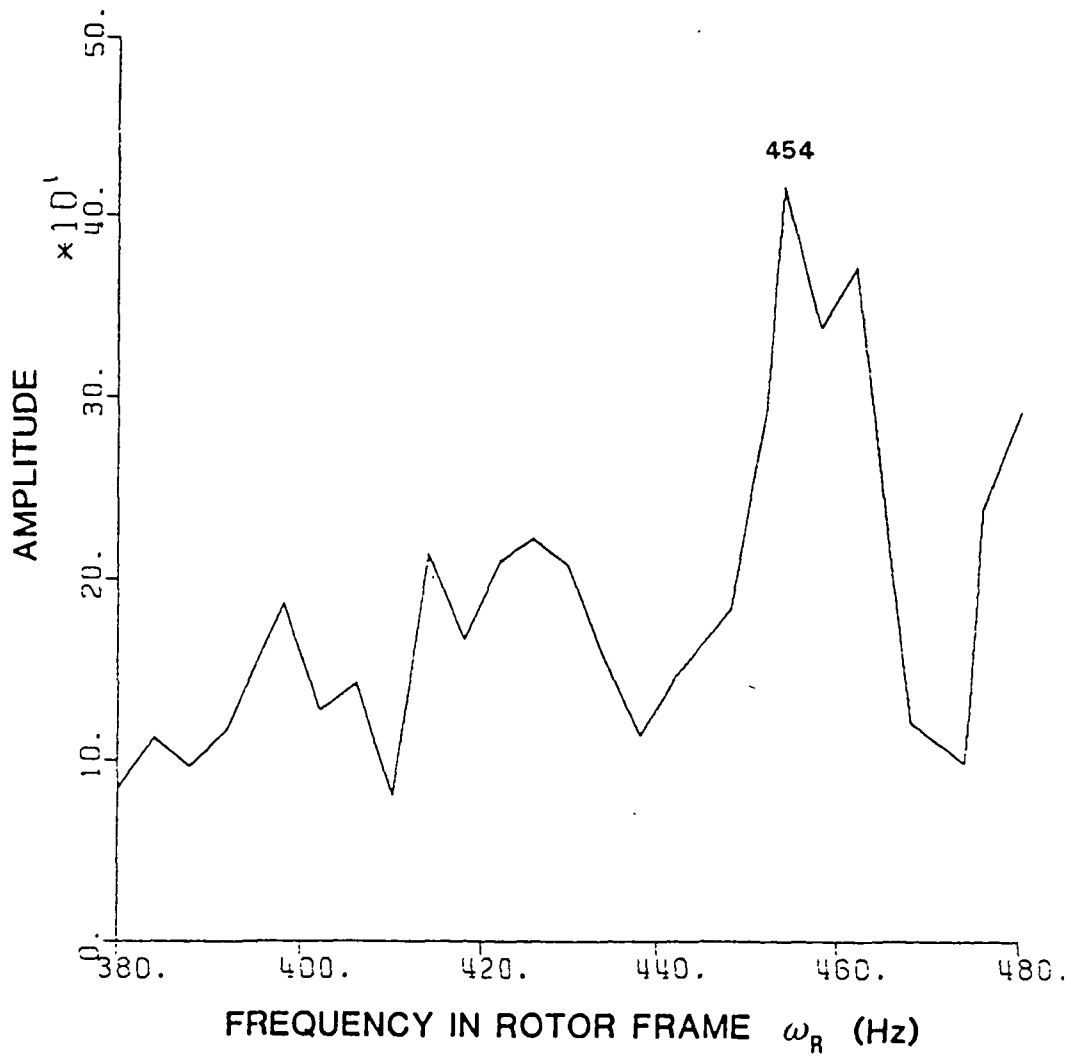

Fig. 5.24 Blade response transfer function for: Ω = 120 Hz, forward whirl excitation, high mode.

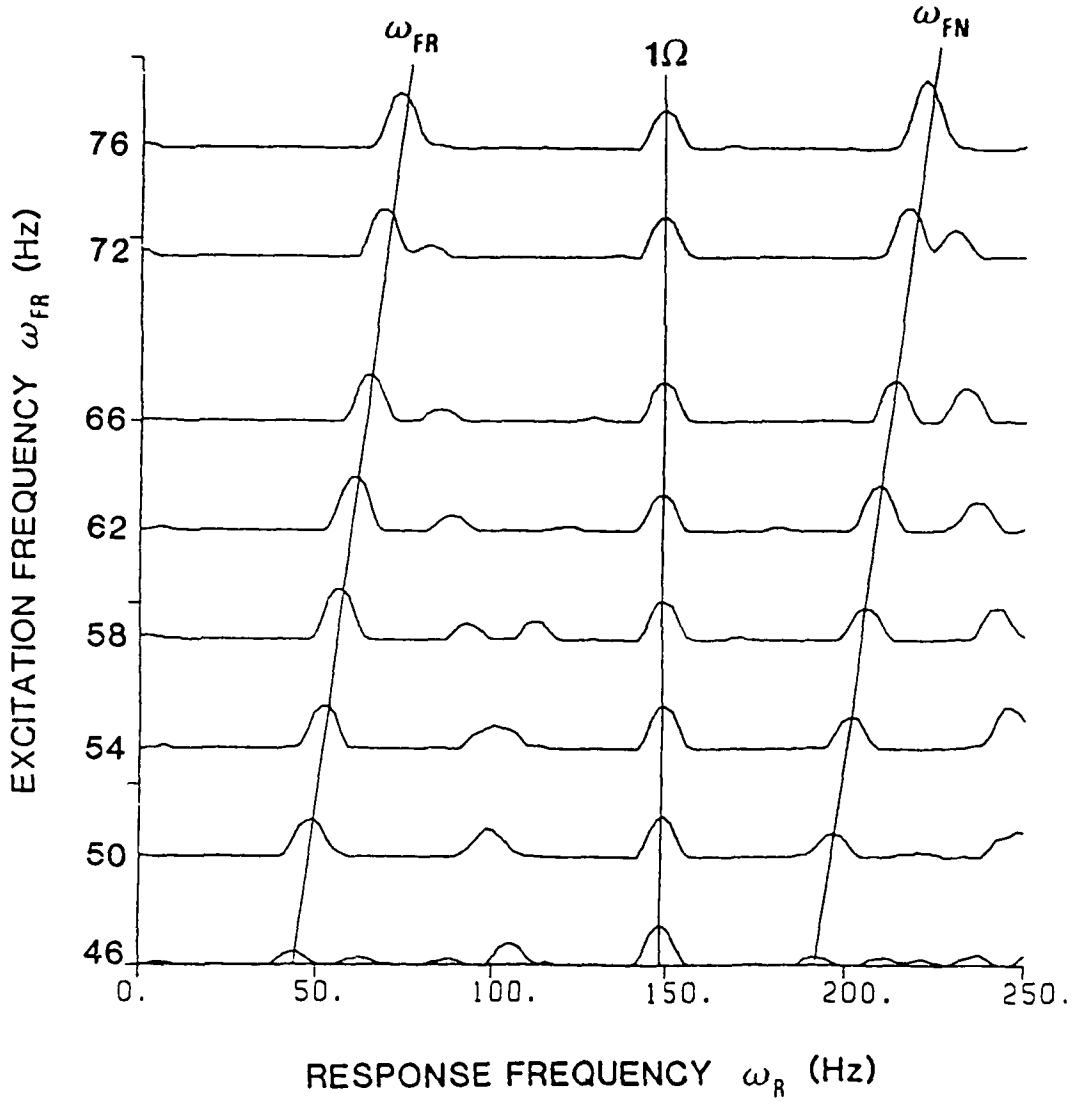

Fig. 5.25 Blade displacement spectral cascade plot for: Ω = 150 Hz, forward whirl excitation of the disk translation mode, excitation frequency range ω_{FR} = 46 to 76 Hz.

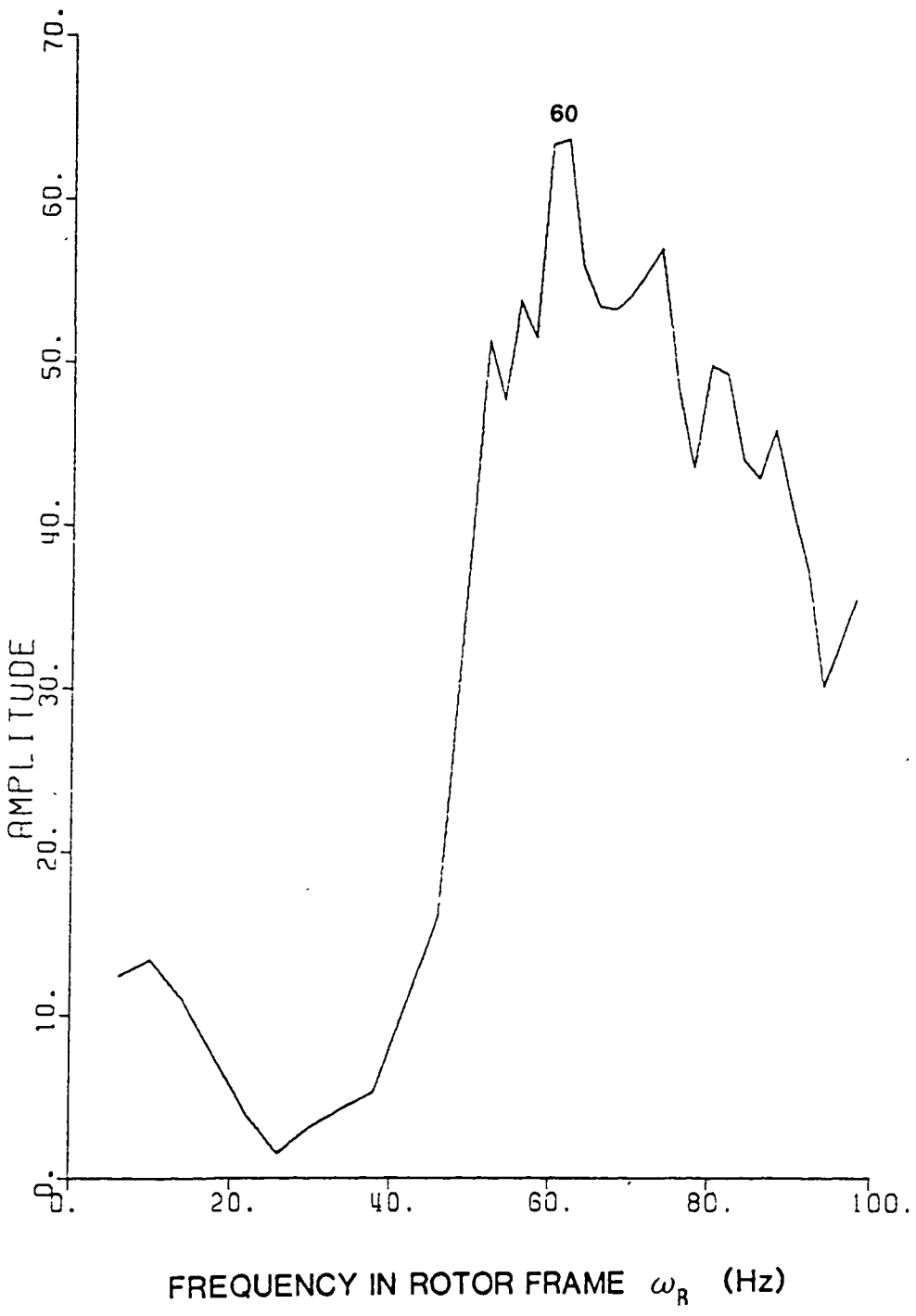

Fig. 5.26 Blade response transfer function for: Ω = 150 Hz, forward whirl excitation.

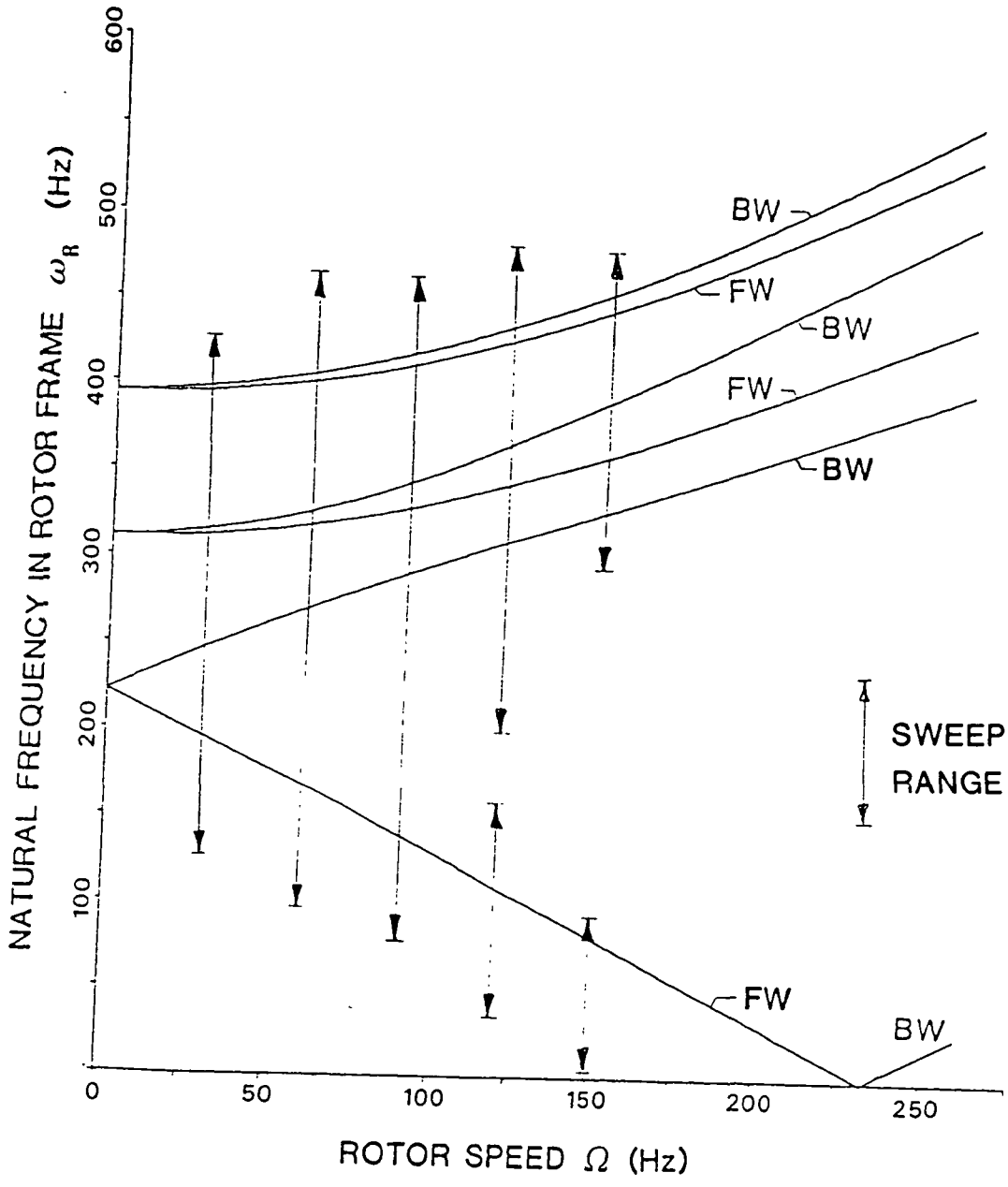

Fig. 5.27 Forward whirl excitation sweep ranges overplotted on the predicted system natural frequency plot.

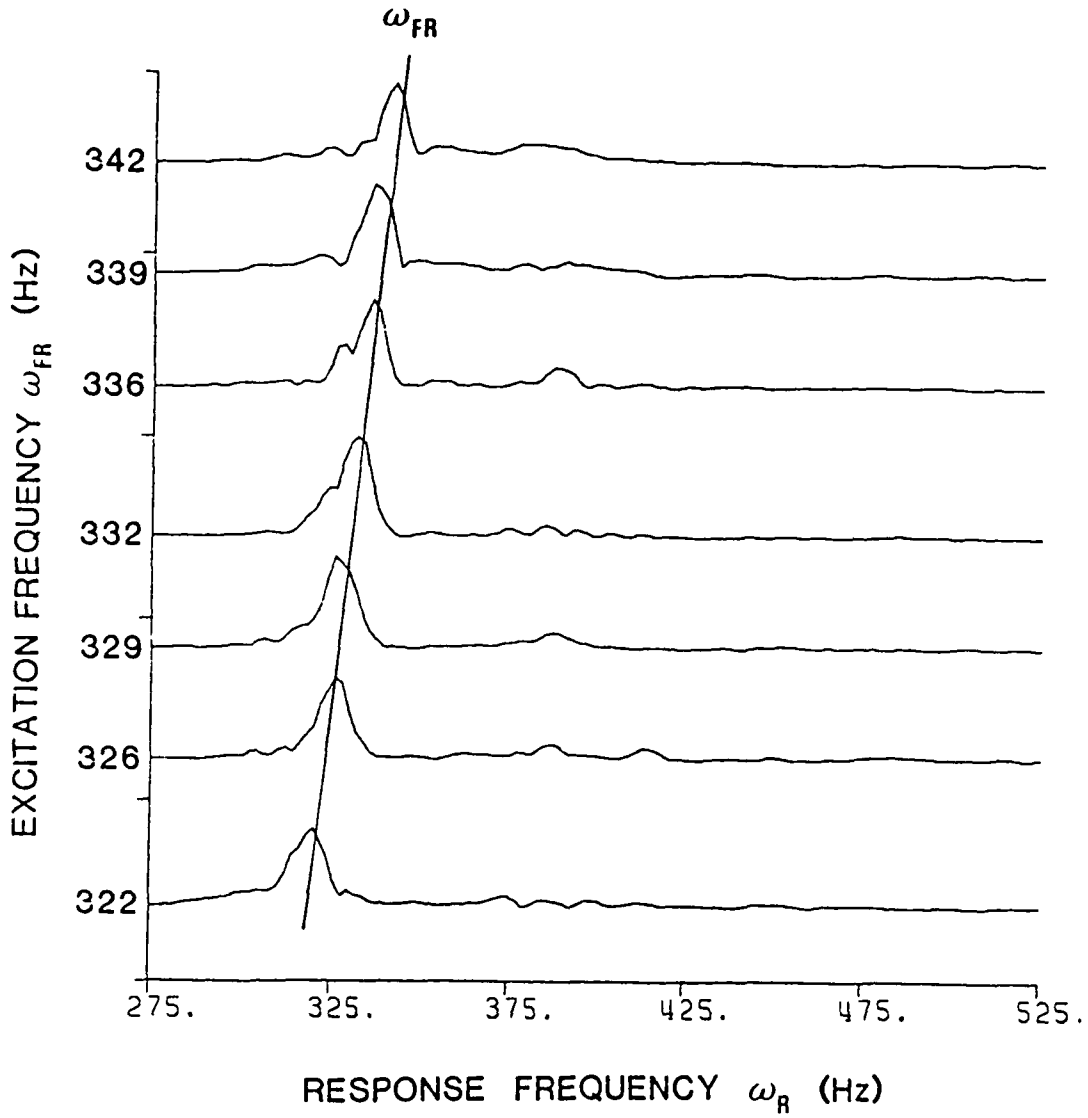

Fig. 5.28 Blade displacement spectral cascade plot for: Ω = 5 Hz, backward whirl excitation of the disk pitch mode, excitation frequency range ω_{FR} = 322 to 342 Hz.

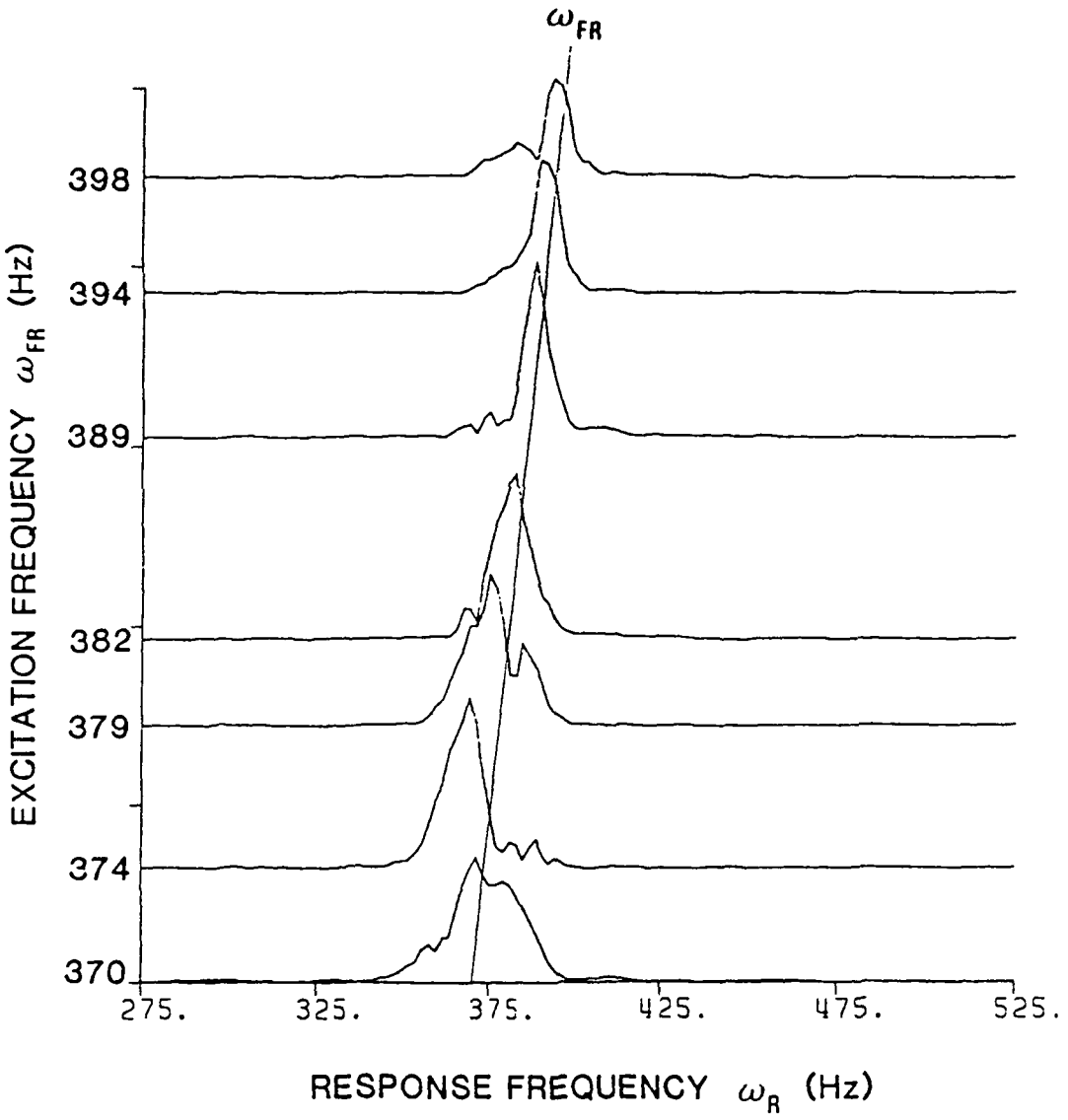

Fig. 5.29 Blade displacement spectral cascade plot for: Ω = 5 Hz, backward whirl excitation of the blade 1ND mode, excitation frequency range ω_{FR} = 370 Hz to 398 Hz.

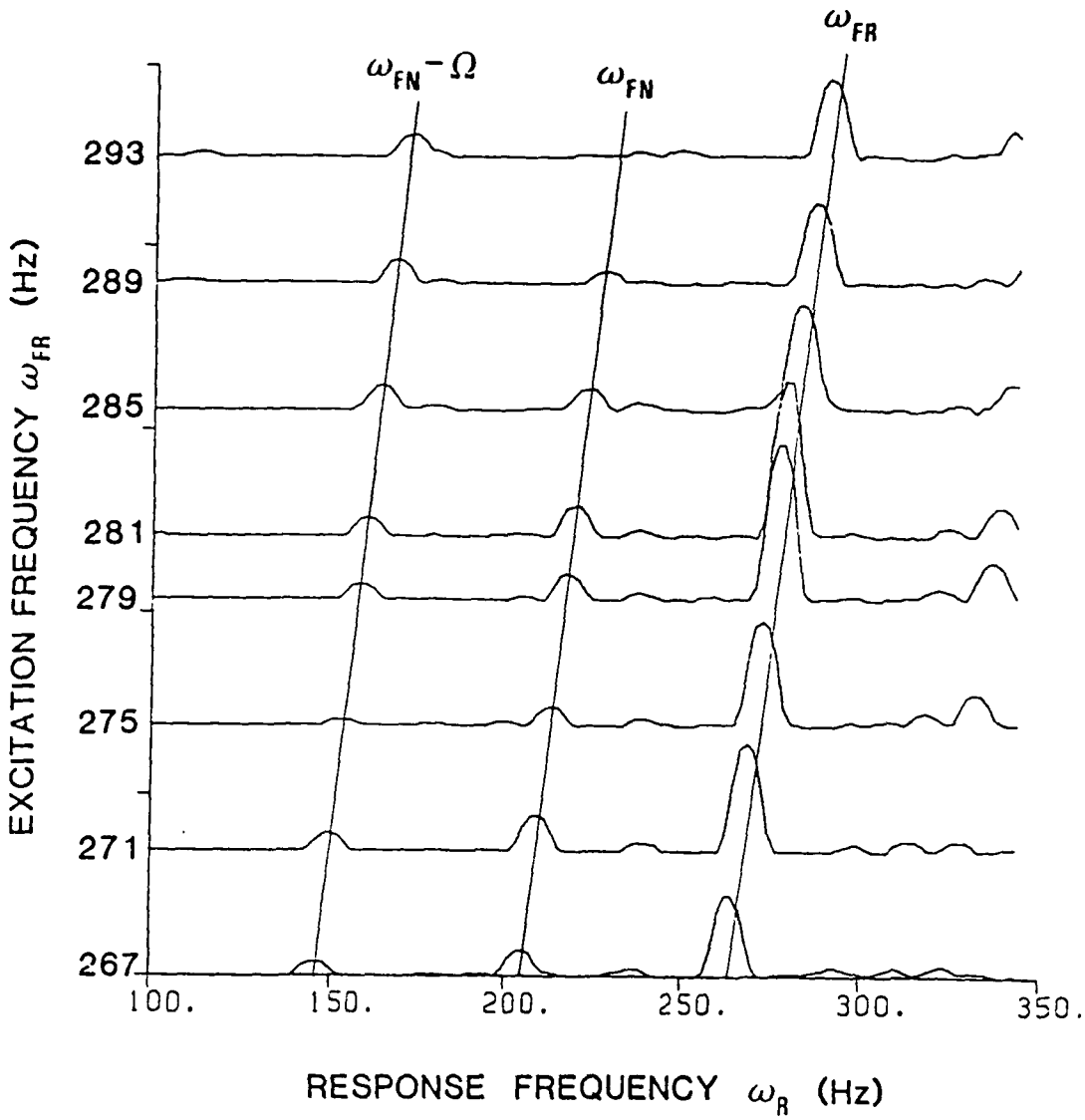

Fig. 5.30 Blade displacement spectral cascade plot for: Ω = 60 Hz, backward whirl excitation of the disk pitch mode, excitation frequency range ω_{FR} = 267 to 293 Hz.

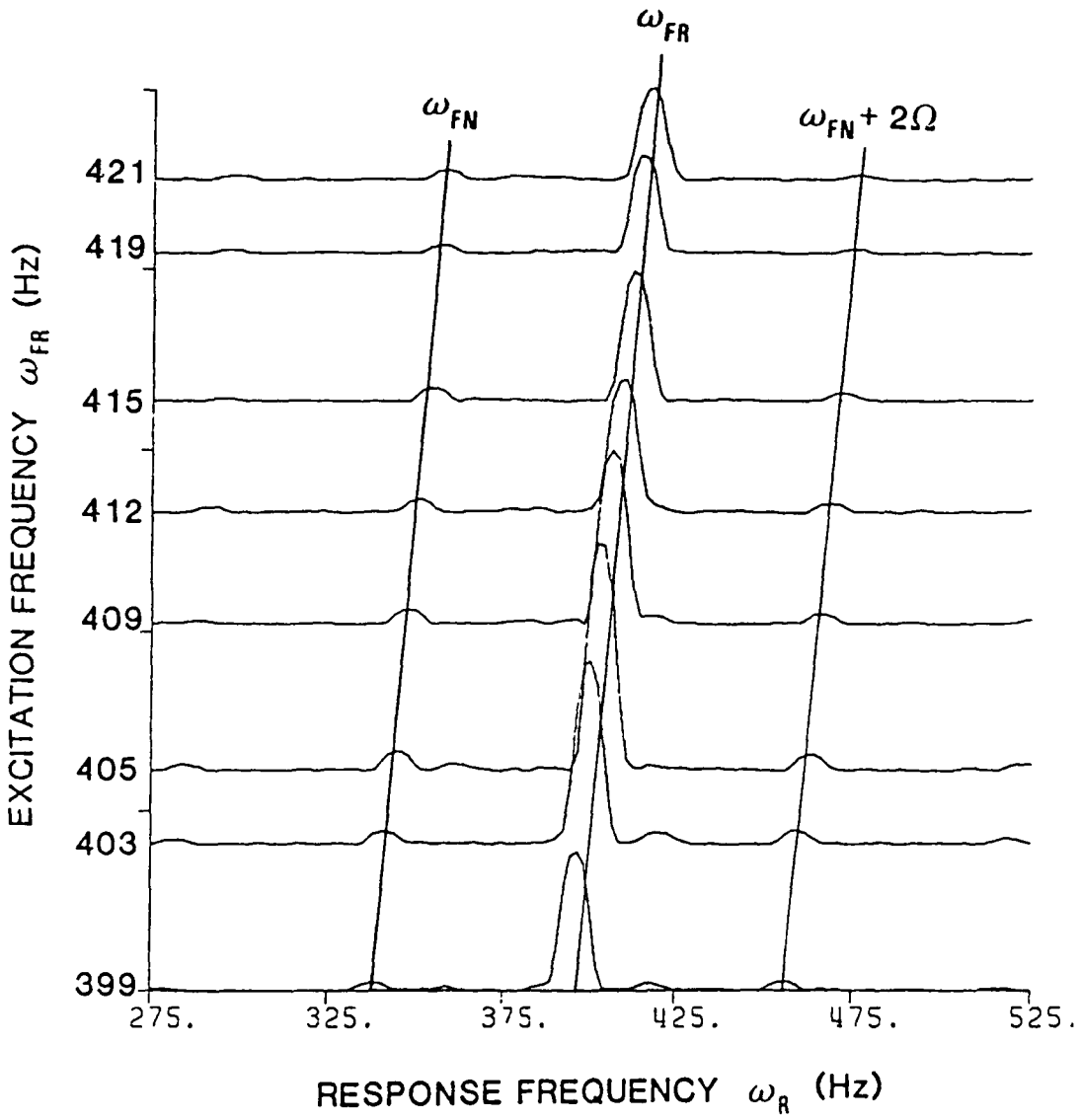

Fig. 5.31 Blade displacement spectral cascade plot for: Ω = 60 Hz, backward whirl excitation of the blade 1ND mode, excitation frequency range ω_{FR} = 399 to 421 Hz.

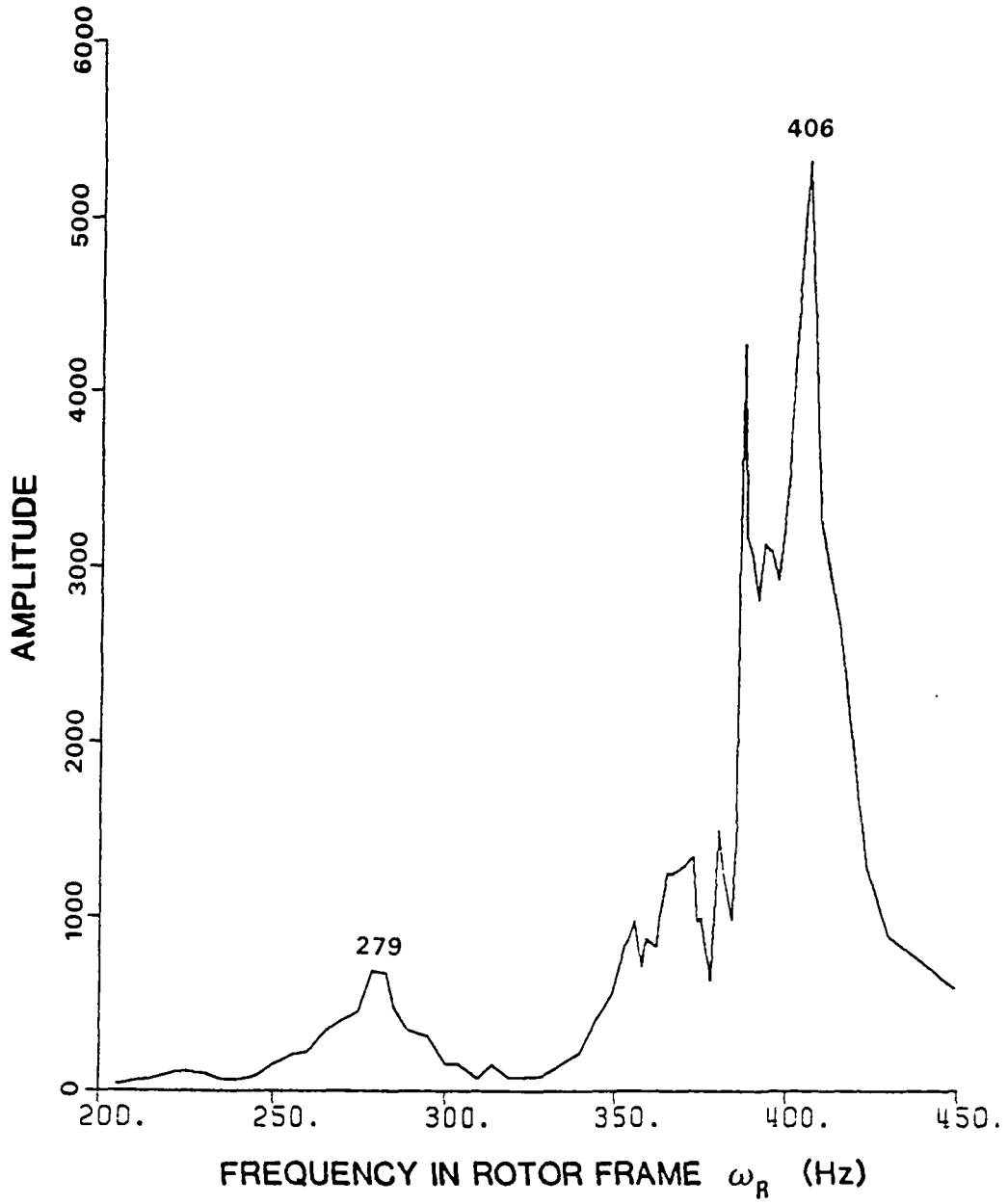

Fig. 5.32 Blade response transfer function for: Ω = 60 Hz, backward whirl excitation.

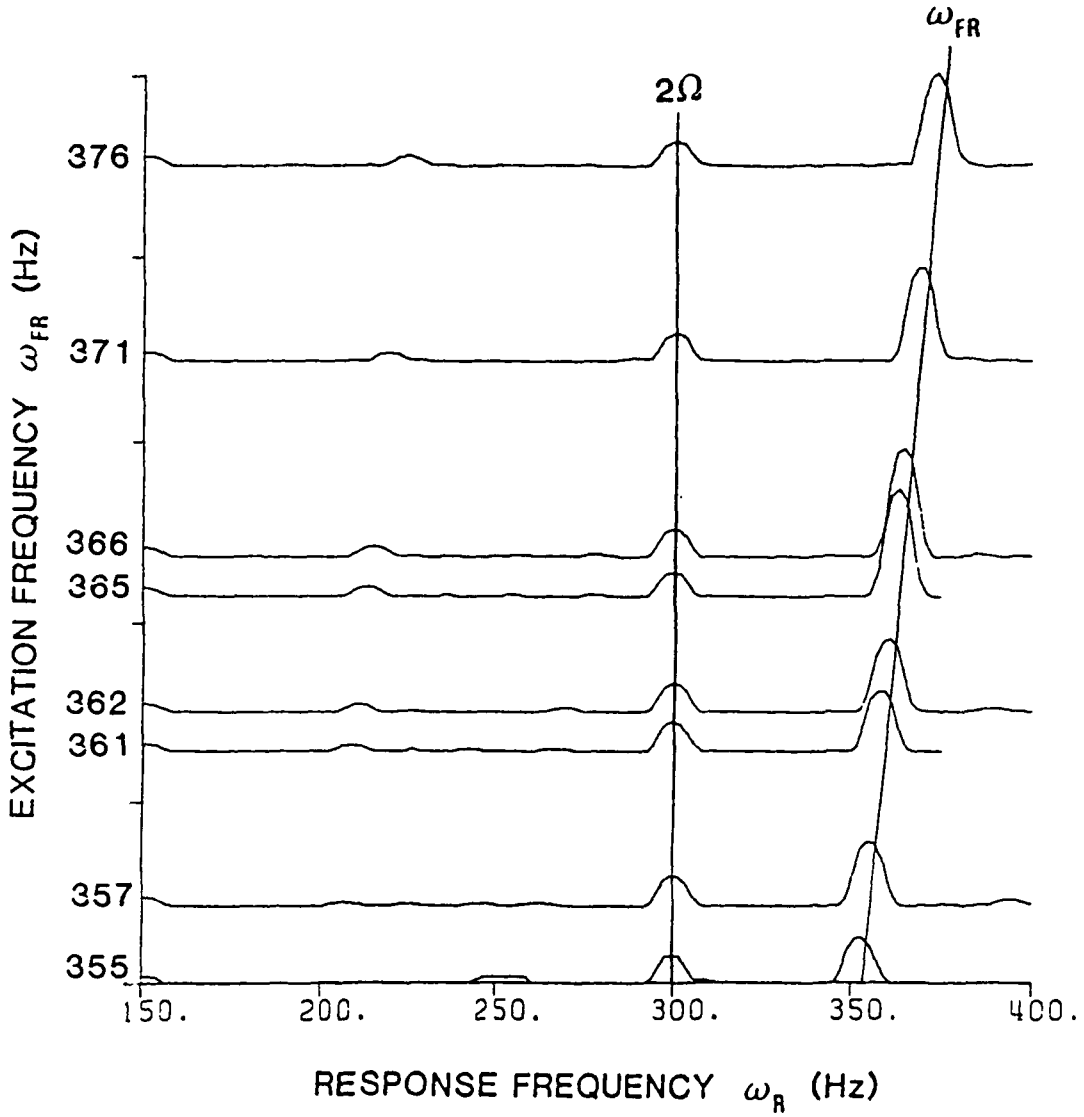

Fig. 5.33 Blade displacement spectral cascade plot for: Ω = 150 Hz, backward whirl excitation of the disk pitch mode, excitation frequency range ω_{FR} = 355 to 376 Hz.

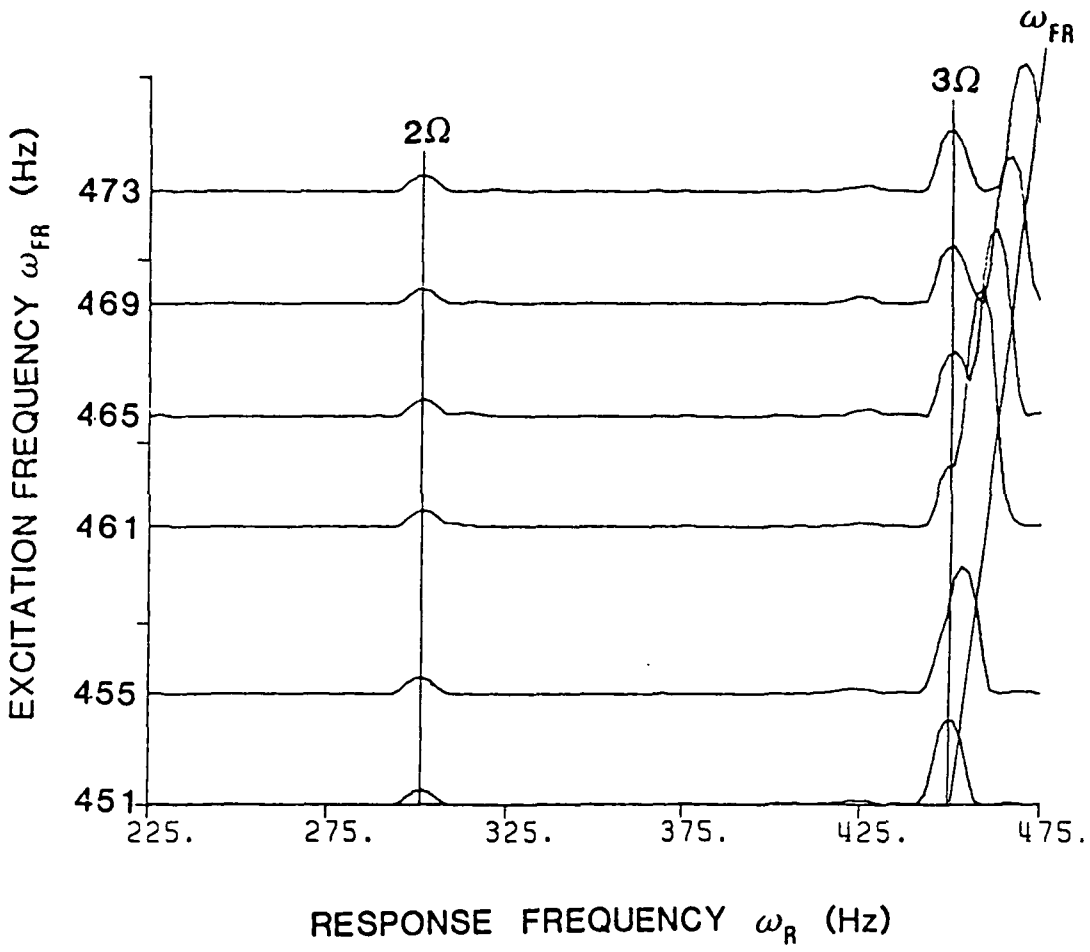

Fig. 5.34 Blade displacement spectral cascade plot for: Ω = 150 Hz, backward whirl excitation of the blade 1ND mode, excitation frequency range ω_{FR} = 451 to 473 Hz.

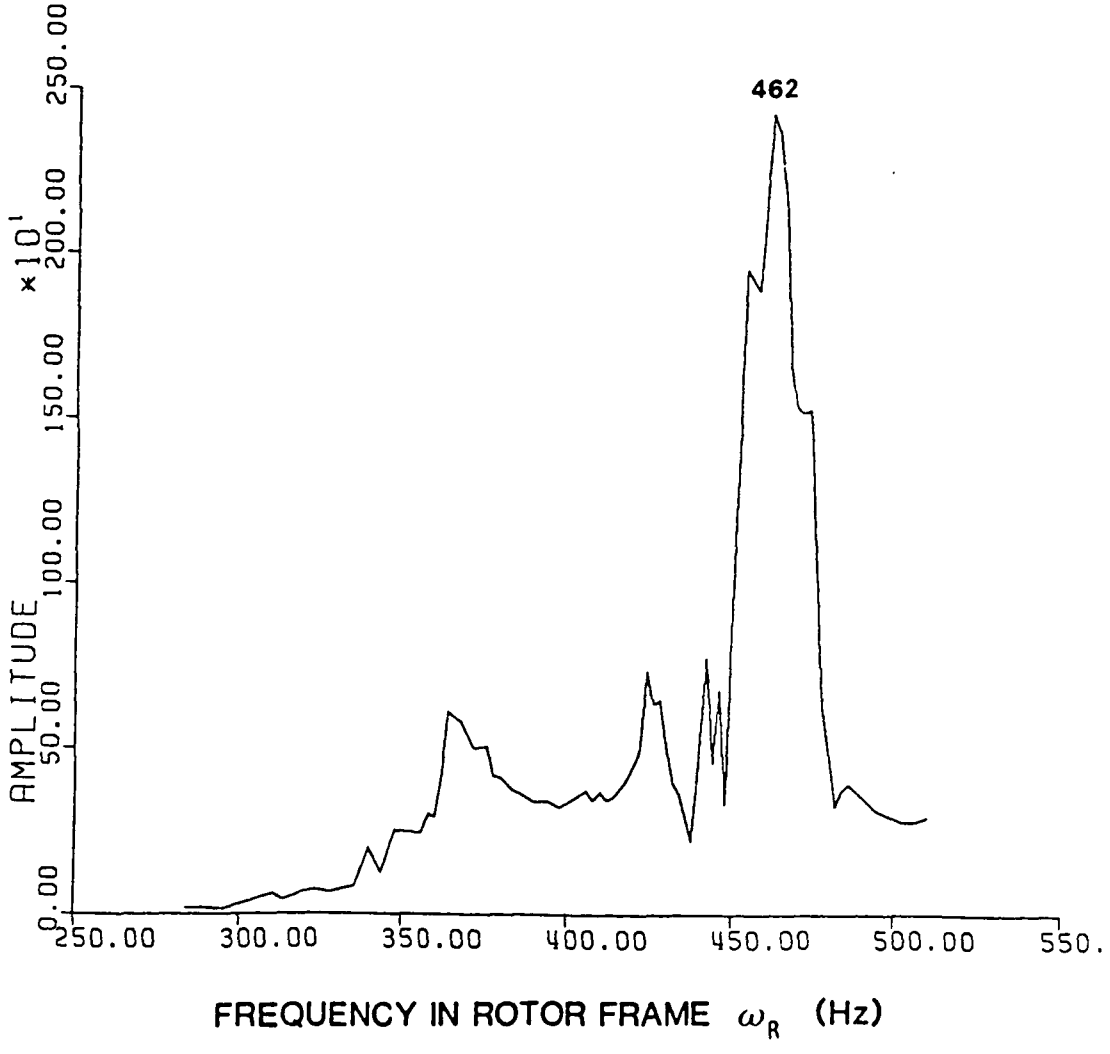

Fig. 5.35 Blade response transfer function for: Ω = 150 Hz, backward whirl excitation.

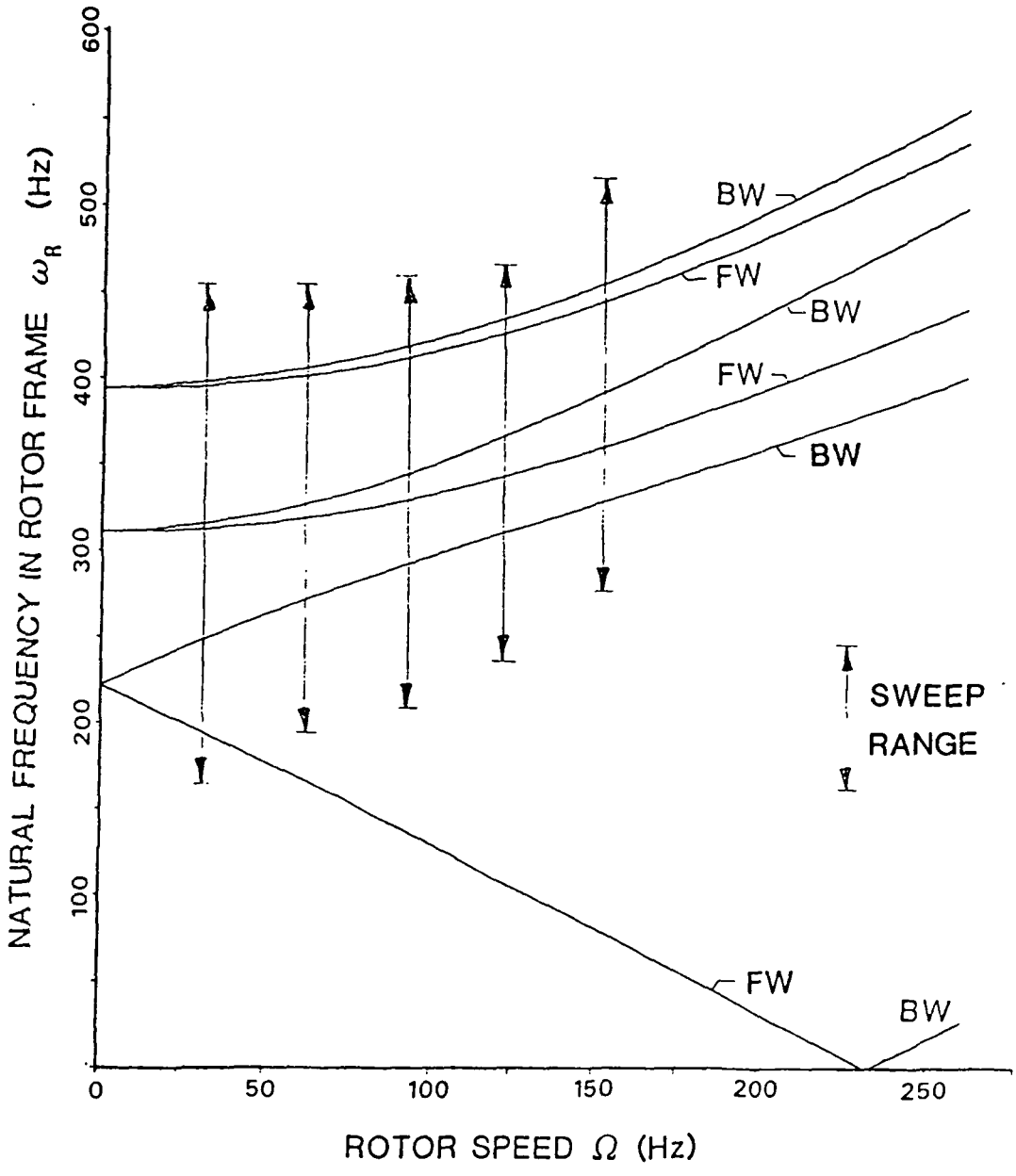

Fig. 5.36 Backward whirl excitation sweep ranges overplotted on the predicted system natural frequency plot.

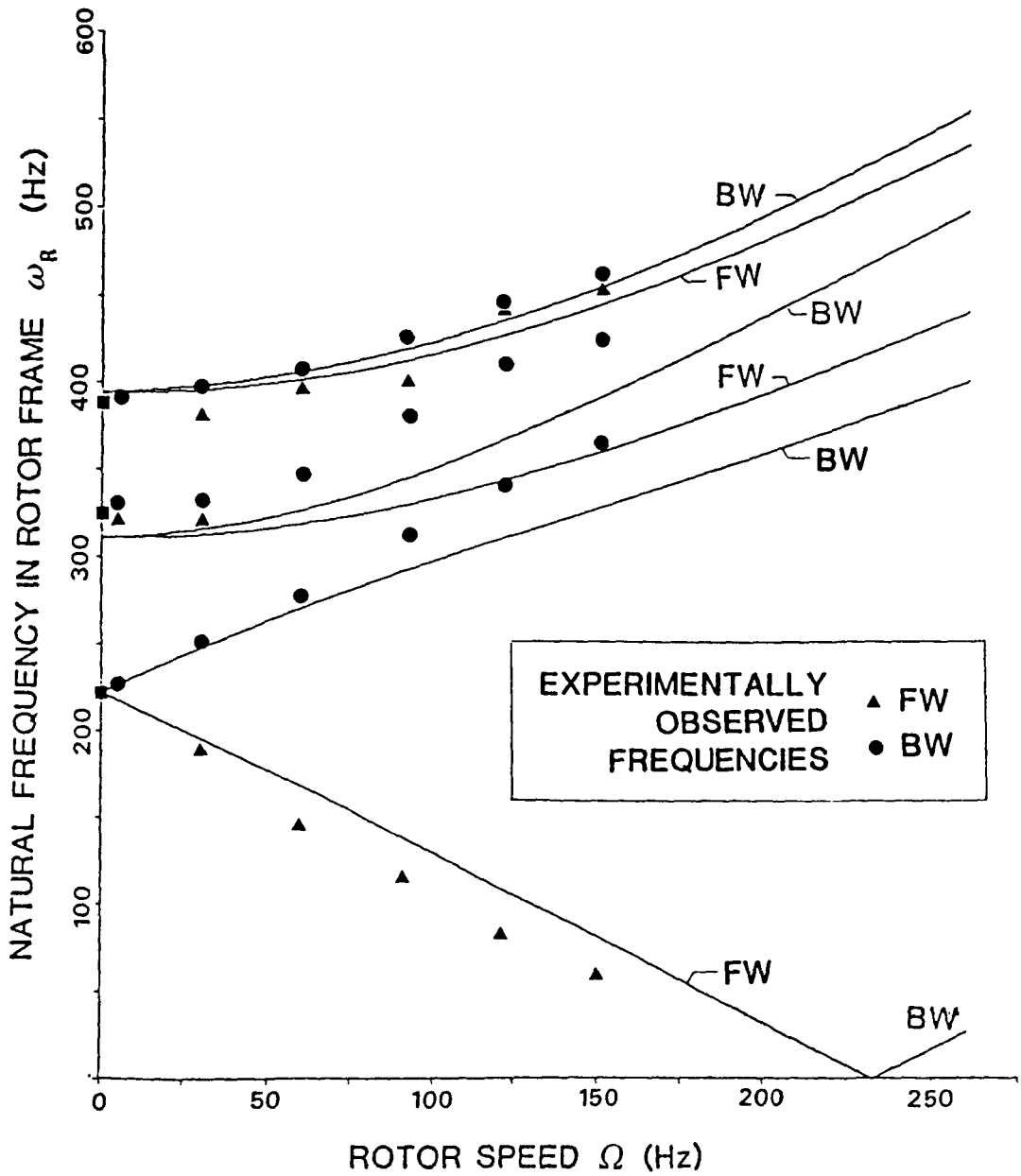

Fig. 5.37 Summary plot of experimentally determined system natural frequencies overplotted on the predicted system natural frequency plot.